

**PROPENE PARTIAL OXIDATION AND LUMINESCENCE
STUDIES ON SELECTED TRANSITION METAL OXIDES**

A Thesis Submitted to Goa University for the Award of the Degree of

DOCTOR OF PHILOSOPHY

In

CHEMISTRY

By

Mr. Shambhu S. Parab

(M.Sc.)

(Research Guide)

Prof. A.V. Salker

GOA UNIVERSITY

Taleigao Plateau, Goa

2018

DECLARATION

I hereby declare that the work embodied in the thesis entitled '**Propene Partial Oxidation and Luminescence Studies on Selected Transition Metal Oxides**' is the result of investigations carried out by me under the guidance of **Prof. A. V. Salker** at Department of Chemistry, Goa University and that it has not previously formed the basis for the award of any degree or diploma or other similar titles.

In keeping with the general practice of reporting scientific observations, due acknowledgement has been made wherever the work described is based on the findings of other investigators.

Mr. Shambhu S. Parab

Ph.D. Student
Department of Chemistry
Goa University

Goa University
March 2018

DEPARTMENT OF CHEMISTRY

CERTIFICATE

This is to certify that the thesis entitled, '**Propene Partial Oxidation and Luminescence Studies on Selected Transition Metal Oxides**' submitted by **Mr. Shambhu S. Parab** is a record of the research work carried out by the candidate during the period of study under my supervision and that it has not previously formed the basis for the award of any degree or diploma or other similar titles.

Prof. A.V. Salker

Research Guide
Department of Chemistry
Goa University

Goa University
March 2018

ACKNOWLEDGEMENT

My Ph.D. tenure in the university was a great learning and enriching experience. Many people created indelible marks in my life through their kind acts of invaluable support. I take this opportunity to express my gratitude towards all of them. First and the foremost, I would like to thank my respected research guide Prof. A.V. Salker, who with his exemplary work ethic has guided me throughout my time in the university. There were the times when he gave me great support and instilled belief in me so that I could complete my work. Learning under him was a great experience. I am filled with immense gratitude to acknowledge his time, expert guidance and valuable technical inputs.

I thank my subject expert and head of the department, Prof. B.R. Srinivasan for his valuable scientific suggestions and motivational support. I also thank former head, Prof. S.G. Tilve for providing the necessary facilities. I am indebted to all my teachers in the department of chemistry for their valuable guidance whenever the need arose. I am also grateful to the present dean and former deans for their kind suggestions. I am very much thankful to UGC, New-Delhi for the financial assistance through UGC-BSR Fellowship.

I sincerely thank all the staff members in the department office and administrative office for the smooth processing of my official formalities. I am thankful to Mr. Agnelo Lopes and from the glass blowing section for helping me wholeheartedly every time. I also thank Mr. Jayprakash and Mr. Madhusudan Lanjewar from instrumentation centre for their valuable technical help. I am indebted to librarian and library staff especially, Mr. Ramchandra Gawas, Mr. Krishna Pai and Mr. Chulu for their ever co-operating presence and care in the library. I am thankful to Mr. Girish Prabhu, NIO Donapaula for providing the XRD facility. I thank MNIT, Jaipur for

extending the facilities of instrumental analysis. I also thank IIT Madras for the characterization facilities provided by them. I am grateful to Dr. Amit Rajput and Mr. Jeya kanthan for their time and important technical discussions

I thank my senior research colleagues, Dr. Puzy Pawaskar, Dr. Satish Naik, Dr. Rohan Kunkalekar, Dr. Shrikant Naik, Dr. Mahesh Majik, Dr. Santosh Shetgaonkar, Dr. Kiran Dhavaskar, Dr. Lactina Gonsalves and all the others for their kind support. I express my gratitude towards my fellow research scholars in our group namely, Madhavi, Mira, Mithil, Celia and Sudarshana for their company and for helping me whenever needed. I would also like to thank Sagar, Diptesh, Prajesh, Hari, Sandesh, Chinmay and all my colleagues and juniors in all the other research groups for their kind support and co-operation. I deeply thank and appreciate Satu, Chandan, Dattaprasad, Rahul, Kedar, Pratik, Aniket and Sanket for their great company, love and care during my stay in the university..

I humbly thank my father Shri. Sakharam S. Parab and my mother Smt. Samidha S. Parab. A million words of acknowledgement will not suffice to describe their untiring efforts and love in raising me. Their strive through the humble origins, sensitive outlook towards life and humility in adhering to our roots have had lasting impressions on me as a person. I also respectfully thank my grandfather, Shri. Ganpat Prabhugaonkar, my grandmothers Smt. Satyabhama G. Prabhugaonkar and Smt. Parvati S. Parab, for their love and blessings. I am also indebted to my younger brothers, Shubham and Dhiraj for their love and affection. I am grateful to all my family members for their blessings and kind words of encouragement.

Last but not the least; I am humbled and grateful to the God for the blessings and blissful company in every endeavours of life.

CONTENTS

		CHAPTER 1	Page No.
1.		INTRODUCTION	1
		CHAPTER 2	
2.		LITERATURE REVIEW	10
	2.1	Propene Partial Oxidation	10
	2.1.1	Acrolein	10
	2.1.2	Early developments in Acrolein production	11
	2.1.3	Explored catalytic systems	13
	2.1.3.1	Copper based catalysts	13
	2.1.3.2	Bi-Mo based catalysts	16
	2.1.3.3	Sb-Sn-O catalysts	21
	2.1.3.4	Miscellaneous catalyst systems	22
	2.2	Bi₄V₂O₁₁ oxide system	23
	2.3	VSbO₄ oxide system	25
	2.4	Luminescence studies on Ca₃V₂O₈ host	27
		CHAPTER 3	
3.		EXPERIMENTAL	31
	3.1	Introduction	31
	3.2	Preparation of materials	32
	3.2.1	Cu/Bi ₂ Mo ₃ O ₁₂	32
	3.2.2	Cu incorporated Bi ₄ V ₂ O ₁₁	33
	3.2.3	VSbO ₄ related compositions	34
	3.2.4	W inserted Bi ₂ MoO ₆	35
	3.2.5	RE doped Ca ₃ V ₂ O ₈ compositions	36
	3.3	Characerization: Theoretical background and practice	38
	3.3.1	Thermogravimetric-Differential thermal analysis	38
	3.3.2	X-ray diffraction	39
	3.3.3	Infra-red spectroscopy	40
	3.3.4	Raman Spectroscopy	40
	3.3.5	Ultraviolet Diffuse Reflectance Spectroscopy	41

	3.3.6	Scanning electron microscopy	42
	3.3.7	Transmission electron microscopy	43
	3.3.8	X-ray photoelectron microscopy	43
	3.3.9	Photoluminescence Spectroscopy	44
	3.3.10	BET surface area analysis	47
	3.3.11	Catalytic activity measurements	49
		CHAPTER 4	
4.		CHARACTERIZATION AND SPECTRAL STUDIES	50
	4.1	Thermal analysis	51
	4.2	X-ray diffraction analysis	61
	4.3	Infrared spectroscopic studies	71
	4.4	Raman spectroscopic studies	77
	4.5	UV-DRS studies	81
	4.6	XPS studies	90
	4.7	SEM studies	97
	4.8	TEM studies	101
	4.9	Luminescence studies	103
		CHAPTER 5	
5.		CATALYTIC STUDIES	115
	5.1	BET surface area measurements	115
	5.2	Partial oxidation of Propene.	118
	5.2.1	Cu/Bi ₂ Mo ₃ O ₁₂ catalysts	118
	5.2.2	Bi ₄ V _{2-x} Cu _x O ₁₁ catalysts	121
	5.2.3	V _{1-x} Cu _x SbO ₄ catalysts	124
	5.2.4	Cu-K-V-Sb-O catalysts	127
	5.2.5	Bi ₂ Mo _{1-x} W _x O ₆ catalysts	130
	5.2.6	M ₃ V ₂ O ₈ catalysts (M= Ca, Sr and Ba)	133
		CHAPTER 6	
6.		SUMMARY AND CONCLUSIONS	137
		REFERENCES	144
		APPENDIX	160

LIST OF ABBREVIATIONS

BE	Binding Energy
BET	Brunauer-Emmett-Teller
CT	Charge Transfer
DRS	Diffuse Reflectance Spectroscopy
DTA	Differential Thermal Analysis
FID	Flame Ionization Detector
FS	Full Scan
FTIR	Fourier Transform Infrared Spectroscopy
FWHM	Full Width at Half Maximum
GC	Gas Chromatograph
ID	Internal Diameter
JCPDS	Joint Committee on Powder Diffraction Standards
MFC	Mass Flow Controller
PL	Photoluminescence
R.E	Rare Earth
RT	Room Temperature
SEM	Scanning Electron Microscopy
SV	Space Velocity
TCD	Thermal Conductivity Detector
TEM	Transmission Electron Microscopy
TG	Thermogravimetry
TOS	Time on Stream
UV	Ultra Violet
UV-Vis	Ultraviolet-Visible
XPS	X-ray Photoelectron Spectroscopy
XRD	X-Ray Diffraction

1. INTRODUCTION

From the early times of nomadic life and cave dwellings, the human civilization has come a long way to enter into today's technologically advanced world. This has been owed to the relentless pursuit of mankind towards the improvement of its livelihood. The prehistoric man transformed into today's advanced human being by constantly striving for the betterment of life and sustenance. This was achieved slowly and steadily by accumulating the knowledge and processing it further through man's ideas. Take for example, the advent of the wheel in the form of a circular wooden log for sliding a simple handcart; the prehistoric inventor would never have imagined that a time would come when his wooden wheel would go on and evolve in the form able to move the modern day transportation marvels such as bullet trains, supercars and supersonic jets. This example just fortifies the true nature of science and what it can achieve through persistent strive for betterment, aided by technological amalgamations. Therefore, even a small contribution of true scientific knowledge to this never-ending trail of science and technology will only help to uncover the new horizons of progress.

The developments in the industrial sectors such as chemical, electronics, and metallurgy industries have contributed a great share in elevating the human index. Industrial sector not only works on the new objectives and strategies but also constantly tries to improvise the existing processes. The widespread industrialization has brought the mankind prosperity but has also led to the serious side effects such as global pollution and difficulty in managing the natural resources due to less efficient processes. Therefore, the industries working on the sound platforms of atom economy (E factor) and environmentally benign methods (based on Green chemistry) are important to alleviate the human progress in a sustained manner [1, 2]. More than any

other industry, the chemical industry is the one which finds itself stuck at the crossroads to manage the balance on the fronts of cost-effectiveness, process efficiency and environment.

The supply of chemical feedstock for the production of fine chemicals has been the mainstay of the chemical industry. The production of these chemicals often comes with lots of waste and heavy consumption of energy. Transforming the waste products into raw materials for other reactions is a constructive step which in many ways contributes to the cause of nature [3]. The application of catalysis to the industrial processes has seen tremendous growth in production and process efficiency and thus is a major helping factor in the world's industrial productions [4]. As is well known the catalyst is the substance that increases the rate of the reaction without being consumed itself in the reaction. Therefore, a catalyst can catalyse the catalytic conversions as long as it does not lose its activity. Consequently, a search for catalytic system robust enough to remain active for longer periods of time is industrially important. In general, the catalysis is divided into two main branches namely, homogeneous and heterogeneous catalysis. In homogeneous catalysis, the reactants and the catalyst are in the same phase whereas, in the heterogeneous catalysis, the reactants and the catalyst are present in different phases. On an industrial scale, the heterogeneous catalysis has found its strong foothold due to its advantages and also due to the inherent disadvantages associated with the homogeneous catalysis. Although, both the processes are prone to catalyst leaching, the continuous phase in case of homogeneous catalysis makes it all the more cumbersome. It must be noted that the field of homogeneous catalysis is also rapidly progressing and one cannot deny the specificity and selectivity that homogeneous catalysts offer. Therefore, homogeneous catalysis is still considered as the backbone of industrial production of fine and hardcore organic chemicals. More innovation in the

process engineering could very well overcome the inherent drawbacks faced by the homogeneous catalysis. In relation to the active centres, homogeneous catalysts offer a set of mostly identical active centres. The active centres found in the heterogeneous catalysts are different from those found in the homogeneous catalyst as there can be a presence of different types of active centres. These different types of active centres present in the heterogeneous catalysts can give broad product distributions. Therefore, when one is dealing with the heterogeneous catalyst, one also has to take into account the homogeneity in texture and the surface morphology of the catalyst so that the product distribution is narrowed as possible. The main drawbacks in case of the heterogeneous catalysts are intricacy in assembling the identical active centres on the catalyst surface and in getting the sufficient yield of the desired product. Sometimes, the high temperature employed in heterogeneous catalysis is also a limiting factor that can affect the performance of the catalyst. The main advantages of heterogeneous catalysts over the homogeneous catalysts are that they generally have higher thermal stability, longer lifetime and can be regenerated time after time with little or no loss in the activity.

Partial oxidations of the hydrocarbons constitute the conversion of the alkanes and alkenes to the desired oxidation products. These transformations of the hydrocarbons are carried out by heterogeneous catalysts with the simultaneous presence of molecular oxygen. The partial or selective oxidations of hydrocarbons are industrially very important reactions which supply a variety of monomers for the production of synthetic rubbers, polymers and fibres [3, 5-6]. Therefore, these oxidation reactions have a major share in the sustainable reactions [7-10]. Some examples of the partial oxidation of the hydrocarbons are the allylic oxidation to aldehydes, ammoxidation, epoxidation and paraffinic oxidation [11-14]. Usually, alkanes are

converted to olefins since they provide an efficient route towards many oxygenated products [15-17]. The conversion of alkanes to olefins is a very costly process, therefore; a trend of directly converting alkanes to the oxygenated products has come into existence [18, 19]. This process also has its own drawbacks as the direct conversion of alkanes to oxygenated products often is accompanied with more selectivity towards the total oxidation products such as CO/CO₂ leading to the loss in process efficiency [20]. To overcome this, the conversion of alkanes to alkenes, such as propane to propene is undertaken through a catalytic process called as oxidative dehydrogenation (ODH) which yields propene from propane in very less cost as compared to the processes which do not utilize catalysis [21].

Amoxidation of propene to acrylonitrile is one reaction which has served as a perfect example of the triumph of heterogeneous catalysis. Acrylonitrile production in the early days was carried out either from ethylene cyanohydrins (derived from ethylene oxide and HCN) or from the combination of acetylene and HCN. The latter process eventually substituted the first one but had the drawback of producing acetylenic impurities which were difficult to separate from the major product acrylonitrile [22]. But the introduction of a novel and clean process of producing the acrylonitrile by the oxidation of propene and ammonia made a giant leap forward in the production of acrylonitrile [23] and since then this process has experienced a great deal of commercialisation and technological development.

Another similar process which emerged in parallel to the amoxidation was the production of acrolein from the propene. This reaction was termed as the allylic oxidation as in this reaction, the oxidation of the allylic carbon of propene is carried out. The basic idea of this reaction emerged from the thought proposed by Lewis *et al.* [24], who proposed that the intrinsic lattice oxygen derived from a reducible metal

oxide could be an efficient and selective oxidant than the molecular oxygen. Since, acrolein is a raw material for a number of important products such as glutaraldehyde, acrylic acid *etc.* its production is of utmost value. This reaction has also served as a model reaction for the researchers to study the basic principles of the hydrocarbon oxidation. Varieties of the reducible metal oxides have been tested over the years for this reaction. Electronically and geometrically accurate ensembles of the surface sites are found to be the essential features for any partial oxidation to occur [25]. Similarly, the partial oxidation of propene also has its own unique set of requirements that a proposed catalyst must have. These requirements could be met using proper preparation methodologies since catalysts are very much susceptible to the preparative conditions such as temperature, pH *etc* [26, 27]. It is also known that the cations present on the catalyst surface act as the acidic or basic sites according to their chemical and electronic nature [28] therefore, a favourable elemental composition is also an essential parameter in designing the efficient catalyst. In our present studies on the partial oxidation of propene, we have explored few established catalyst systems by making some modifications and other systems which were not explored extensively before.

Luminescence spectroscopy is the technique in which a material is irradiated by the electromagnetic radiations to excite the electrons from lower energy levels to the higher energy levels. The excited electrons lose their extra energy as they fall back to their original lower energy levels. There are different paths for losing the extra energy and one of those paths is the emission of electromagnetic radiations longer than the incident ones. The radiations that cause excitation and the subsequent radiations emitted by the material after relaxation, present a clear glimpse into the design of the material structure and the construction of electronic energy levels in the material. Therefore, luminescence spectroscopy can be very well used by coupling it with the other

analytical techniques for a thorough characterization of a given material. Standard procedures of analytical techniques derived from Luminescence spectroscopy are well documented for the qualitative and quantitative measurements in the laboratory. A particular radiation emitted by the material indicates the nature of luminescence centre present in that material. The luminescence centres here are nothing but the ions or functionalities present in the material that can be excited. A slight deviation of luminescence centre from its standard emission pattern, if studied carefully can give valuable insights into the electronic environment present around the luminescence centre. The effect of host material's structure on the luminescence centre and vice versa can also be studied rigorously. Furthermore, as is observed in most of the emission spectroscopy techniques, the emission intensities with proper standardisation can give quantitative estimates of the luminescence centres present in the material.

In recent years, the research surrounding the luminescence spectroscopy has grown by leaps and bounds. This progress has been the result of several applicative facets of luminescent materials discovered by the researchers. As discussed initially in the chapter, every industry has garnered a great amount of momentum due to the new findings and discoveries. The electronic industry since closely associated with the day to day life of people was not made to lag behind. The main application of the luminescent materials is in the lighting devices or light sources. As we know that the primary light sources used by the man are fluorescent and incandescent lamps. In the recent times, it has been realised that these light sources are costly sources of light. Due to this, the light sources in the form of Light Emitting Devices (LEDs) have taken the centre stage. These devices are robust; operate at lower voltages with very good luminous efficiency, colour purity and brightness. Therefore, these materials are the focus of latest research and are in great demand all over the world [29]. These materials

are finding the applications in a number of devices such as Field emission displays, Plasma display panels and already mentioned Light emitting devices [30-32]. Rare earth ions have very rich colour emitting properties [33]. Therefore, introducing these rare earth ions in small quantities in proper host materials to get desirable colour emissions is a great field of interest [34, 35]. Since the valence electrons of the R.E ions are deeply embedded in the atom and therefore are not affected by the ligand fields. Therefore, these ions emit in sharp lines which form the basis for their colour purity [36, 37]. The host materials in which these ions are doped must have some basic properties such as wide band gap and low vibrational energy [38]. Many host materials such as tungstates, vanadates and phosphates are used extensively in the literature [39-41]. In our present studies, we have selected $\text{Ca}_3\text{V}_2\text{O}_8$ as a host material and have substituted R.E ions such as Tb^{3+} , Ce^{3+} and Eu^{3+} . The resultant phosphors have been studied for their luminescence pattern so as to evaluate their colour rendering properties and their probable candidacy for lighting applications.

Based upon the above considerations different metal oxides compositions were synthesised, characterised and were applied towards propene partial oxidation and luminescence studies. The basic methodology of the investigations presented in this thesis consists of following basic points.

- Preparation of the following series of metal oxide compositions using the appropriate techniques such as sol-gel and co-precipitation.

1. $X\% \text{Cu}/\text{Bi}_2\text{Mo}_3\text{O}_{12}$ ($X = 2, 4, \text{ and } 8$)

2. $\text{Bi}_4\text{V}_{2-x}\text{Cu}_x\text{O}_{11}$ ($x = 0.0, 0.1, 0.2, 0.3 \text{ and } 0.4$)

3. $\text{Cu}_x\text{V}_{1-x}\text{SbO}_4$ ($x = 0.0, 0.05, 0.1, 0.2 \text{ and } 0.3$)

4. $\text{Cu}_x\text{K}_y\text{V}_{1-x}\text{Sb}_{1-y}\text{O}_x$ ($x = 0.05, y = 0.02$); ($x = 0.1, y = 0.05$); ($x = 0.2, y = 0.1$); ($x = 0.3, y = 0.15$)

5. $\text{Bi}_2\text{Mo}_{1-x}\text{W}_x\text{O}_6$ ($x = 0.0, 0.2$ and 0.4)
6. $\text{M}_3\text{V}_2\text{O}_8$ ($\text{M} = \text{Ca}, \text{Sr}$ and Ba)
7. $\text{Ca}_{3-3x/2}\text{Tb}_x\text{V}_2\text{O}_8$ ($x = 0.04, 0.08, 0.12, 0.16$ and 0.20)
8. $\text{Ca}_{3-2x}\text{Tb}_x\text{Na}_x\text{V}_2\text{O}_8$ ($x = 0.04, 0.08, 0.12, 0.16$ and 0.20)
9. $\text{Ca}_{2.94-3x/2}\text{Ce}_{0.04}\text{Tb}_x\text{V}_2\text{O}_8$ ($x = 0.0, 0.04, 0.08, 0.12$ and 0.16)
10. $\text{Ca}_{2.48-3x/2}\text{Pb}_{0.4}\text{Tb}_{0.08}\text{Eu}_x\text{V}_2\text{O}_8$ ($x = 0.06, 0.08, 0.10, 0.12, 0.14$ and 0.16)

- Characterisation of these compounds using basic techniques such as TG-DTA analysis, XRD, FTIR Spectroscopy, Raman spectroscopy, SEM, TEM and XPS studies.
- The luminescence of R.E ions in the host lattice with different doping schemes and doping combinations were studied.
- Catalytic evaluation of the prepared catalysts for partial oxidation of propene was carried out on the catalytic set-up. An attempt was made to explain the catalytic activity shown by the catalysis on the basis of their structure and composition.

The present thesis is organised into the following chapters.

Organization of the Thesis

Chapter 1: Introduction: A brief introduction and scope of the research work done have been presented.

Chapter 2: Literature review: An account of the trends found in the literature pertaining to the research work compiled in the thesis is summarized in this chapter.

Chapter 3: Experimental: Procedures of material preparation, details of characterization techniques employed and methods adopted for catalytic activity measurements have been discussed in this chapter.

Chapter 4: Structural and spectral studies: Structural characterization and spectral studies of prepared materials are highlighted in this chapter.

Chapter 5: Catalytic studies: Catalytic activity measurements are reported and elucidated in detail here.

Chapter 6: Summary and Conclusions: Chapter wise summary and conclusions drawn from all the studies are stated in this chapter.

References- All the references cited have been compiled in this section.

2. LITERATURE REVIEW

Extensive background information on any research area provides a sound knowledge regarding the trends prevailing in that area as well as the scope for further investigations. In the first chapter, a brief introduction and scope of the studies presented in this thesis were given. This chapter will give a brief account of the literature reported on the topics studied in the thesis.

2.1 Propene Partial Oxidation

There are many partial oxidation products of propene which vary with respect to the reaction conditions and the catalyst system used. The major partial oxidation products of the propene are namely acrylonitrile, acrolein, acrylic acid [42] and propene oxide [43, 44]. In the present investigation, we have confined our interest only towards the acrolein. Therefore, in the next pages, the literature aspects related to the acrolein will be discussed.

2.1.1 Acrolein

Acrolein is also known by the name propenal. Its molecule is a chain of three carbon atoms and has two unsaturated carbon bondings. One of the unsaturated carbon bonds comes from the vinyl group and the other one from the terminal aldehyde group. These both unsaturated bonds are conjugate to each other. The presence of above two functionalities in acrolein makes it undergo reactions which are typical of both, an unsaturated hydrocarbon and an aldehyde. Acrolein gets polymerized easily, even the acrolein vapours when condensed gets polymerized. Acrolein polymerization in the acidic or alkaline solutions is a very exothermic reaction; no quenching agent can stop this violent reaction. A number of agents can initiate the acrolein polymerization such

as peroxides, heat, and light. Acrolein also reacts with moisture, and therefore acrolein stored in moisture containing bottles is very much susceptible to the polymerization. It is also known to be very toxic, flammable and a harsh lacrimatic agent. Along with its flammability and volatility it closely resembles acetone, but unlike acetone, it is scarcely soluble in water. It is a very well known biocide, and it is sometimes used to control the growth of microbes that cause plugging and blockages in pipelines [45].

Acrolein is known to be present in cigarette smoke in high concentration. It is also found in nature in some foods. The fossil fuel combustion is also one of the sources of the acrolein. Acrolein is not yet classified as an out and out carcinogen and until recently no studies were carried out to check its effect on the human body. But it is also reported that the ingestion of acrolein in rats caused an increase in the growth of cancerous tumours. It must also be noted that some authors have pointed towards the link between the acrolein in cigarette smoke and lung cancer [46- 48].

2.1.2 Early Developments in Acrolein Production

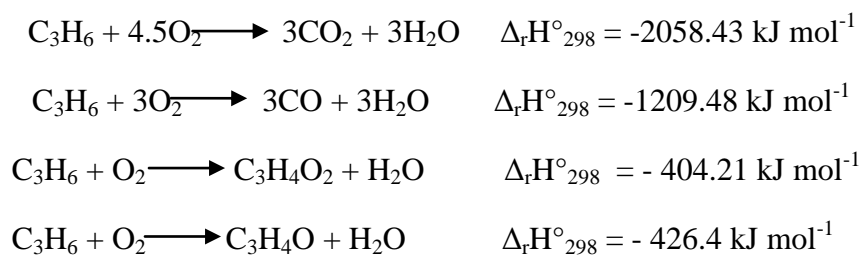
Partial oxidation of propene using heterogeneous catalysts is represented by the following equation,



$$\Delta_r H^\circ = 340.8 \text{ kJ mol}^{-1}$$

$$\Delta_r G^\circ = -180.19 \text{ kJ mol}^{-1}$$

As can be seen from the above thermodynamic parameters, the formation of acrolein is a spontaneous process. It must also be noted that acrolein is not the only product of the catalytic reaction between propene and O₂. Several other products such as CO, CO₂, and acrylic acid are formed and can be represented by the following reactions with their thermodynamic parameters.



[22]

So it can be quickly evaluated from the above parameters that the products like CO and CO₂ are energetically more favoured than the acrolein. Therefore, it was a challenge to produce acrolein. Acrolein was commercially produced for the first time in 1948. The catalyst used was Cu₂O, which was prepared and patented by Hearne *et al.* for the services of Shell chemical company [48- 50]. Vermel *et al* also studied the similar compositions of Cu₂O [51]. The obtained yield from this patented process was not even 50%, keeping a lot of room for the improvement and discovery of new efficient catalysts systems.

In the decade of 1950s, Standard Oil of Ohio (SOHIO) launched a broad search for the catalyst system to efficiently carry out the partial oxidation of propene. Along with the acrolein, SOHIO targeted the valuable compounds such as acrylonitrile, acrylic acid and methacrylonitrile [22]. This research basically was based on the unique idea laid down by Lewis *et al.* [24] which proposed that the lattice oxygen of reducible metal oxide could be a very interesting prospect for partial oxidation than the externally added molecular oxygen. In the initial stages, the reaction was carried out using the test catalysts in a fluidized bed form without the addition of O₂ in the feed. It was noticed that the reaction of propene or reactive intermediates with the gaseous oxygen could give unwanted products such as CO and CO₂. The depleted catalyst was then replenished with the separate stream of O₂. Further studies by the scientists led them

towards the Bi-Mo catalyst which showed better activity and performance than Cu_2O even in the presence of O_2 in the feed.

2.1.3 Explored Catalytic Systems

This subsection will give an overview of the catalyst systems explored so far and their salient features

2.1.3.1 Copper-based catalysts

As discussed earlier Cu_2O was the first heterogeneous catalyst that was applied for the partial oxidation of propene. Early copper containing catalysts were Copper oxides or Copper supported on silica. These catalysts could give propene conversions of about 10-12% and the selectivity up to 60-80% [52]. Many researchers have used these copper-containing catalysts as the model catalysts to evaluate the reaction mechanisms [53- 56]. Woodcock *et al.* studied the catalyst in which the copper was supported on the mixture of Al_2O_3 and SiO_2 . The catalyst gave the total propene conversion of about 18% and the selectivity of about 62% [57]. Wood *et al.* studied the oxidation of propene on the Cuprous oxide and found that the propene oxidation to acrolein is more facile on the stoichiometric Cu_2O . The selectivity to the acrolein was also found to be highest on the stoichiometric Cu_2O [56].

Authors have concluded that CuO gives more of carbon oxides and little of Acrolein [58]. Inui *et al.* have found that slightly copper-rich copper oxide catalyst was suitable for the acrolein formation [59]. Similar to these findings it has been observed that Cu rich Cu_2O is an efficient catalyst, whereas the oxygen-rich Cu_2O formed CO_2 and H_2O [60]. Tuysuz *et al.* studied the Copper loadings on a silica support; they studied the very small amount of loadings from 0.06 to 1%. The selectivity above 50% was found. It was found that the acrolein selectivity decreased with the increase in the

Copper concentration. Therefore, it was concluded that the isolated Copper sites were good for the better selectivity to the Acrolein [61]. Reitz *et al.* have done a comparative study of both the Cupric as well as Cuprous oxides. The finding of the Reitz has revealed that the reduction of Copper oxide was 8-10 times faster than that of the cuprous oxides suggesting that the activation energy on Copper oxide is very less and the complete oxidation on the Copper oxide is due to the highly oxidized species on the surface of the Cupric oxide [62]. Boreskov *et al.* have pointed out that on Cu_2O powder obtained through reduction of CuO , propylene forms two types of adsorbed species reversible and irreversible. The reversible species led to the formation of partially oxidized products whereas the irreversible species formed CO_2 and H_2O . This group has designated the acrolein forming species as Π -allyl species. [63, 64]. A report of the unusual catalyst with the formulation of $\text{Cu}_2\text{Mo}_3\text{O}_{10}$ is found in the literature. It was found that during the reaction the Copper species switched oxidation states from 1+ to 2+ states. Phase changes in the catalyst were also observed. It was concluded that the redox active catalyst system might undergo resonant behaviour with respect to oxidation state and phase under the presence of reaction feed [65- 67].

Propene is a reducing gas and a Lewis base in the sense that it gets adsorbed onto the surface of the catalyst by donating the double bond electrons to the electron deficient surface of the catalyst. Therefore, some of the researchers formulated the catalyst by combining the active Copper oxides on the acidic surfaces. One such study is done by the Jong Sung *et al.* they studied Copper exchanged zeolites. Small amounts of Copper loadings were done on zeolites. The previously exchanged zeolites with Mg were then exchanged with the Copper using Copper Nitrate solutions. The effect of reoxidations was studied on the catalyst. The effect of moisture on the catalyst was also studied, and it was found that the presence of the moisture on the catalyst surface

affected the production of acrolein in a positive way. The conversion of propene up to 5% was found to occur and the selectivity of about 70% was obtained [68]. Same authors have studied Cu^{2+} exchanged X and Y-zeolites in the presence of different types of major co-cations such as Mg^{2+} , Ca^{2+} , Li^+ , Na^+ etc. They reported that the yield of acrolein was dependent on feed gas ratio, Si/Al ratio in zeolite as well as the nature of co-cation. Y-zeolites showed better activity than the X-zeolites. Best results were obtained with an $\text{O}_2/\text{propene}$ ratio of 1 on CuMg-Y zeolite [69]. Recently some authors have studied highly dispersed Cu metallic particles on SBA-15 which showed considerably good activity. It was also found that the Cu metallic particles got oxidized to Cu^{1+} and Cu^{2+} species on coming in contact with the reaction mixture of propene and O_2 . The fraction of Cu^{2+} increased with the increase in temperature [70]. All in all Cu oxides are the only single component oxides that are active towards the partial oxidation of propene and have been a very important contributor towards acrolein's industrial production in the initial stages and also as a model catalyst for the researchers to study. It could also be understood from the above discussions that almost all the researchers agree that the Cu_2O is the phase responsible for the partial oxidation, whereas CuO for the complete oxidation. Until recently the selectivity of Cu_2O towards acrolein was studied by controlling the crystal planes, which adds one more dimension in the quest of selectivity [70]^a. The probable mechanism for the complete oxidation of propene to CO_2 and H_2O can be seen in the following figure,

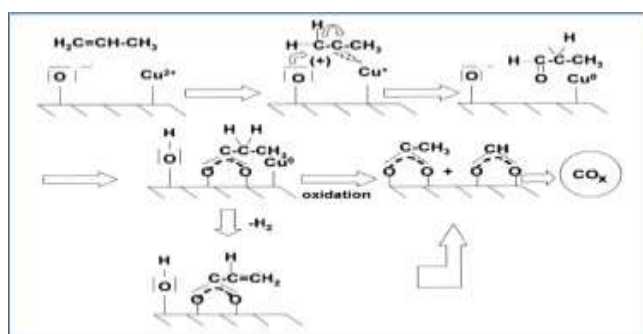


Fig. 2.1 Complete oxidation on Cu^{2+} sites.

2.1.3.2 Bi-Mo based catalysts

Bi-Mo based catalysts were the result of extensive work done by Standard Oil of Ohio (SOHIO). The basic form of these catalysts can be written as $\text{Bi}_2\text{O}_3 \cdot n\text{MoO}_3$. It must also be noted that authors have studied a number of additives to this Bi-Mo catalyst system and have tried to improve it. Right from the start of their discovery in the 1960s by Veatch *et al.* [71] they garnered a great amount of interest in the research community due to their selectivity [72]. Above discovery was greatly dependent on the idea put forward by Lewis [24]. In addition to that, the lattice oxygen which gets depleted by hydrocarbon oxidation was proposed to get replenished from the oxygen present in the feed gas [22, 73]. The tracer experiments that consisted of the isotope labeling of oxygen confirmed that indeed the oxygen was selectively inserted from the catalysts crystal lattice and the catalysts were the primary oxidants for partial oxidation whereas the feed O_2 only reoxidised the depleted or reduced catalysts [74, 75].

After Copper oxide catalysts, Bismuth molybdates are the most extensively researched catalysts not only for acrolein but are also modified for the other products such as acrylonitrile, acrylic acid etc. In the present day, the large-scale commercial production of acrolein is done on the catalysts which have Bi and Mo as the basic exponents [22, 72]. Several phases of Bismuth molybdates are known, but out of those phases only three are known to be active namely, $\gamma\text{-Bi}_2\text{MoO}_6$, $\beta\text{-Bi}_2\text{Mo}_2\text{O}_9$ and $\alpha\text{-Bi}_2\text{Mo}_3\text{O}_{12}$. A great amount of attention is dedicated towards the evaluation of their activity. Most of the researchers have concluded that the $\text{Bi}_2\text{Mo}_2\text{O}_9$ is a better catalyst than $\text{Bi}_2\text{Mo}_3\text{O}_{12}$ [76- 80]. Bi_2MoO_6 has caused the most difference in opinion among the researchers, some have proposed it to be the most active phase [81] whereas, some have stated that it is the least efficient phase out of the three [82]. Some reports also suggest that its activity is comparable to $\text{Bi}_2\text{Mo}_3\text{O}_{12}$ [83]. Overall from the above

discussions, it could be speculated that the preparation techniques and conditions used might have a major say on the catalysts. The parameters such as the concentration and the pH of the metal solutions used as well as the order of mixing could play an important deciding role in textural and compositional factors of the catalyst. It is also found that the preparative conditions like calcination differ vastly in the reports [84]. But the little emphasis on such studies has been given in the literature [85, 86]. The activity of Bi_2MoO_6 for butane oxidation has been reported to be dependent on the preparative conditions used [87, 88]. These reports present the insights about how the preparative procedures can affect the changes at an atomic and molecular level to change the nature of active centres and thus the resultant activity. Some researchers have proposed that the difference in efficiencies could occur due to the compositional and textural changes occurring on the surface. These researchers have pointed that the accumulation of Bismuth on the catalyst surface due to calcination could lower the activity and selectivity significantly [87, 89- 91].

Apart from the evaluation of catalytic activity of these three phases individually. The synergistic effects in the mixture of these catalysts have also been reported [92]. The synergy effect has been experienced in the form of improvement in catalytic activities. Reports have suggested about the synergy between α and γ phases obtained through decomposition of β phase [79, 80 and 93]. A synergy effect between γ and β phase has also been reported. It seems that the different phases have a specific role to play in the synergy interactions. It has been reported that γ phase is responsible for the oxygen transport [9, 94] whereas, β and α phases were understood to have higher number of active sites for the adsorption of propene [95- 97]. A schematic figure given below depicts a general mode of synergy between the Bismuth molybdate phases.

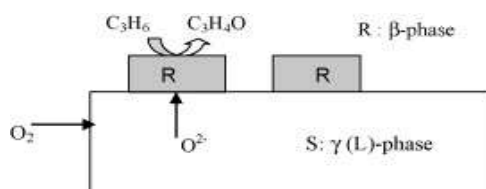


Fig. 2.2 A schematic to show synergy between γ and β phase.

In addition to the individual use of above three phases, the introduction of divalent metals in their lattice has found to have positive effects on the catalytic activity [98, 99]. The improvement was attributed towards the synergy effect between the bivalent metal ion and the molybdate, the synergy effect observed by Moro-oka was based on the support effect [100]. Vedrine *et al.* in their studies have stated a morphological reason behind the improved catalytic activity. In their studies on FeCoBiMoO catalyst, they found that $\text{Fe}_{1-x}\text{Co}_x\text{MoO}_4$ particles were deposited on the large Bi-Mo particle. They concluded that the bivalent molybdate enhances the mobility of electrons thus the redox mechanism is also encouraged improving the activity [101, 102]. Besides the morphological and support effects, in several other reports, the involvement of lattice oxygen is reported after the introduction of bivalent ions [103-105]. An interesting behaviour is reported by Ueda *et al.* the catalyst systems in which the bivalent metal ions are lower in size than Bi^{+3} cation, the Bi-Mo part furnishes the lattice oxygen and the bivalent metal molybdate part acts as the support. But in the systems wherein the bivalent metal ions are larger in size than the Bi^{+3} , the lattice oxygen from both the systems are involved in the reaction [106].

Based on the above discussions it could be understood that the meaningful additives can add valuable attributes to the Bi-Mo based systems. Taking this into the consideration many authors prepared the multi-component catalysts which were industrially successful for the preparation of acrolein as well as acrylic acid [107- 110]. These multi-component catalysts prepared by co-precipitation methods usually have

low activities due to their lower surface area. In this context, Jo *et al.* prepared Bi-Mo based multi-component catalyst using Pechini process with the addition of Ethylene glycol. The addition of ethylene glycol decreased the propene conversion due to the lack of active crystalline phases like $\text{Bi}_2\text{Mo}_3\text{O}_{12}$ and Bi_2MoO_6 . But the selectivity towards acrolein and acrylic acid increased due to the reduction in surface acidic sites and increased synergy between Bi_2MoO_6 and $\text{Bi}_2\text{Mo}_3\text{O}_{12}$ as a result of better homogeneity [111].

Throughout the literature, the Bismuth molybdates are prepared using different preparatory techniques such as solid state [112] and widely used co-precipitation method [93, 94, 113- 115]. Sol-gel technique has been used scarcely by the authors. Sol-gel or sometimes called as the complexation method is a very important method as it offers a homogeneous mixture of the precursors and maintains expected stoichiometry unlike the co-precipitation techniques wherein the pH, the concentration of metal salt solution largely influence the precipitating phases [116- 118]. The complexing or the gelling agents which are usually the acids such as citric acid help in forming the three-dimensional interconnected network of the metal centres. These precursors on decomposition can result in a porous structure leading to the material with high surface area [119]. Some authors have also followed the complexation with the spray drying methods [95, 120]. By the conventional method of preparation, the surface area of Bismuth molybdate compounds have been on the lower side, and have been an obstacle in exploiting their true potential [121- 123]. In recent times, authors have reported methods such as flame pyrolysis and hydrothermal methods to get Bi-Mo catalysts with high surface area [124- 126].

The exceptional catalytic activities possessed by the three basic molybdates contributed from the structures possessed by these oxides. the $\alpha\text{-Bi}_2\text{Mo}_3\text{O}_{12}$ structure is

derived from the CaWO_4 structure which is called as the Scheelite structure. The structure of $\alpha\text{-Bi}_2\text{Mo}_3\text{O}_{12}$ was proposed by Van den Elzen and Rieck using single crystal x-ray diffraction technique [127]. This structure was later on confirmed by Theobald *et al.*[128]. The Scheelite structure is composed of the stacking of the Ca^{2+} and WO_4^{2-} ions. These ions are replaced by Bi^{+3} and MoO_4^{-2} respectively in $\text{Bi}_2\text{Mo}_3\text{O}_{12}$. MoO_4 tetrahedra here are present in the form of Mo_2O_8 but are again differentiated into two forms. In one there is a centre of symmetry whereas the other form lacks it. The coordination number of Bi^{+3} is 8. The correct structure of $\gamma\text{-Bi}_2\text{MoO}_6$ was also reported by Van den elzen [129]. This structure consists of alternating layers of $[\text{BiO}_2]^{2+}$ and $[\text{MoO}_2]^{2+}$ and the octahedral MoO_6 are linked to each other by corner-sharing [130]. In $\beta\text{-Bi}_2\text{Mo}_2\text{O}_9$ four clusters of MoO_4 tetrahedra are built to become Mo_4O_{16} and are bound together by Bi atoms [131]. Bi atoms are surrounded by 8 oxygens from the MoO_4 tetrahedra. There are some oxygens which are only connected to Bi. This structure is composed of oxygen chains which are only connected to the Bi cation, and this Bi^{+3} cation runs parallel to $(\text{Mo}_4\text{O}_{16}\text{-Bi-Mo}_4\text{O}_{16})$ stack. From the above discussion, it is clear that all the three phases are composed of some sort of layer structure, with the presence of redox active cations in them which provide the passage and work as channels for the oxygen mobility [132], which has great implications in the oxidation catalysis. A very simplistic view of these structures could be given as follows.

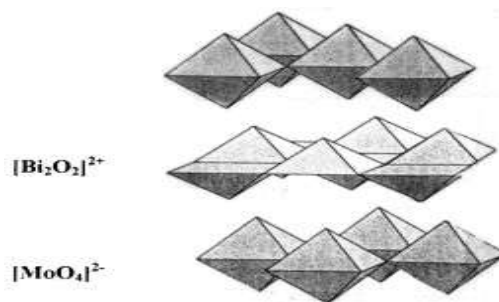


Fig. 2.3 A Simplistic view of the layered structure.

2.1.3.3 SbSnO catalysts.

Sb-Sn-O catalysts reported in literature mostly consist of many phases. The presences of different phases are attributed to many factors such as timescale of calcinations, heating temperature and the concentrations of the constituent metals, Sb and Sn [133- 136]. Out of the many phases formed in the catalysts, two were identified, a solid solution of SnO₂ and SbO₂ and the other phase was identified to be as α and β forms of Sb₂O₄. The composite nature of the catalyst was the main hurdle in identifying the active phases. But an observation was made that suggested that the catalytic activity reached its peak when both the above said phases were present tied with the surface enrichment by antimony [137, 138]. It is also reported in the literature that none of the above phases were active as a catalyst for the reaction when used separately [139]. Some authors have proposed that the selectivity shown by the catalysts is dependent on the presence of Sb⁺⁵ which is stabilized in the tetragonal environment of SnO₂. These Sb⁺⁵ ions are proposed to be octahedrally co-ordinated sites efficient for the allylic oxidation with Sb⁺⁴ acting as an oxygen activating site. Some authors have also proposed Sb⁺⁴ as a sole active site. [140, 141].

In relation to another catalysts system which contained Fe in addition to Sn and Sb, authors proposed that the active sites were exclusively the Sb⁺⁵ and Sb⁺³ ions connected with bridging oxygen. Sb⁺³ ions were claimed to be the H- abstraction sites whereas the Sb⁺⁵ sites were assigned redox action that is, oxygen insertion [96]. So the active site was proposed to be the redox couple of Sb⁺⁵/Sb⁺³ present on the surface of Sb_{1-x}Sn_xO₂ solid solution or on a fine Sb₂O₄ layer formed on the above solid solution [137]. An interesting report claimed that the small addition of Sb to SnO₂ enhanced its conductivity by a considerable margin and this increase was claimed due to the

substitution of Sb^{5+} for Sn^{4+} in SnO_2 lattice. This hints at the redox activity of Sb^{5+} in the lattice [142].

2.1.3.4 Miscellaneous catalyst systems

Uranium antimonite consisting of $\text{USb}_3\text{O}_{10}$ and USbO_5 was studied. In this catalyst, both U and Sb were present in +5 oxidation state. It was learned that the first phase was very efficient and selective towards the acrolein whereas the second phase was labeled less selective towards acrolein. All in all the activity of this antimonite catalyst is determined by the degree of presence of $\text{USb}_3\text{O}_{10}$ phase. It was also reported that this catalyst has a unique oxygen mobility favouring the partial oxidation. But, as evident from the presence of uranium, its radioactive nature barred it from any practical applications [143- 146].

Imachi *et al.* in 1983 studied 1.5% Rh / Al_2O_3 catalyst. Very low conversions and selectivity were found. A similar study was also done by Duan *et al.* using Rh/ TiO_2 as a catalyst [147, 148]. The above two examples show the failure of precious metal to carry out the allylic oxidation. In 2001, Xie *et al.* reported the catalysts in which the Pd (2wt %) was supported on SDB (Styrene Divinyl Benzene) and the moisture effect was studied. In presence of the moisture, it was found that the complete oxidation was suppressed with the increase in the rate of formation of acrolein and acrylic acid. The selectivity to the acrolein mainly is thought to be increased due to the blockage of the complete oxidation sites by water and creation of oxygen insertion sites [149].

Dimitratos *et al.* in 2007 studied two catalyst systems, in the first one Au was incorporated in $\text{Cs}_{2.5}\text{H}_{1.5}\text{PVMo}_{11}\text{O}_{40}$ and in second, $\text{Cs}_{2.5}\text{H}_{1.5}\text{PVMo}_{11}\text{O}_{40}$ was supported by 15% Au/ TiO_2 support. It was found that Au in $\text{Cs}_{2.5}\text{H}_{1.5}\text{PVMo}_{11}\text{O}_{40}$ showed the total conversion of about 36% with the selectivity mainly for the Acetic acid (34.7%).

$\text{Cs}_{2.5}\text{H}_{1.5}\text{PVMo}_{11}\text{O}_{40}$ supported on 15% Au/TiO₂, showed lesser conversions but retained the higher selectivity for the acetic acid and acrylic acid [150]. He *et al.* in 2000 presented synergetic effect of Te₂MoO₇ and MoO₃. Different catalysts with the different ratios of the Te and Mo were prepared, individual activities of MoO₃, TeO₂, WO₃ were also studied. It was found that activity of Te₂MoO₇ was increased with the addition of MoO₃ and WO₃ but this was not observed with the addition of TeO₂ [151].

Zhang *et al.* in 1999 prepared series of compounds with the formula RE₂M_{2/3}Nb_{4/3}O₇ (RE=Nd, Sm, Eu; M=Cu, Co, Zn) by wet chemical methods. These RE containing oxide systems were not found to be relevant for the partial oxidations but the total conversions of propene were found to occur at temperatures between 400 to 500 °C [152].

2.2 Bi₄V₂O₁₁ oxide system

Bi₄V₂O₁₁ is sometimes denoted as Bi₄V₂O_{11-δ} as it is an oxygen-deficient oxide. It belongs to the structural family of compounds known as Aurivillius. This type of compounds are represented by the general formula, (Bi₂O₃)(A_{n-1}B_nO_{3n+1}), A and B are the metal ions in the structure which has co-ordination number of 16 and 6 respectively, whereas 'n' denotes the number of BO₆ octahedra. These octahedra are stacked in a perpendicular direction of the sheets. The basic structure is composed of Bi₂O₂ layers and (A_{n-1}B_nO_{3n+1}) layers which are perovskite-like slabs. The Vanadate layer is sandwiched by Bi₂O₂ layer. Stereochemically active 6s² lone pair of Bi⁺³ points toward the vacant sites [153,154]. There are three polymorphic forms exhibited by Bi₄V₂O₁₁ namely, α-Monoclinic form, β-Orthorhombic form, and γ-Tetragonal form. These polymorphs can be described in a mean orthorhombic unit cell with the parameters

$a_m=5.5\text{\AA}$, $b_m=5.6\text{\AA}$ and $c_m =15.3\text{\AA}$ [155]. The two transitions involving above three polymorphs can be shown as follows,



It is found that the increase in the temperature increases the symmetry of the polymorphs. The high-temperature γ is tetragonal in symmetry whereas the lower temperature polymorphs α and β show super lattice reflections. $2am$ superstructure is associated with the β phase and $6am$ superstructure is associated with α phase [155-159]. These compounds have been extensively studied for their dielectric properties, oxygen separation membranes and for their high ionic conductivity [160- 164]. This property enables for their applications in the solid oxide fuel cells [165, 166]. These compounds are reported for the use in photocatalysis due to their lower band gap values and apt electronic structure [167- 169].

$\text{Bi}_4\text{V}_2\text{O}_{11}$ is a very good oxide ion conductor [170, 171]. Among the three polymorphs, γ -polymorph shows the highest ionic conductivity due to the presence of vacancies in the perovskite-like Vanadate layer which are sandwiched between bismuthate layers. The α and β phases do not have the disorderliness of vacancies and hence have higher activation energies resulting in lower conductivities [172, 173]. It is reported widely that the high-temperature γ polymorph could be made stable by doping $\text{Bi}_4\text{V}_2\text{O}_{11}$ with the metal ions of aliovalent valences [174- 177].

The role of lattice oxygen in the partial oxidation is well known up till now. Oxygen is added to the hydrocarbons from the lattice sites and is replenished by the incoming feed oxygen. Therefore this process has a lot do with the oxygen mobility in the lattice as oxygen replenishment is a to and fro process between the bulk and the surface. But it's study in relation to the partial oxidation is relatively understated but

has got the attention from the other fields such as fuel cells and oxygen generators [178, 179] may be because the above-said applications deal more with the bulk than the surface. But it has proved it's worth elucidating the synergistic effects in multi-component catalysts for acrolein [102] Therefore, it is proposed that the membrane reactors incorporating the oxide ion conductors could be used to increase the conversion and selectivity of partial oxidation products in oxidation [180]. Some compounds related to the $\text{Bi}_4\text{V}_2\text{O}_{11}$ compounds have been utilized for the oxidative dehydrogenation of propene [181] and dehydrodimerization of propene [182, 183].

These compounds are mostly prepared by solid state or ceramic methods, [184, 185] rarely some methods like solution deposition or sol-gel method are reported [186, 187]. From the above discussion it can be understood that the $\text{Bi}_4\text{V}_2\text{O}_{11}$ and related compounds have broad application in which their important attributes such as oxide ion mobility, low band gap nature is exploited.

2.3 V-Sb metal oxide system

VSbO_4 oxide for the first time was reported by Vernon and Milligan [188]. Tetragonal rutile type of structure was assigned to this compound. The oxidation states of Sb and V claimed were +3 and +5 respectively. This rutile tetragonal structure was later on confirmed as Rutile by Roth and Waring [189]. They also added that oxide has a higher temperature polymorph. Schuer and Klemm based on their magnetic studies stated that the oxidation states initially thought by Vernon and Milligan were not correct. But the confirmation of the oxidation states was stumbled upon two combinations, $\text{V}^{+4}\text{Sb}^{+4}\text{O}_4$ and $\text{V}^{+3}\text{Sb}^{+5}\text{O}_4$ [190].

Later on, VSbO_4 was prepared by Birchall and Sleight who also reported rutile tetragonal structure [191]. VSbO_4 is understood to be a structure with the cationic

defects and is composed of 16 % cationic defects. This has resulted in the presence of V^{4+} oxidation states for Vanadium. This cation deficient composition can be represented as $V_{0.64}^{4+}V_{0.28}^{3+}Sb_{0.92}^{5+}\square_{0.16}O_{42}$ where a square represents the vacancies present. This composition is claimed to be the source of V-Sb catalyst activity [192]. Thus the presence of redox couple of V^{4+}/V^{3+} could be considered a facilitator of catalytic activity towards important oxidation reactions.

V-Sb mixed oxides are found to be efficient and selective towards many oxidation processes such as selective neutralization of N containing volatile organic compounds, Hydrogen sulfide oxidation to sulfur, conversion of methane to formaldehyde, and isobutene transformation to methacrolein [193- 196]. These catalysts are also able catalysts for the ammoxidations or oxidations of propane or propylene for the production of acrylonitrile [197- 200].

Researchers report that the formation of V-Sb oxides depends heavily on the method of preparation and thus the variation in the catalytic activity is observed [201]. Authors have reported the presence of segregated phases such as V_2O_5 and amorphous oxides of Sb such as Sb_2O_3 and α - Sb_2O_4 [202, 203]. Haraguchi *et al.* have prepared α - $Sb_2O_4/VSbO_4$ on a silica substrate by electron lithography [204]. The width of the α - Sb_2O_4 layer affected the acrolein formation rates. Similar catalysts system is also reported by a separate author [205]. Acrolein was also reported to be produced from the Mo-V-Sb catalyst. The selectivity towards the acrolein and acrylonitrile was increased with the introduction of Mo in $VSbO_4$ [206].

Site isolation approach has been used by the researchers in hydrocarbon oxidations. In this approach, the active centres are diluted by the addition of inert material. The oxidized products of the lower hydrocarbons can get serially oxidized to

completely oxidized products due to the prolonged stay on the catalysis. Therefore, in this case, the introduction of inert metal ions can act by facilitating desorption of the products or by reducing the acidity of the surface of the catalyst, such approaches are used in the literature for catalysts including VSbO₄ [207- 210].

2.4 Luminescence Studies

Recent times have seen great attention being shifted towards the research on luminescent materials as they are very good devices for lighting in Field emission display (FEDs), X-ray detectors, Cathode Ray Tubes (CRTs), Plasma Display Panels (PDPs) and white light emitting diodes due to their excellent luminous efficiency and limited use of energy [211- 214]. White light-emitting diodes (w-LEDs) possess advantages such as very good efficiency, lower power consumption, long working life [215]. In light of these facts, w-LEDs have become a preferred choice for illumination and therefore have garnered interest from the researchers [216, 217].

Vanadium has a structural chemistry in which it is present in various coordination environments such as square pyramidal, tetrahedral and octahedral in different oxidation states. This coupled with their intrinsic luminescence properties have been used extensively in optical materials of broad applications [218, 219]. Taking this into the consideration the alkaline earth metal orthovanadates, M₃V₂O₈ (M = divalent metal), have been given a great amount of interest due to their interesting ferroelectric properties, transport properties and for their use in the solid-state lasers. In addition to this, they are also known for their thermal stability, crystallographic properties, and visible light transmission properties [220- 223]. Therefore, in recent times, many researchers have directed their attention towards the rare earth ions incorporated alkaline earth metal vanadates [221, 224- 226]. The lower price and their

abundance have been the important reasons for developing them as the alternatives for the materials with the higher cost tag such as YAG: Ce⁺³ and YVO₄: Eu⁺³ which are used in cathode ray tubes and white LEDs [227- 229].

Ca₃V₂O₈ is one such compound of alkaline earth metal vanadates family which has been studied with great interest. Ca₃V₂O₈ is a ferroelectric compound [230] and was discovered as a host material for laser by Brixner [225]. The Ca₃V₂O₈ structure is derived from a distorted variant of the K₂Pb(SO₄)₂ Palmierite structure and is composed of M (XO₄)₂⁴⁻ layers, [M is a divalent atom and X is a pentavalent atom] joined by M²⁺ cations wherein the hexagonal close packing is formed by oxygen. The interlayer sites for the Ca²⁺ cations are half filled with a random distribution of vacancies. This defect structure with inherent defects along with the presence of V⁴⁺ ions is responsible for its high-temperature ferroelectric property and high electronic conductivity. Ca²⁺ ions with different co-ordination number are placed at nonequivalent sites of the lattice which results in the deviation from the Palmierite structure [220, 231- 233]. Ca₃V₂O₈ was prepared first by Tammann in 1925 [234].

RE-doped Ca₃V₂O₈ are prepared extensively in the literature. Following paragraphs will give a brief overview of the different compositions prepared and their peculiarities. The fluorescence spectrum of the Sm-doped Ca₃V₂O₈ single crystal was reported in 1993. The crystal was grown by a Czochralski method. Authors concluded that the luminescence efficiency was too low for this phosphor [235]. Bi and P were co-doped in Ca₃V₂O₈: Eu⁺³, using a simple solution technique in which all the starting materials were mixed in nitric acid and then calcined at 740 °C. The effect of this co-doping on Eu⁺³ emission was evaluated [226]. Eu⁺³ emission was tested in Ca, Sr and Ba orthovanadates prepared by a conventional high-temperature solid-state method and the energy transfer between VO₄⁻³ and Eu⁺³ was found to occur. The ionic radius of the

alkaline earth metal was claimed to affect the emission line positions [236]. Site symmetry and luminescence studies on mixed $(\text{CaBa})_3(\text{VO}_4)_2$ were done under the blue excitations, an optimum concentration of Ca and Eu for the best luminescence was reported by the authors. The phosphors were prepared by solid state technique [237]. The same authors have studied the Ca and Mg mixed vanadates with the simultaneous doping of Yb^{+3} and Eu^{+3} [238]. The optimum concentrations and the mechanism of the luminescence were studied in detail by the authors. In one of the reports, Eu^{+3} and Li^+ were doped simultaneously in $\text{Ca}_3\text{V}_2\text{O}_8$ lattice using a simple solution technique, the introduction of Li was said to increase the luminescence intensity of Eu^{+3} [239]. Luminescence properties of Nd^{+3} doped $\text{Ca}_3\text{V}_2\text{O}_8$ single crystal fiber prepared by floating zone technique were studied, this material was stated as a proposed material for solid-state tunable lasers [240]. Simultaneous doping of Eu and Sm were done in $\text{Ca}_3\text{V}_2\text{O}_8$ lattice using a modified solid-state method. Sm was found to increase the broadness in the excitation wavelengths and simultaneously intensifies the emission bands [241]. A red emitting phosphor was developed by doping Eu^{3+} and Mn^{2+} in $\text{Ca}_3\text{V}_2\text{O}_8$ using citric acid assisted sol-gel technique. Mn^{2+} doping was found to be detrimental to red emission due to the energy transfer from Eu^{3+} to Mn^{2+} [242]. Some phosphors have also been developed to be used in solar cells such as the mixed vanadate $(\text{CaSr})_3(\text{VO}_4)_2: \text{Pr}^{3+}, \text{Eu}^{3+}$ prepared by solid-state reaction. The Sr^{2+} substitution was found to increase the luminescence intensity of the red phosphor. The prepared composition was claimed to be a candidate for Cu Phthalocyanine based solar cells [243]. In another report, the effect of different ratios of Ca and V in a composition on Eu^{+3} emissions was studied. These compositions were prepared by the citric acid assisted method. A composition with the ratio of Ca/V of 3:2.2 was found to be the most efficient given the highest luminescence intensity of Eu^{+3} [244].

It can be seen from the above representative reports, that the solid state technique has been used abundantly in the literature. Some of the methods like coprecipitation [245, 246], hydrothermal [247, 248] and combustions [249] are also used. As it is evident the rare earth ions are used individually or in combinations as the activators in the host materials. The important aspect of doping Rare earth ions is about their concentrations in which they are doped. It is observed that after a certain optimal concentration of Rare earth ions the luminescence intensity decreases. This quenching of the luminescence of Rare earth ions is a peculiar property of lanthanide ions doped in the host lattices. It is observed that when the distance between the neighbouring RE ions decreases in the host systems, the interaction between them increases resulting in the decrease in the luminescence intensity[250, 251].

3. EXPERIMENTAL

3.1 Introduction

Preparation of materials and their systematic physico-chemical characterization is a very important process in material chemistry. Chemists tend to select the preparative methodology that can yield a pure phase material. Along with the formation of pure phase, a control over the texture and morphology of materials is also essential as these parameters influence the performance of the material and therefore, needs special attention in designing the materials. Generally, in catalysis, it is desirable to have catalysts with the very high surface area, but it must also be noted that the aspect of the surface area only comes after the formation of pure phase (or a desirable mixture of phases) of the catalyst. A material with the very high surface area but lacking in crystalline phases responsible for the catalysis will present a no-win situation. In these regards, methodologies that strike a neat balance with both the above-said aspects are ideal. In case of luminescent materials also the phase purity is of utmost importance. A phase pure luminescent material apart from the application point of view offers a secure platform to study the electronic band structure without any perturbation caused by the presence of impurity phases.

Physico-chemical characterization techniques allow a detail evaluation of the preparative methods used. The structure-activity relationships deduced by linking structure of the material and their behaviour give key ideas regarding the changes to be made in the preparative procedure or in the composition of the material itself. A detail characterization, therefore, helps with the underlying principles of structure and activity and also opens up new vistas for further development of materials.

In this chapter, a detailed account of the preparative methods used to prepare the materials under study is presented. The theories and practical procedures behind each characterization technique used such as TG-DTA, X-ray diffraction, IR spectroscopy, Raman spectroscopy, XPS, SEM, and TEM *etc.* are given in detail. Details of instrumentation and brief operating procedures are also discussed.

3.2 Preparation of the materials

In this section, a brief account of the procedures utilized to prepare the studied materials is given.

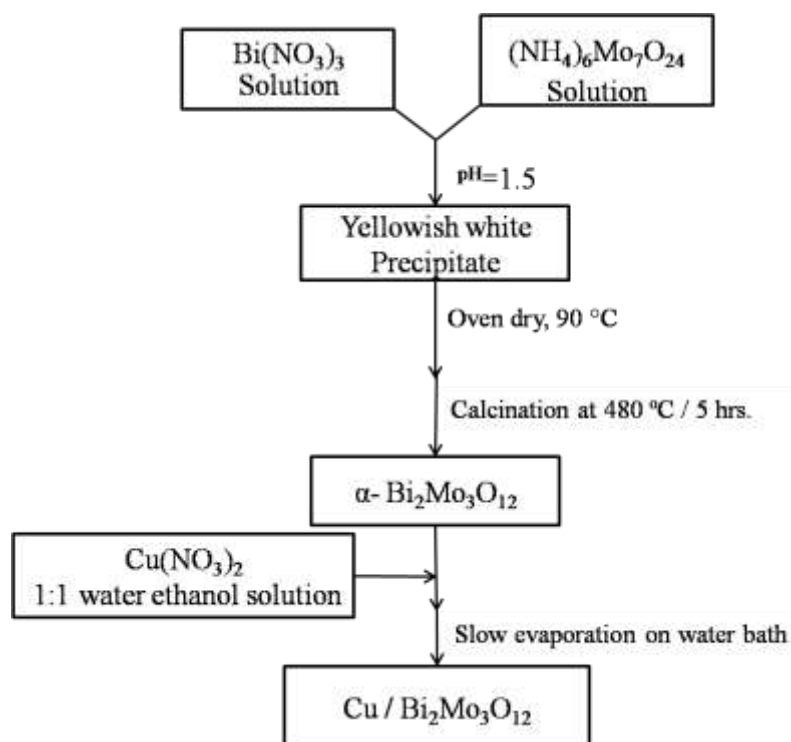
3.2.1 Preparation of Cu/Bi₂Mo₃O₁₂ catalysts

X% Cu/Bi₂Mo₃O₁₂ (X = 2, 4, and 8)

Bi₂Mo₃O₁₂ was prepared by a conventional co-precipitation method. The typical procedure is summarised in the Scheme 3.1. In this process, the calculated amount of Bi(NO₃)₃.5H₂O (Sigma-Aldrich) was dissolved in 10% HNO₃ (Thomas Baker) solution whereas, the calculated amount of (NH₄)₆Mo₇O₂₄ (Sigma-Aldrich) was dissolved in a hot distilled water. The pH of the molybdate solution was kept acidic. After the complete dissolution of both the compounds, the Bi⁺³ solution was added slowly to the molybdate solution. The pH was kept at 1.5 throughout the addition. The ensuing precipitate was kept on stirring for another four hours and was filtered through Buchner funnel on a suction pump. The obtained Bi₂Mo₃O₁₂ precursor was decomposed by calcination at 480 °C for four hours yielding the monophasic Bi₂Mo₃O₁₂ oxide.

Cu impregnated Bi₂Mo₃O₁₂ catalysts were prepared by the wet impregnation method, in this method the desired amount Bi₂Mo₃O₁₂ was weighed in a round bottle flask. The flask containing the powder was kept in an oven for two hours at 120 °C to

drive off the adsorbed moisture and gases. Simultaneously, $\text{Cu}(\text{NO}_3)_2 \cdot 2.5\text{H}_2\text{O}$ (Sigma-Aldrich) corresponding to the desired Cu loading was weighed and dissolved in a minimum quantity of 1: 1 water-ethanol mixture.



Scheme 3.1. The preparative procedure of $\text{Cu}/\text{Bi}_2\text{Mo}_3\text{O}_{12}$ catalysts.

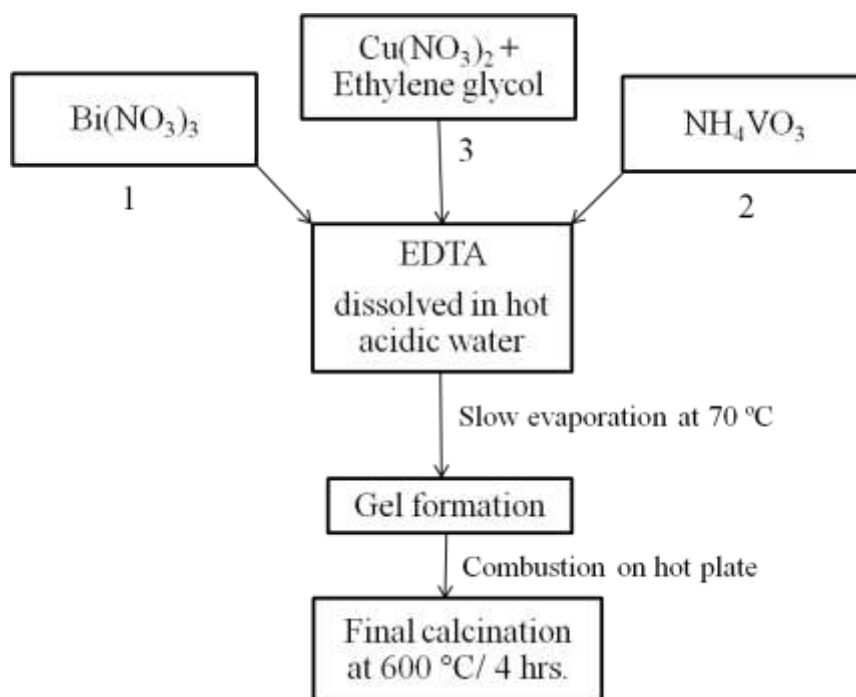
The Cu^{+2} solution was then added carefully drop by drop to the $\text{Bi}_2\text{Mo}_3\text{O}_{12}$ powder so that it completely gets wet. Round bottom flask was then kept on a water bath maintained at 70 °C for the evaporation. The powder was then finally calcined at 450 °C for 1 hr.

3.2.2 Preparation of Cu incorporated $\text{Bi}_4\text{V}_2\text{O}_{11}$

$\text{Bi}_4\text{V}_{2-x}\text{Cu}_x\text{O}_{11}$ ($x = 0.0, 0.1, 0.2, 0.3$ and 0.4)

Scheme 3.2 presents the typical procedure. EDTA sol-gel auto combustion technique was used to prepare these compositions. In this process, EDTA (Thomas Baker) was first dissolved in hot acidic water. To this EDTA solution, calculated

amounts of $\text{Bi}(\text{NO}_3)_3 \cdot 5\text{H}_2\text{O}$ was added first and allowed to form a clear solution. Subsequently, the solutions of weighed quantities of NH_4VO_3 (Sigma-Aldrich) followed by $\text{Cu}(\text{NO}_3)_2 \cdot 2.5\text{H}_2\text{O}$ were added. The solution was kept for stirring on a hot plate maintained at $70\text{ }^\circ\text{C}$ to form a viscous gel.



Scheme 3.2. The preparative procedure of $\text{Bi}_4\text{V}_{2-x}\text{Cu}_x\text{O}_{11}$ composition.

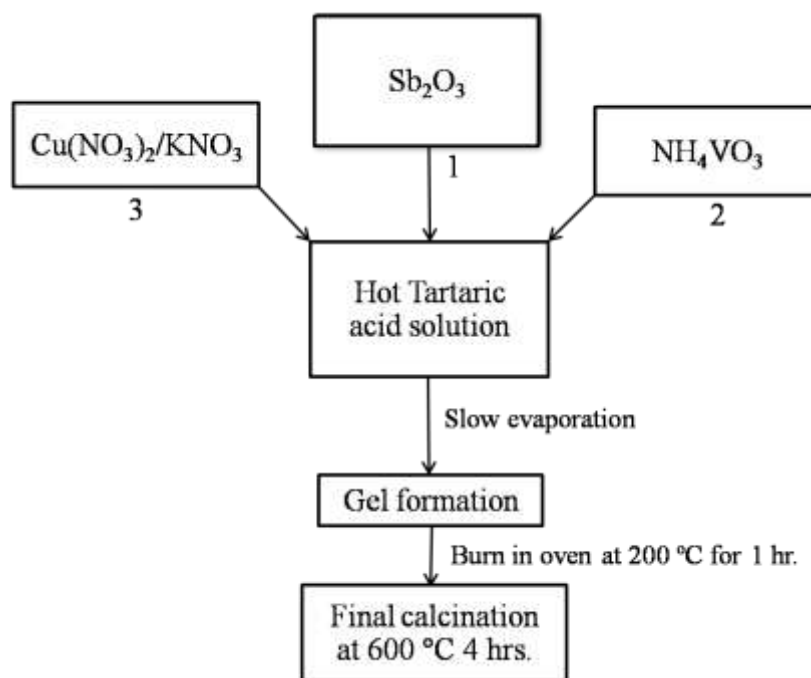
This gel got combusted on a hot plate giving a brown powder which was finally calcined at $600\text{ }^\circ\text{C}$ for 4 hrs. to yield final compositions.

3.2.3 Preparation of VSbO_4 related compositions

$\text{Cu}_x\text{V}_{1-x}\text{SbO}_4$ ($x = 0.0, 0.05, 0.1, 0.2$ and 0.3)

$\text{Cu}_x\text{K}_y\text{V}_{1-x}\text{Sb}_{1-y}\text{O}$ ($x = 0.05, y = 0.02$); ($x = 0.1, y = 0.05$); ($x = 0.2, y = 0.1$); ($x = 0.3, y = 0.15$)

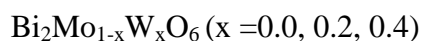
Above compositions were prepared by a Tartaric acid sol-gel process. In the first step tartaric acid (Thomas Baker) was dissolved in distilled water. The tartaric acid solution was made hot by keeping it on hot plate with continuous stirring.



Scheme 3.3. The preparative procedure of VSbO₄ related compositions,

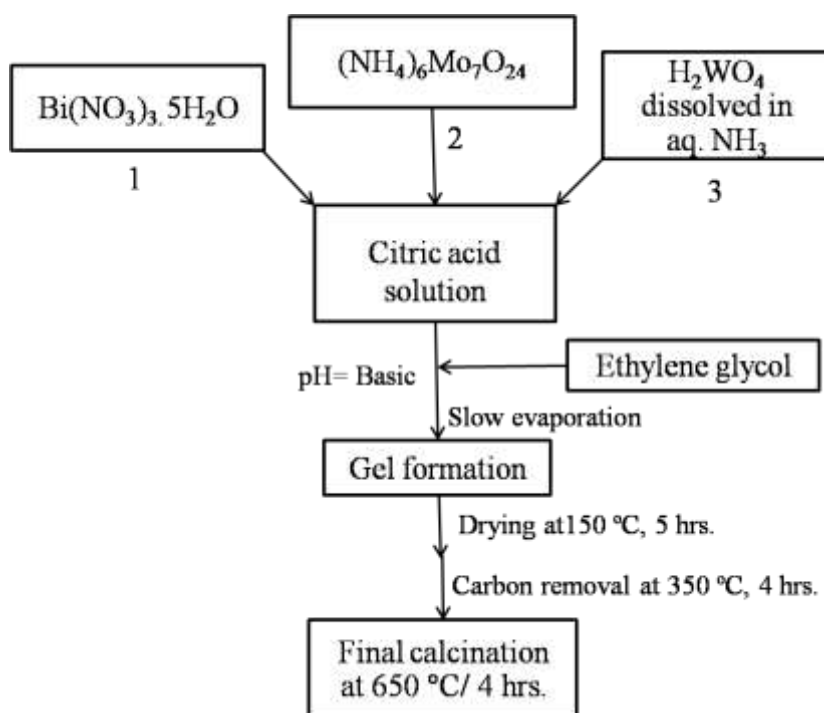
The calculated amount of Sb₂O₃ (SD Fine Chemicals) was weighed and poured into the hot tartaric acid solution with vigorous stirring until the complete dissolution. NH₄VO₃ was dissolved in a separate beaker and was added to the Sb-tartaric acid solution. After the homogenization, the calculated amount of Cu(NO₃)₂·2.5H₂O was added. Stirring and the moderate heat was continued until the formation of a viscous gel. The gel formed was then burnt in a convection oven kept at 200 °C for 1hr. Final calcination was carried out at 600 °C for 4 hrs. A typical procedure is summarised in the Scheme 3.3

3.2.4 Preparation of W inserted Bi₂MoO₆



The Scheme 3.4 displays the typical procedure. In this process, the aqueous solutions of Bi³⁺, Mo⁶⁺, and W⁶⁺ were obtained by carefully weighing the calculated amounts of Bi(NO₃)₃·5H₂O, (NH₄)₆Mo₇O₂₄ and H₂WO₄ (Sigma-Aldrich) respectively.

An aqueous solution of citric acid was prepared by weighing the citric acid (Thomas Baker) corresponding to the molar ratio of 1: 2 to the metal ions. Mo^{6+} and W^{6+} solutions were added to the citric acid solution with constant stirring followed by the addition of Bi^{3+} solution. The resultant solution was kept on stirring with the moderate heating.



Scheme 3.4. The preparative procedure of $\text{Bi}_2\text{Mo}_{1-x}\text{W}_x\text{O}_6$ system.

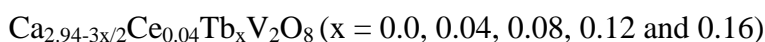
All along this process, the pH of the solution was kept basic so as to prevent the precipitation. As the evaporation leads to the gellation, obtained gel was dried in an oven at 150 °C. The residual carbon in the precursor was removed at 350 °C followed by the final calcination at 650 °C for 4 hrs.

3.2.5 Preparation of Alkaline earth vanadates and RE-doped $\text{Ca}_3\text{V}_2\text{O}_8$

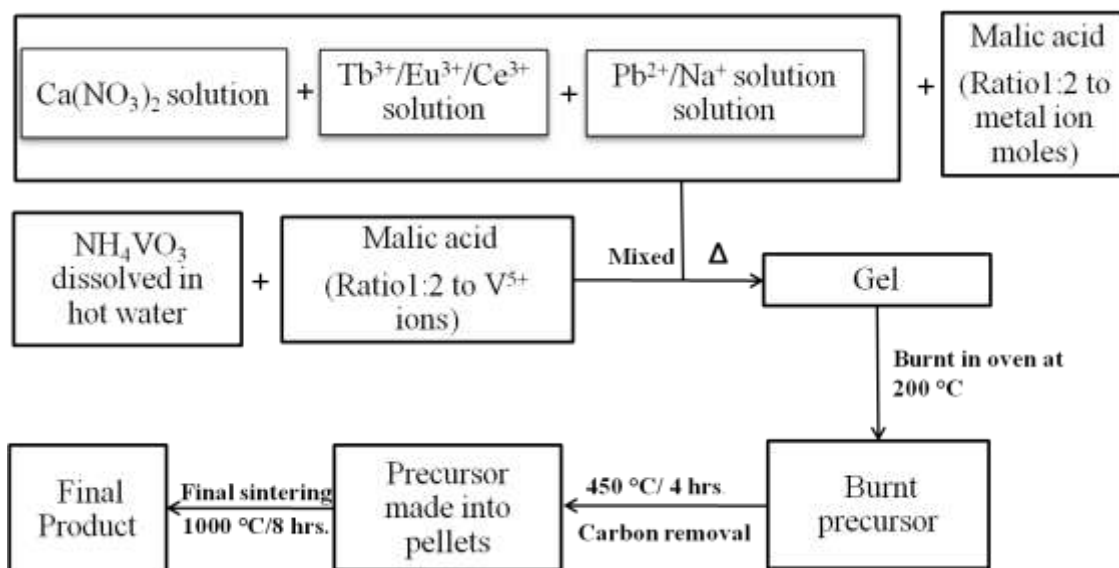
$\text{M}_3\text{V}_2\text{O}_8$ (M = Ca, Sr and Ba)

$\text{Ca}_{3-3x/2}\text{Tb}_x\text{V}_2\text{O}_8$ (x = 0.04, 0.08, 0.12, 0.16 and 0.20)

$\text{Ca}_{3-2x}\text{Tb}_x\text{Na}_x\text{V}_2\text{O}_8$ (x = 0.04, 0.08, 0.12, 0.16 and 0.20)



All the above series were prepared by a Malic acid assisted sol-gel process. The typical procedure can be described as follows. In accordance of the respective compositions, $\text{Ca}(\text{NO}_3)_2 \cdot 4\text{H}_2\text{O}$ (Sigma-Aldrich), $\text{Sr}(\text{NO}_3)_2$ (Sigma-Aldrich), $\text{Ba}(\text{NO}_3)_2$ (Sigma-Aldrich), Na_2CO_3 (Thomas Baker), $\text{Tb}(\text{NO}_3)_3 \cdot 5\text{H}_2\text{O}$ and $\text{Ce}(\text{NO}_3)_3 \cdot 6\text{H}_2\text{O}$ (Both Sigma-Aldrich) were dissolved in distilled water. This was the cationic solution. Water-insoluble oxide Eu_2O_3 (Sigma-Aldrich) was dissolved in a minimum quantity of Nitric acid and was added to the cationic solution. NH_4VO_3 was dissolved in a hot water. Malic acid (Thomas Baker) corresponding to the ratio of 1: 2 to the total metal ions was weighed. Malic acid was added separately to the cationic solution and NH_4VO_3 solution.



Scheme 3.5. The preparative procedure of RE-doped $\text{Ca}_3\text{V}_2\text{O}_8$.

After the complete dissolution of all the components, both the solutions were mixed; the resultant solution was stirred and heated slowly on a hot plate for the evaporation. The solution proceeded to form a gel. This gel was heated in an oven at

200 °C to give a carbonaceous precursor which was then ground in a mortar and pestle. The powder obtained was then calcined at 450 °C for the removal of carbon. Final sintering was done at 800 °C for pure alkaline earth metal vanadates, whereas R.E-doped Calcium vanadates were sintered at 1000 °C in the form of pellets. The procedure is summarised in the Scheme 3.5.

3.3 Characterizations: Theoretical background and practice

3.3.1 Thermogravimetric-Differential Thermal Analysis (TG-DTA)

TG-DTA analysis, as the name suggests is the technique in which the sample under study is steadily heated with a predetermined heating rate from ambient temperature to the desired higher temperature in a controlled atmosphere. The effect of the steady increase in the temperature on the sample is studied which gives the information such as the thermal stability of the material and its composition. In this technique, the two crucibles, one reference, and another containing sample are heated simultaneously. As the temperature is increased, the temperature of the sample crucible increases or decreases depending on the exothermic or endothermic process. The change in temperature with respect to the reference crucible is then quantified in terms of the electric signal which forms the basis for the DTA curve. Similarly, the microbalance checks the minute changes in the weight of the sample giving TG curve as an output.

NETZSCH STA TG-DTA instrument was used for our studies. The temperature was increased from ambient temperature to the desired higher temperature at the rate of 10 °C/minute in an air atmosphere. Recrystallized alumina crucibles were used as the sample holders. Reference crucible was kept empty whereas the sample crucible contained the compound under study. The analysis sample was usually weighed

between 10-15 mg. The TG-DTA curves obtained were mainly used to know the decomposition patterns and to decide over the final calcination temperature of the metal oxide precursors. Thermal stability of the prepared oxide compositions was also evaluated.

3.3.2 X-ray diffraction (XRD)

Powder X-ray diffraction is the most important and basic technique utilized by the chemists for structural characterization of crystalline compounds. Phase purity, crystallinity, average crystallite size, grain boundaries, unit cell parameters and lattice constants are some of the important data that can be deciphered from the XRD powder patterns. Monochromatic X-rays (mostly Cu- α radiations) get diffracted when they strike the systematic arrays of atoms called planes. The X-rays are made incident on a material at different angles, if the condition called as the Bragg's law is met then the diffracted beams will interfere constructively and the peak will appear at the respective diffracting angle. The Bragg's law is given by the following equation,

$$n\lambda = 2d \sin\theta$$

Where, 'n' is the order of diffraction, ' λ ' is the wavelength of incident radiation, 'd' is the inter-planar distance and ' θ ' is the angle of incident radiation. Each plane will show its peak at its characteristic angle thus this information can be used to find their interplanar distances and can be compared with the standard JCPDS data card of the respective material for the confirmation of phase purity. The diffraction analysis were carried out on RIGAKU ULTIMA IV X-ray diffractometer using Cu-K α line (1.5418 Å) filtered through Ni absorber.

3.3.3 Infrared spectroscopy (IR)

Infrared spectroscopy is an important technique classified under the name 'Vibrational spectroscopy'. As the name suggests the technique mainly deals with the change in vibrational energy levels of a compound. When the radiations from the middle-infrared region (from 200 - 4000 cm^{-1}) strike a molecule, they have sufficient amount of energy to cause transitions from vibrational ground states to excited states. An important criterion for this to occur is that the molecule should possess a permanent dipole moment. Homo-nuclear molecules such as N_2 or O_2 which does not have any dipole moment are therefore found to be IR inactive. As the molecule with dipole moment stretches, contracts or bends it absorbs the energy resonant with its frequency of vibration and this leads to the IR spectra. More the change in dipole moment more will be the intensity of the infrared band.

An infrared spectrum is a very important tool in detecting the purity of the material and is mainly used in the organic chemistry. IR spectroscopy can also provide a very good picture of the M-O bonding in the metal oxide systems. The shifts in the IR bands in solid solution or difference in the pristine and doped IR spectra can provide important information regarding the structure. Infrared spectra in our studies were recorded on SHIMADZU FTIR Prestige-21 spectrophotometer. The sample was ground finely with KBr powder and was filled in the sample holder mounted on an aperture where it was irradiated with the IR radiations and the spectra were recorded.

3.3.4 Raman spectroscopy

Raman spectroscopy is the vibrational spectroscopy which is based on Raman Effect. Raman Effect states that when a monochromatic radiation is incident on a material, it scatters this radiation unchanged called as Rayleigh scattering but in

addition to this wavelength, there are radiations of higher and lower wavenumbers that are scattered, these are the result of inelastic scattering. In other words, the material takes up some part of the energy of the incident radiations. Therefore, the radiation emitted out will be lower in wavenumbers this lower shift is called as the Stokes shift. Similarly, when the molecules are already in the excited state they transfer their extra energy to the radiation shifting the scattered radiation to the higher wavenumbers and this shift is called as Anti-stokes shift. The intensities of the Stokes lines are always higher than the Anti-stokes lines at room temperature as the lower energy levels are more populated than the excited levels. Therefore, stokes lines are recorded in the routine measurements.

Raman spectroscopy gives information regarding the local structure of crystalline materials, M-O bondings in metal oxide and crystallinity. This information forms complementary data set to the information provided by the IR spectroscopy. Raman spectroscopic measurements were carried out on STR-500 Confocal micro Raman spectrophotometer.

3.3.5 Ultraviolet Diffuse Reflectance (UV-DRS) spectroscopy

UV-DRS is a reflectance spectroscopy. In this technique, the solid film or powder of infinite thickness is irradiated with radiations ranging from 200-800 nm, and the diffuse reflectance emitted out by the sample is collected in an integrating sphere which is then fed to the detector. Along with the sample material, another reference material of infinite thickness having zero absorbance or 100% reflectance is taken. So the reflectance of the sample is the relative reflectance with respect to the reference material. As the sample is irradiated at zero angles, only the diffuse reflectance is collected by the integration sphere leaving out the Specular reflections.

This technique provides handy information regarding the outer orbital electron of the atoms of a molecule or an oxide system and thus information regarding the bonding state and electronic environment could be retrieved. This technique is majorly used for optical band gap determinations of semiconductor systems by locating the band edge in nm which can be utilized to give the optical band gap of the material according to the following formula.

$$\text{Band gap (eV)} = 1240/\lambda \text{ (in nm)}$$

In the present studies, the band gap of the compositions was determined by using the expression for the band gap given by Tauc. The relation is called as Tauc equation given below.

$$(\alpha h\nu)^2 = A (h\nu - E_g)$$

Where ‘ α ’ is the absorption coefficient, ‘ h ’ is the Planck’s constant, ‘ ν ’ is the frequency of radiation, ‘ A ’ is the proportionality constant and ‘ E_g ’ is the band gap of the material. As can be observed from the equation above, the equation is in the form of straight line. All the terms except ‘ E_g ’ are known. Therefore, a plot of $(\alpha h\nu)^2$ vs $h\nu$ was plotted. The point of inflection of the plot was extended to the x-axis by marking the tangent. The point of intersection of the tangent on x-axis gave the value of band gap in eV. The Diffuse reflectance spectra were obtained from Shimadzu UV 2450 UV-Visible spectrometer. The spectra were recorded from 200- 800 nm. BaSO₄ was used as the reference material.

3.3.6 Scanning electron microscopy (SEM)

SEM comes under a broader category of microscopy technique called as electron microscopy. In SEM a focussed beam of electrons is utilized to scan the surface of the electrons to produce the images. Interactions of the electrons with the material surface give rise to different types of signals such as secondary electrons and

backscattered electrons which can procure information regarding composition and topology of the sample. The most common SEM microscopes work on the principle of a collection of secondary electrons emitted by the material excited by the focussed electron beam. As the secondary electrons are emitted from the close vicinity of the specimens surface images of very high resolution can be obtained. Electron beams of about 5-50 eV are used giving the resolution of around 5 nm. SEM studies were performed on Nova Nano FESEM- 450 and ZEISS EVO 18 instruments.

3.3.7 Transmission electron microscopy (TEM)

This electron microscopy works on similar lines to that of a light microscope. Only in this case instead of light, an electron beam is used. In this technique, an electron beam is made to pass through a very thin material of the order of 100 nm thicknesses or a suspension mounted on a grid. The image is generated by the interaction of the electron beam with the sample as it is transmitted through. The images are recorded on a fluorescent background or a photographic film. The images are also captured with the help of CCD cameras. Due to very small de Broglie wavelengths of the electron, the resolution obtained through TEM is very high. A cluster or an array of atoms could be observed with great detail. TEM for an inorganic chemist provides information such as particle size and crystallinity of the material. TEM images were obtained from PHILIPS CM 200 Transmission electron microscope operating at accelerating voltage 200 kV with a resolution of 2.4 Å.

3.3.8 X-ray photoelectron spectroscopy (XPS)

This technique is a consequence of photoelectric effect. In this technique, the sample material is bombarded with the high energy x-rays. This bombardment knocks

out the electrons from the atomic orbitals of the constituent elements. The number and kinetic energies of these emitted electrons are measured since kinetic energies of these electrons can supply important information regarding the oxidation states of the elements.

Binding energies of the inner orbital electrons of the elements are very much dependent on the oxidation states of the elements and therefore the change in the oxidation state and electronic environment can be easily monitored by measuring the kinetic energies of outgoing electrons. The number of electrons emitted can give the quantitative estimate of the particular element in the sample material. XPS could be used for the quantitative measurements by applying the properly calibrated quantification factors. In XPS, the atoms of only the uppermost layers of the sample material could be ionized, at the most 5 nm in depth, this renders XPS a tag of very sensitive surface technique. The XPS measurements were carried out on Omicron ESCA instrument supplied by Oxford instruments, Germany using the radiation of Al- α (1486.7 eV). The resolution of the instrument was 0.6 eV.

3.3.9 Photoluminescence spectroscopy

Luminescence spectroscopy is a non-destructive optical spectroscopy. The interactions of the electromagnetic radiations with the electrons located at different energy levels is studied, this gives the information regarding the locations of filled energy levels, levels of impurity, mechanisms of electron-hole combinations *etc.* The radiations with the energy higher than that of the band gap of the material when incident on the material leads to the excitation of the electrons from the lower energy levels to the higher energy levels. The energy levels from where the electrons are raised in the energy are called as the ground state energy levels whereas; the energy levels to

which the electrons are raised are called as the excited state energy levels. Once the electrons are at the excited level, they will look out to dissipate the extra energy acquired which is achieved by radiative or non-radiative relaxation processes. Non-radiative processes include the loss of the energy in form of heat or transfer of energy to the neighbouring atoms and so on. Radiative relaxation processes are the ones in which the energy is lost in the form of radiations. These radiations most of the times fall in the visible region but sometimes can also fall in the infrared region of the spectrum. The radiative processes depending on their timescale of occurrence are labeled as either fluorescence or phosphorescence. Fluorescence occurs very fast after the absorption and occurs from the spin allowed state, whereas phosphorescence is a delayed process and takes place from a spin-forbidden state. The delay is due to the phenomenon called as the intersystem crossing. Both the above said relaxation processes are collectively termed as luminescence.

Luminescence spectroscopy mainly deals with the absorption and emission of radiations with the related processes such a quantum yield and lifetime. Quantum yield can simply be defined as the ratio of quanta of the radiations emitted to the quanta of the radiation absorbed; it is a very important criterion for any luminescent material or more specifically for a phosphor. Lifetime is the resident time of the system in the excited state. Luminescence spectroscopy is usually carried out in two forms one is steady state spectroscopy and the other one is lifetime analysis. In the steady state technique, the material is continuously excited with the wavelengths and the emission patterns are recorded. In this spectroscopy all the luminescence centres are excited, and sometimes if the two components overlap each other but are from different luminescent centres then the differentiation could become a cumbersome job. Lifetime technique or the time-resolved technique actually detects the decay time of the luminescent centres

and the different luminescent centres have their own decay time which is a major cue for differentiation. A minor luminescent centre that gets buried in the steady-state spectrum could be detected making use of the time resolve technique.

A luminescence spectral study usually consists recording of two types of spectra namely, emission spectra and excitation spectra. Emission spectra record all the emissions in the range of wavelengths at a particular excitation wavelength whereas; the excitation spectra measure the luminous intensity in the range of the excitation wavelengths by monitoring a particular emission.

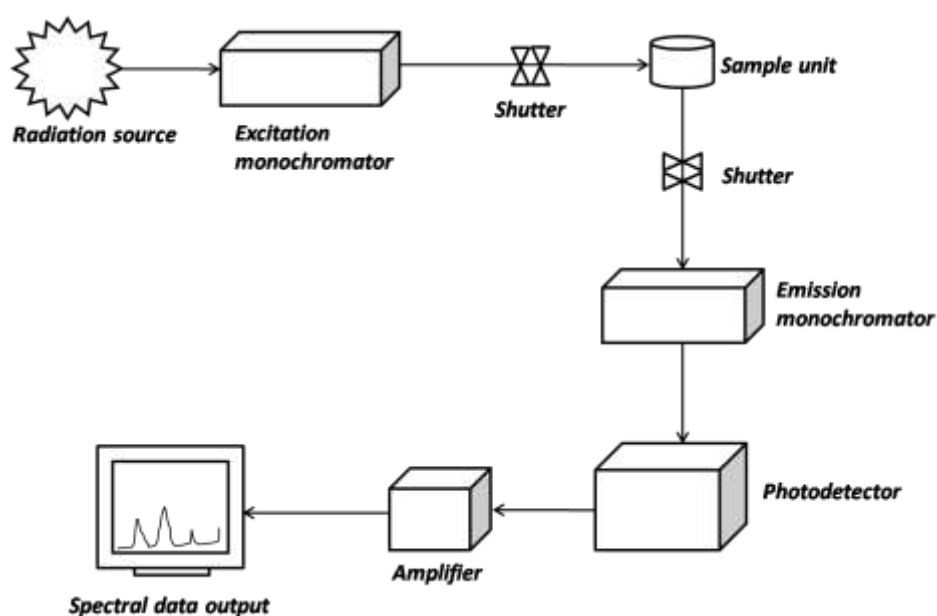


Fig. 3.1. A schematic block diagram of the spectrofluorimeter

A spectrofluorimeter consists of following basic parts, a UV lamp, an excitation monochromator, sample compartment an emission monochromator and a detector in the form of the photomultiplier tube. A schematic block diagram showing all the basic components of the spectrofluorimeter is presented in Fig.3.1. The luminescence studies were done on PTI Quanta Master steady state instrument supplied by HORIBA

scientific. The step size of 0.05 nm was used for the measurement with the integration time of 1s. All the samples were used in pellet form for the spectral analysis.

3.3.10 BET surface area measurements

Brunauer-Emmett-Teller theory explains the adsorption of the gases on the solid surfaces. Stephen Brunauer, Paul Emmett, and Edward Teller first proposed this theory in the year 1938. Multilayer adsorption of the gases can be explained nicely using this concept. BET theory can be considered as an extension of the Langmuir theory which provides a very good picture of monolayer adsorption of the gases. The main hypotheses can be accounted as follows,

1. Gas molecules can get adsorbed on the solid surface forming infinite layers.
2. Gas molecules adsorbed can interact with the molecules adsorbed adjacently.
3. Langmuir theory can be applied to each adsorbed layer in the multilayer.

Following equation presets basic form of BET theory,

$$\left[\frac{1}{V_a \left(\frac{P_0}{P} - 1 \right)} \right] = \frac{C-1}{V_m C} \times \frac{P}{P_0} + \frac{1}{V_m C}$$

Where P and P₀ are the equilibrium and saturation vapour pressures of the adsorbing species on the material surface at the adsorption temperature. V is the quantity of gas adsorbed whereas; V_m is the volume of the monolayer gas adsorbed. C is the experimental constant in the equation. The BET equation takes the form of a straight line. P, P₀ and V are known whereas; C and V_m are obtained from the graph. Surface area is then calculated using the following equation,

$$\text{Surface area} = \frac{N V_m S}{V}$$

Where 'N' is the Avogadro number, 'S' is the area of the cross-section of the adsorbed gas molecule and 'V' is the molar mass of the adsorbed gas molecule. According to the BET theory, it was also proposed that the monolayer adsorption was only possible at lower partial pressures and therefore the gas adsorbed is directly proportional to the surface area of the material. The gases that usually do not react with the surface of the material are used for the surface area determination. Most commonly used gas is N₂ at its boiling point (77 K). Surface area measurement is not an absolute measurement, as the values obtained are dependent on adsorbing gas used and its interaction with the surface, the cross-sectional area of the adsorbate *etc.*

The surface area of the prepared compositions was measured on the instruments SMART SORB 90/91 and QUANTACHROME AUTOSORB IQ-MP-C. The compositions were finely ground and heated at 200 °C for two hours in the N₂ atmosphere prior to analysis. Surface area was measured using N₂ as an adsorbate at liquid Nitrogen temperature.

3.3.11 Catalytic activity measurements

The set-up used to carry out the catalytic activity measurements is displayed in the Fig.3.2. Catalytic measurements of partial oxidation of propene to acrolein were carried out in a fixed bed catalytic reactor made up of Borosil glass with an internal diameter of 10 mm. Each time, 2.0 g of the catalysts was loaded in the catalytic reactor. The space above the catalyst bed was filled with glass wool and porcelain pieces for the preheating of the gaseous reaction mixture. The glass reactor was placed in the tubular furnace which could reach the maximum temperature of 800 °C. The temperature was monitored using a thermocouple placed in the thermocouple pocket just above the catalyst bed.

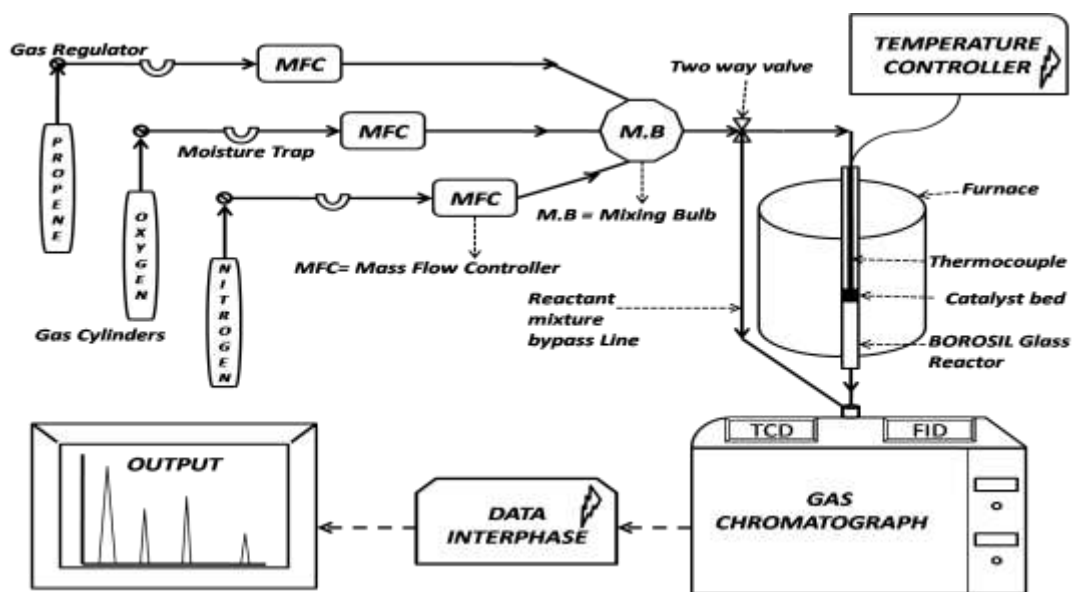


Fig.3.2 A schematic diagram showing the set-up for catalytic activity measurements.

A temperature programmer was used to supply the steady power to the furnace to maintain the desirable heating rate. Reaction gas mixture consisting of 5% propene, 5% oxygen diluted in Nitrogen was used. The total gas flow was kept at 5000 mL/hr. Before starting the actual reaction, the catalyst was heated at 150 °C for 1 hr. in the O₂ stream (250 mL/hr) to drive off the moisture and adsorbed gases on the catalyst.

The gas flows of all the gases were monitored by Mass Flow Controllers (MFC). MFC of make Serra was utilized for controlling the oxygen flow rate and MFCs of Aalborg were utilized to monitor the propene and nitrogen flows. The reactants and the products were monitored on NUCON 5765 Gas chromatograph equipped with Thermal conductivity detector (TCD) and Flame ionization detector (FID). GC columns such as Porapak-Q, Molecular sieve-13x and capillary column were used to identify the reactants and the products. Propene, acrolein, acetaldehyde and CO₂ were analyzed on Porapak-Q column using FID whereas, CO and N₂ were monitored on Molecular sieve-13x column using TCD. The gaseous product mixture was injected periodically in the capillary column to detect any miscellaneous product. Highly pure zero air and H₂

cylinders were used for the FID flame. The carrier gas used was high purity Argon. The column oven was maintained at 140 °C whereas; both the detectors were heated and maintained at 160 °C. The standard solutions and gas mixtures were used to locate the retention time of reactants and products on the respective columns. The concentration calibrations on GC for all the reactants and products were done using the dilute standard solutions and gas mixtures.

The conversion of the propene was calculated based upon the carbon balance. The concentration of propene in the inlet stream and the concentration of the products containing the carbon in the outlet stream were measured. The miscellaneous products if at all formed during the reaction were considered to be negligible and were not considered in the carbon balance. The conversion of propene was calculated as follows.

$$\text{C}_3\text{H}_6 \text{ conversion} = \frac{[\text{No. of moles of C}_3\text{H}_{6(\text{in})} - \text{No. of moles of C}_3\text{H}_{6(\text{out})}] \times 100}{\text{Number of moles of C}_3\text{H}_{6(\text{in})}}$$

The selectivity towards the products acrolein, acetaldehyde and CO_x was calculated as using the following formulae.

$$\text{Acrolein (C}_3\text{H}_4\text{O) selectivity (\%)} = \frac{[\text{No. of moles of C}_3\text{H}_4\text{O}] \times 100}{\text{No. of moles of C}_3\text{H}_6 \text{ converted}}$$

$$\text{Acetaldehyde (C}_2\text{H}_4\text{O) selectivity (\%)} = \frac{[\text{No. of moles of C}_2\text{H}_4\text{O}] \times 100}{\text{No. of moles of C}_3\text{H}_6 \text{ converted}}$$

$$\text{CO}_x \text{ selectivity (\%)} = \frac{[\text{No. of moles of CO/CO}_2] \times 100}{\text{No. of moles of C}_3\text{H}_6 \text{ converted}}$$

4. CHARACTERIZATION AND SPECTRAL STUDIES

4.1 Thermal analysis

The mass loss and thermodynamic events (exothermic and endothermic events) that occur during the decomposition of metal oxide precursors were monitored using their respective TG-DTA curves. These curves aided in finalising the calcination temperature to decompose metal oxide precursors derived from the sol-gel and co-precipitation techniques. TG-DTA curves also furnished valuable information regarding the thermal stability of metal oxides and also helped in setting the optimum sintering temperature in case of doped metal oxide compositions.

4.1.1 $\text{Bi}_2\text{Mo}_3\text{O}_{12}$ co-precipitated precursor

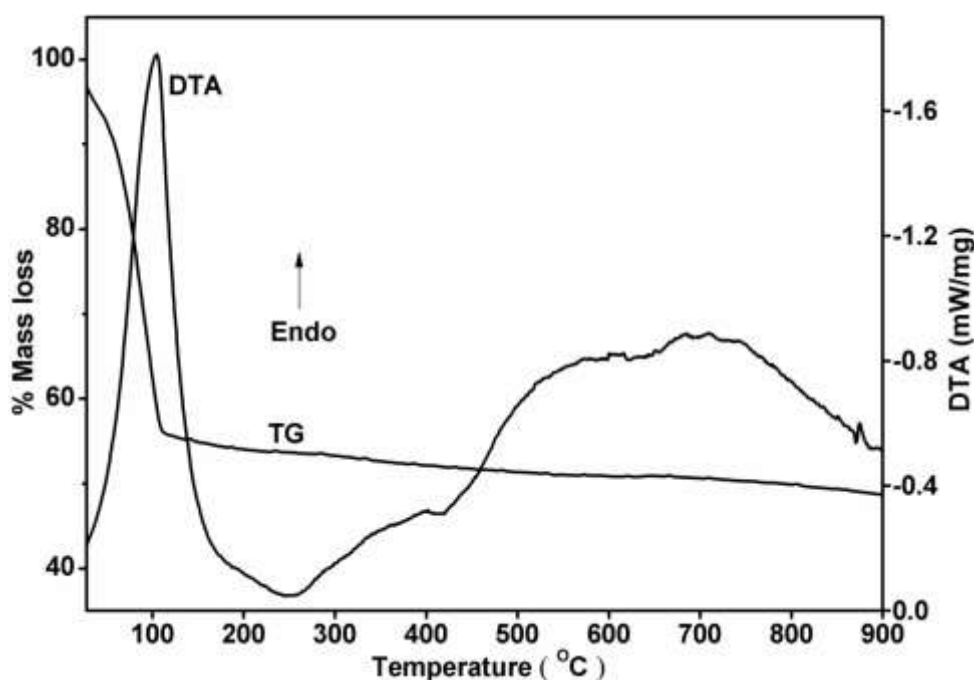


Fig. 4.1 TG-DTA curve of $\text{Bi}_2\text{Mo}_3\text{O}_{12}$ precursor

Fig. 4.1 displays the TG-DTA curve of $\text{Bi}_2\text{Mo}_3\text{O}_{12}$ precursor obtained from co-precipitation. The endothermic peak in DTA is centred on 120 °C. This peak is attributable to the loss of water. The mass loss for this step was found to be almost 50

%, which indicates that the adsorbed water is not the only source of lost water. The amount of water lost hints that the bismuth is precipitated as molybdate in a hydrated form. After this endothermic event, no significant changes in either TG or DTA curves were seen. The broad hump in case of DTA seen in the temperature range from 300 °C to 900 °C was considered a baseline fluctuation as the corresponding temperature region in the TG curve showed almost constant weight loss.

4.1.2 Bi₄V₂O₁₁ precursor

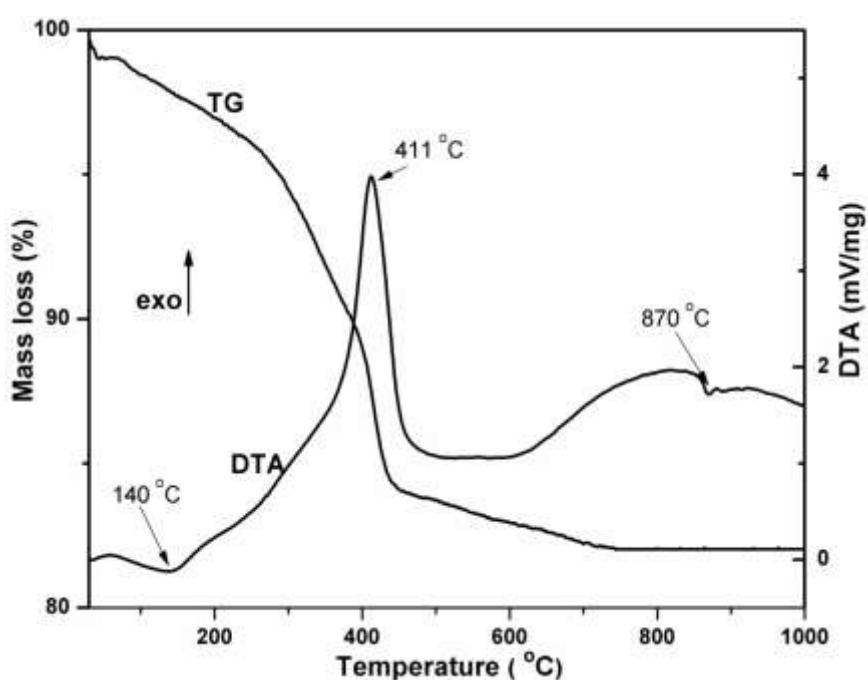


Fig. 4.2 TG-DTA curve of Bi₄V₂O₁₁ precursor

Fig. 4.2 presents the TG-DTA curve of Bi₄V₂O₁₁ precursor as an outcome of EDTA sol-gel auto combustion process. A broad endothermic depression starting from 100 °C and centred on 140 °C is attributed to the loss of residual moisture from the sample. The mass loss that corresponded to this event was negligible. An intense exothermic peak was observed at 411 °C which can be assigned to the exothermic decomposition of the residual organic matter. The total mass loss observed for the above two events was found to be less than 20%. It is found that the majority of the

organic matter is decomposed during the combustion on the hot plate. Therefore, the resultant precursor is devoid of the organic matter that could have been present if the gel only charred. It seems that the nitrates added through Nitric acid to dissolve the $\text{Bi}(\text{NO}_3)_3$ and EDTA drives the autocombustion on the hot plate resulting in the decomposition of major part of organic matter. After the exothermic event at 411 °C, an endothermic event was traced at 870 °C in DTA curve which is attributable to the melting point of $\text{Bi}_4\text{V}_2\text{O}_{11}$ composition [252]. TG curve did not show any mass loss after 650 °C.

4.1.3 VSbO₄ precursor

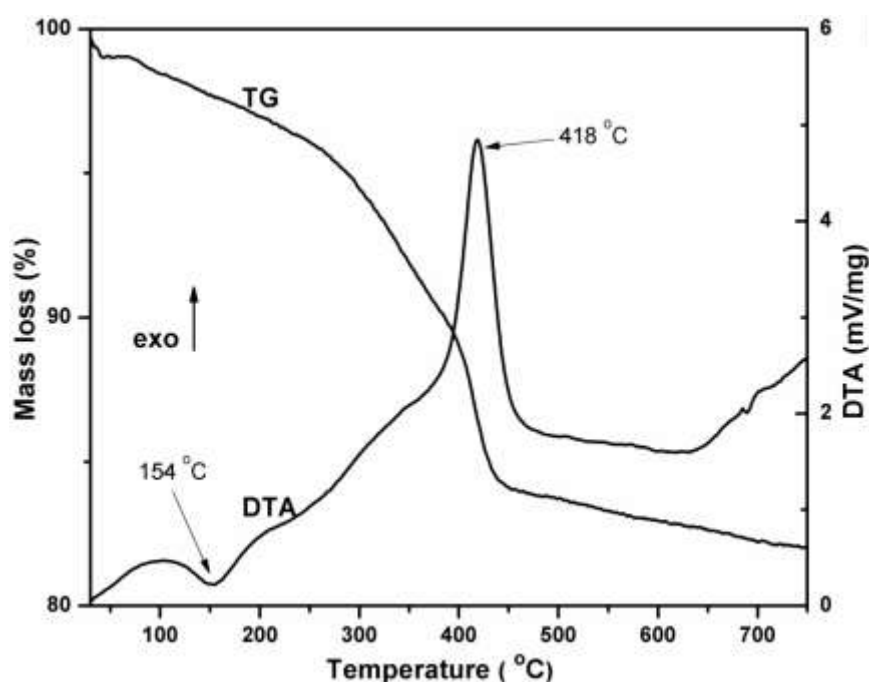


Fig. 4.3 TG-DTA curve of VSbO₄ precursor

Fig. 4.3 display the TG-DTA curve of VSbO₄ precursor obtained through the tartaric acid sol-gel route. An endothermic event centred at 154 °C was the usual loss of moisture from the precursor. A negligible mass loss in the TG curve corresponding to the endothermic event was seen. An intense exothermic peak was observed at 418 °C which is assigned to the exothermic decomposition of organic matter into gaseous

products like Carbon oxides. After this, no significant events were observed in both TG and DTA curves.

4.1.4 $\text{Bi}_2\text{Mo}_{1-x}\text{W}_x\text{O}_6$ citrate precursor

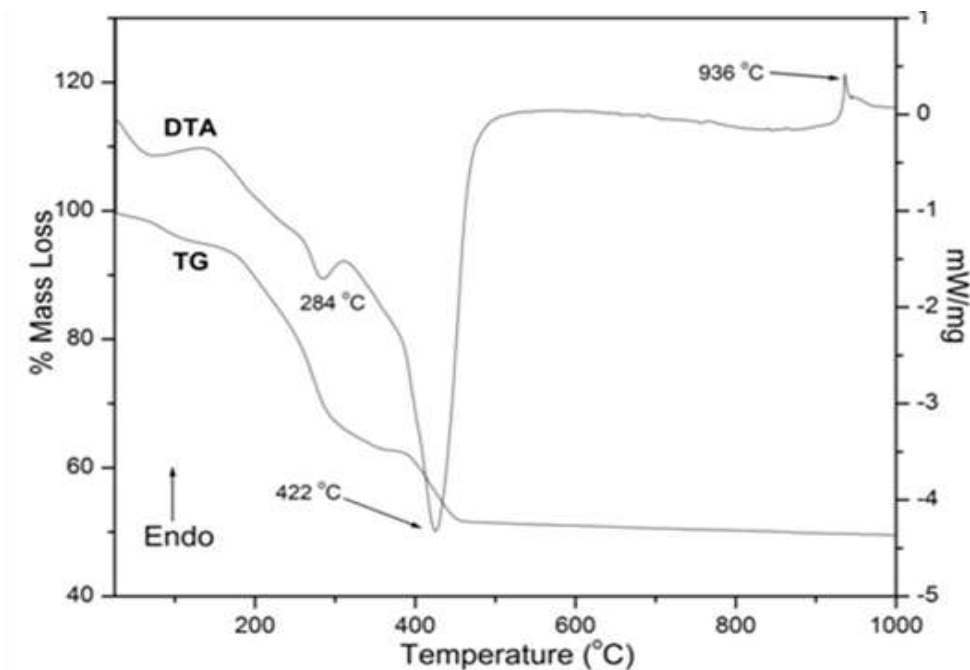


Fig. 4.4 TG-DTA curve of Bi_2MoO_6 precursor

The TG-DTA curve of the Bi_2MoO_6 precursor is presented in Fig. 4.4. The citrate precursor showed mass loss in three distinguishable regions having a major exothermic peak at 445 °C. Most of the overall mass loss corresponds to the removal of H_2O and decomposition of the organic matter. The mass loss region from 30 °C - 200 °C indicates the loss of physisorbed and constitutional water from the precursor. A small endothermic peak at 100 °C is due to the loss of this water. The mass loss in the region from 200 °C– 400 °C corresponds to the initial decomposition of organic moieties, which is characterized by an exothermic peak at 284 °C in the DTA curve. The mass loss region from 400 °C - 530 °C is due to the decomposition of remaining organic matter. The strong exothermic peak at 422 °C is due to the redox decomposition of carboxylate and nitrate moieties leading to the evolution of Carbon oxides and NO_x .

No signals were observed in either TG or DTA curve in the temperature region from 530 °C to 900 °C. Based on these observations the compounds were finally sintered at 650 °C. A strong endothermic peak observed at 936°C indicated the melting point of Bi_2MoO_6 .

4.1.5 $\text{M}_3\text{V}_2\text{O}_8$ precursors (M = Ca, Sr and Ba)

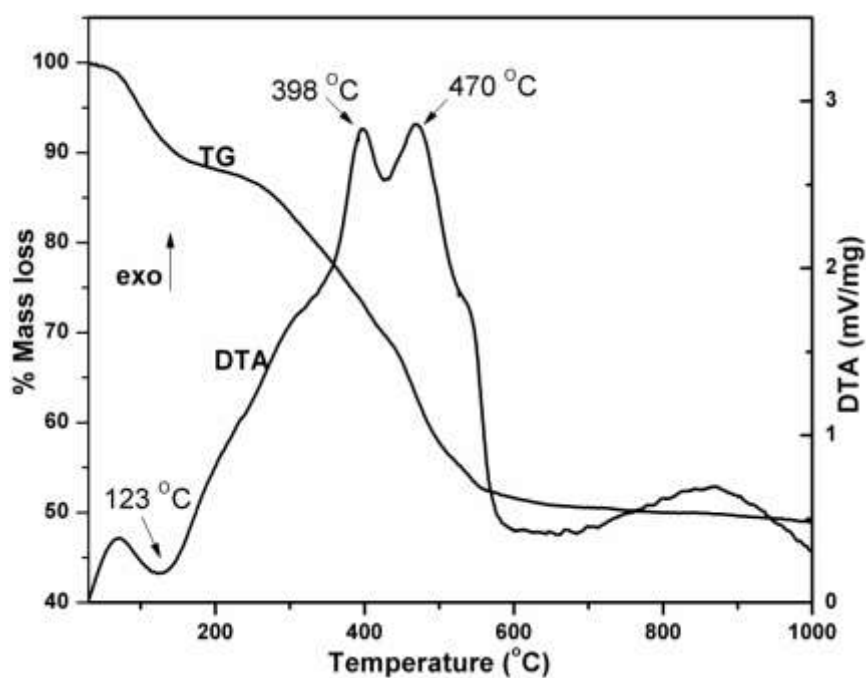


Fig. 4.5 TG-DTA curve of $\text{Ca}_3\text{V}_2\text{O}_8$ precursor

Figs. 4.5, 4.6 and 4.7 display the TG-DTA curves of $\text{Ca}_3\text{V}_2\text{O}_8$, $\text{Sr}_3\text{V}_2\text{O}_8$ and $\text{Ba}_3\text{V}_2\text{O}_8$ precursors respectively. The precursors were as burnt outcomes of the malic acid sol-gel process. All the precursors showed almost identical decomposition pattern. An initial endothermic peak was observed and is attributed obviously to the loss of water from the precursor. Although a small difference in temperature at which the endothermic peak is centred was noticed among the precursors, but the overall temperature range that was spanned was same in all the precursors.

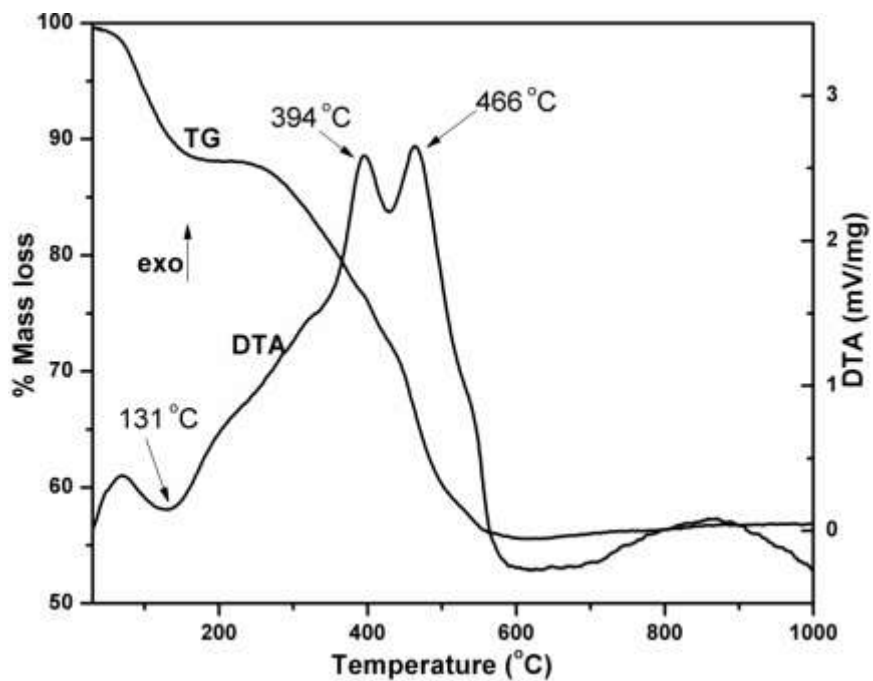


Fig. 4.6 TG-DTA curve of $Sr_3V_2O_8$ precursor

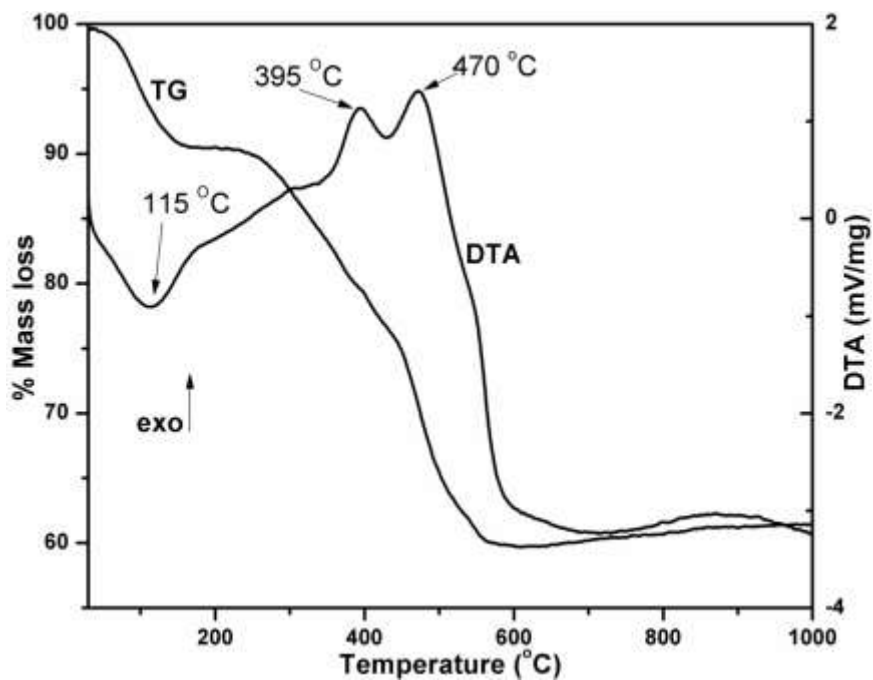


Fig. 4.7 TG-DTA curve of $Ba_3V_2O_8$ precursor

The evaporation of water was followed by two successive exothermic peaks observed at around 390 °C and 470 °C respectively in all the precursors. These peaks are attributed to the exothermic decomposition of organic matter. The complete removal of organic matter was complete after 600 °C. After which there were no significant

changes in both TG as well as DTA curves highlighting the thermal stability of alkaline earth metal orthovanadates.

4.1.6 RE-doped $\text{Ca}_3\text{V}_2\text{O}_8$ precursors.

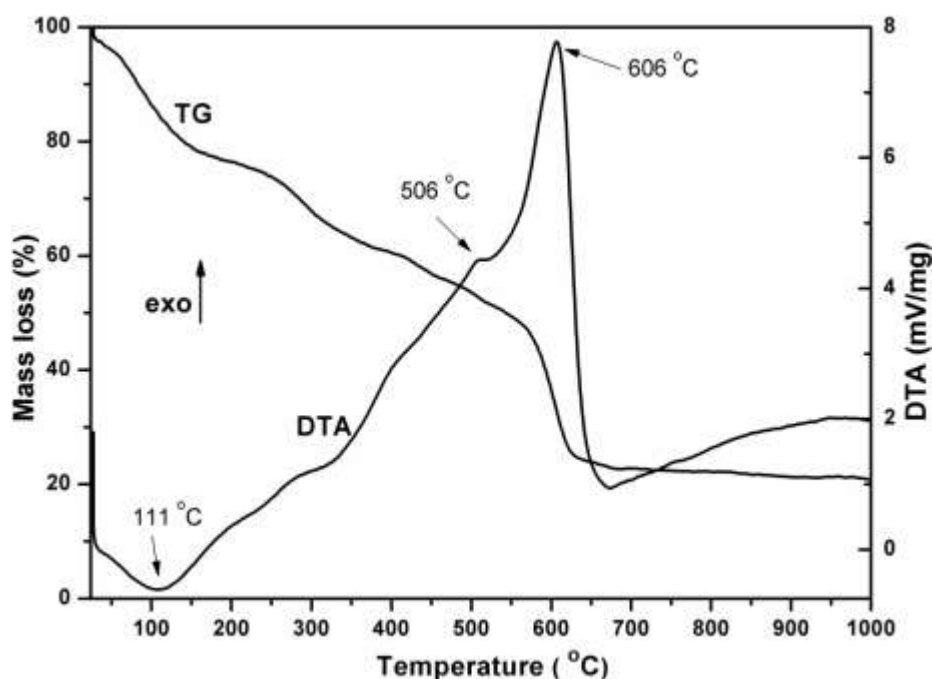


Fig. 4.8 TG-DTA curve of $\text{Ca}_{2.94}\text{Tb}_{0.04}\text{V}_2\text{O}_8$ precursor

The Figs. 4.8 and 4.9 represent the TG-DTA curves of $\text{Ca}_{2.94}\text{Tb}_{0.04}\text{V}_2\text{O}_8$ and $\text{Ca}_{2.92}\text{Tb}_{0.04}\text{Na}_{0.04}\text{V}_2\text{O}_8$ charred precursors respectively. As can be seen from the curves, both the precursors exhibited similar features. A small endothermic hump centred at 111 °C was observed which corresponds to the evaporation of water from the surface of the precursor. This was accompanied by a corresponding gradual mass loss in the TG curve. A small endothermic depression was also observed around 325 °C, this depression was more pronounced in the Na-Tb co-doped sample. This depression could be due to the loss of remaining constitutional water in the precursor.

These endothermic events were followed by the hint of the exothermic event at around 505 °C in both the curves. This indicated the onset of exothermic decomposition. An intense exothermic spike was observed at 606 °C in both the DTA

curves that show the exothermic decomposition of the carbonaceous precursors with the evolution of carbon oxides and nitrogen-containing gases. The exothermic peak descended at around 650 °C. The reflection of this intense exothermic peak was observed in the both TG curves in the form of sharp weight loss. After this an infinitesimal loss in weight was observed up to 1000 °C with no significant events in the DTA curve. Thus, based on the above observations a calcination temperature of 500 °C to remove the residual carbon and the final sintering temperature of 1000 °C were finalised to obtain the final metal oxide composition. The choice of temperature was later confirmed by the pure phase formation of the compositions as deduced from the XRD studies.

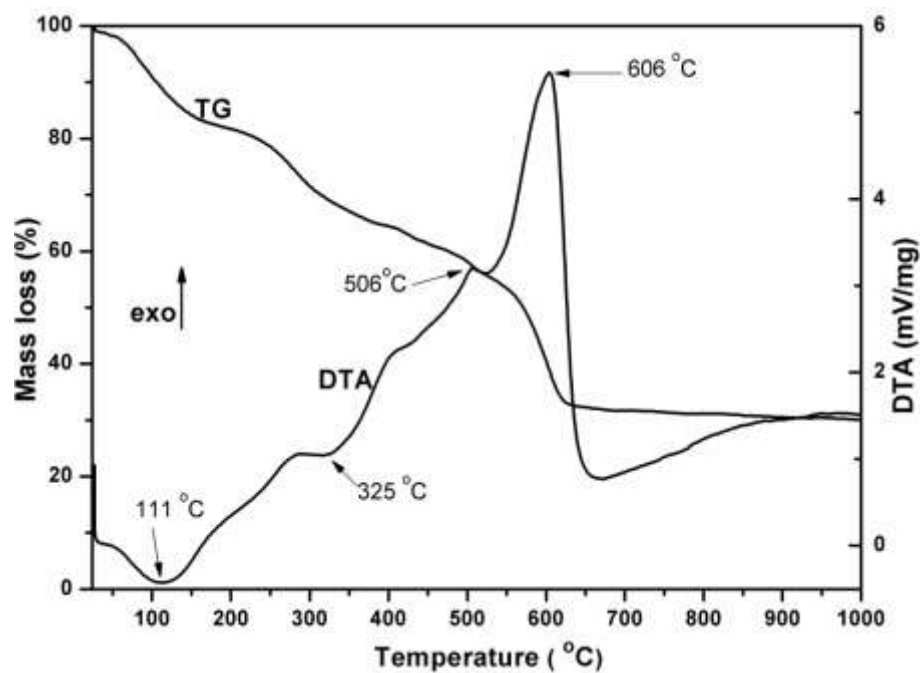


Fig. 4.9 TG-DTA profile of $Ca_{2.92}Tb_{0.04}Na_{0.04}V_2O_8$ precursor

Fig. 4.10 presents the TG-DTA curve for the $Ca_{2.88}Ce_{0.04}Tb_{0.04}V_2O_8$ precursor. As can be observed from the figure, two endothermic depressions were observed in the TG curve at 123 °C and 327 °C respectively, which are attributed to the loss of adsorbed water and constitutional water from the precursor.

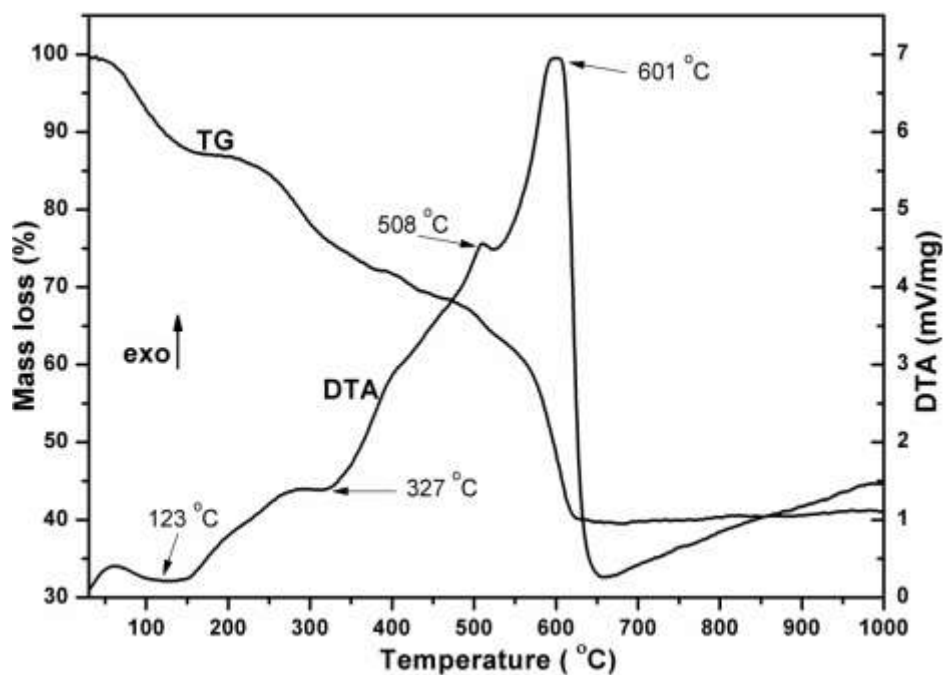


Fig. 4.10 TG-DTA curve of $\text{Ca}_{2.88}\text{Ce}_{0.04}\text{Tb}_{0.04}\text{V}_2\text{O}_8$ precursor

The exothermic decomposition was initiated at 508 °C with the major event taking place at 601 °C. These events were accompanied by the sharp weight loss in the TG curve. After these events, there was no significant activity in both the curves signifying the thermal stability of the formed metal oxide. Similar to Tb and Na-Tb co-doped series, these compounds were also calcined at 500 °C for the carbon removal and then at 1000 °C for the final sintering to get monophasic compositions.

Fig. 4.11 presents TG-DTA profile of $\text{Ca}_{2.39}\text{Pb}_{0.4}\text{Tb}_{0.08}\text{Eu}_{0.06}\text{V}_2\text{O}_8$ precursor. An endothermic depression at 126 °C was attributed to the loss of adsorbed water which corresponded to the weight loss of around 10 % in the TG curve. This was followed by two exothermic twin peaks at 394 °C and 471 °C. These peaks are attributed to the decomposition of carbonaceous precursors. The obtained pattern was different from the previously discussed precursors of Tb single doped, Na-Tb co-doped and Ce-Tb co-doped $\text{Ca}_3\text{V}_2\text{O}_8$ samples. The decomposition in this present case has also taken place at relatively lower temperature.

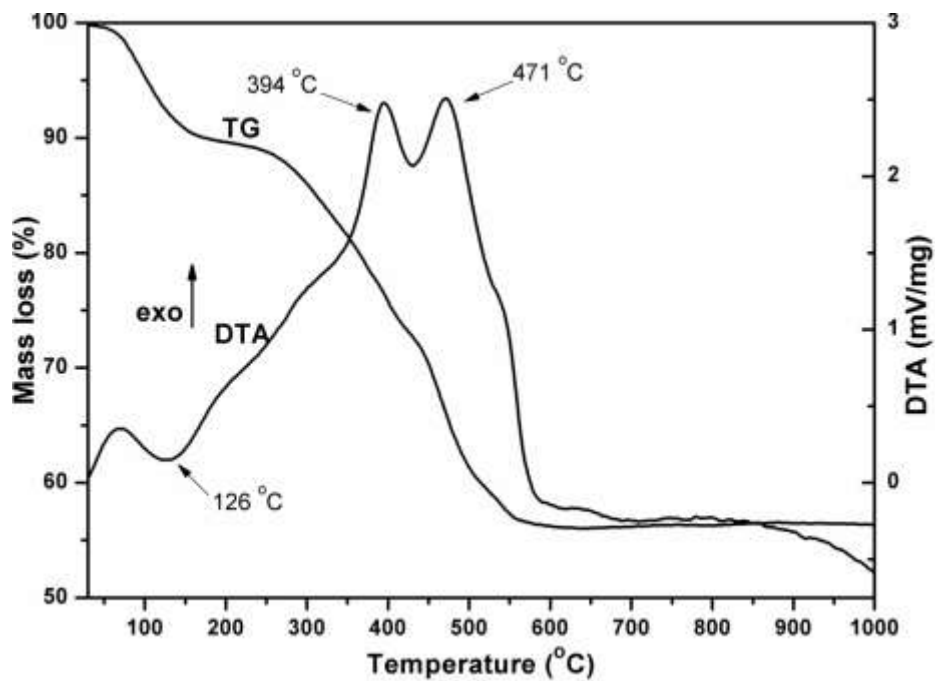


Fig. 4.11 TG–DTA profile of $Ca_{2.39}Pb_{0.4}Tb_{0.08}Eu_{0.06}V_2O_8$ precursor

After 600 °C the TG curve showed no weight loss with an uneventful DTA curve. Although this set of composition showed lower decomposition temperatures they still were calcined at 500 °C and final sintering was done at 1000 °C in the form of pellets.

4.2 X-ray diffraction studies

X-ray diffraction studies were an important part of the characterization process. It helped in elucidating the phase purity of the samples prepared. The ideas regarding the particle nature, like crystallite size, were also deduced from the XRD patterns.

4.2.1 Cu/Bi₂Mo₃O₁₂

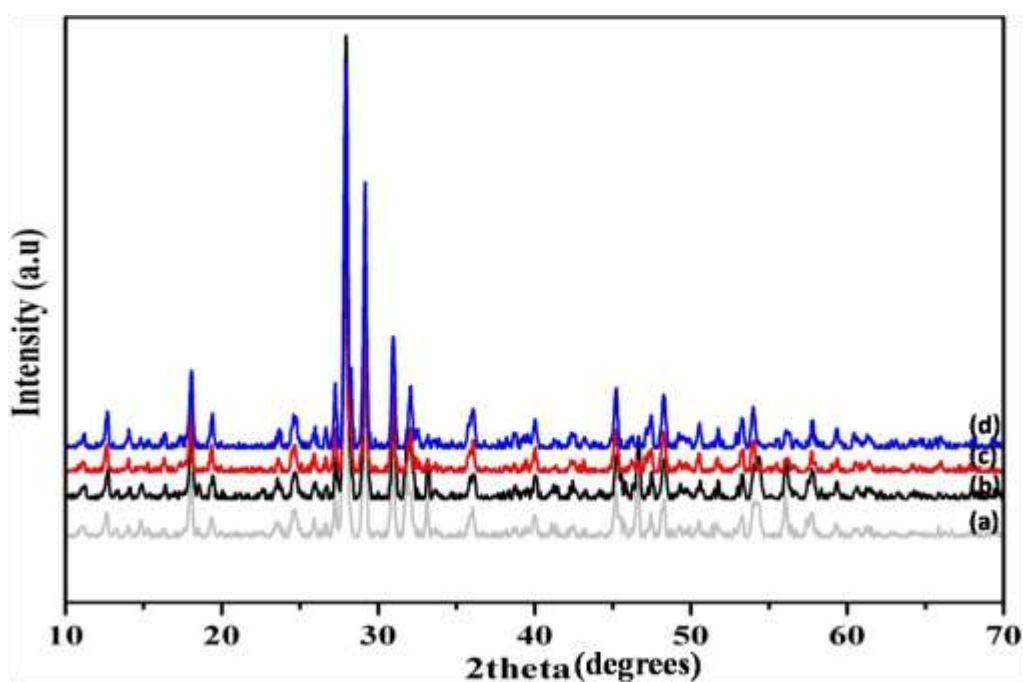


Fig. 4.12 X-ray diffractograms of Cu/Bi₂Mo₃O₁₂ a) Bi₂Mo₃O₁₂ b) 2% Cu/Bi₂Mo₃O₁₂ c) 4% Cu/Bi₂Mo₃O₁₂ d) 8% Cu/Bi₂Mo₃O₁₂

Bi₂Mo₃O₁₂ phase is formed in an orthorhombic crystal lattice. The successful formation of the Bi₂Mo₃O₁₂ was confirmed by comparing the diffractograms with the reported literature [253]. The diffractogram was also compared with the 'd' values given in the JCPDS card No. 21-0103. No extra peaks of Cu or Cu₂O were observed due to the low concentration of Cu in the compositions. The average crystallite size obtained from the Scherrer's formula was in the range of 40-50 nm.

4.2.2 Cu doped $\text{Bi}_4\text{V}_2\text{O}_{11}$ series

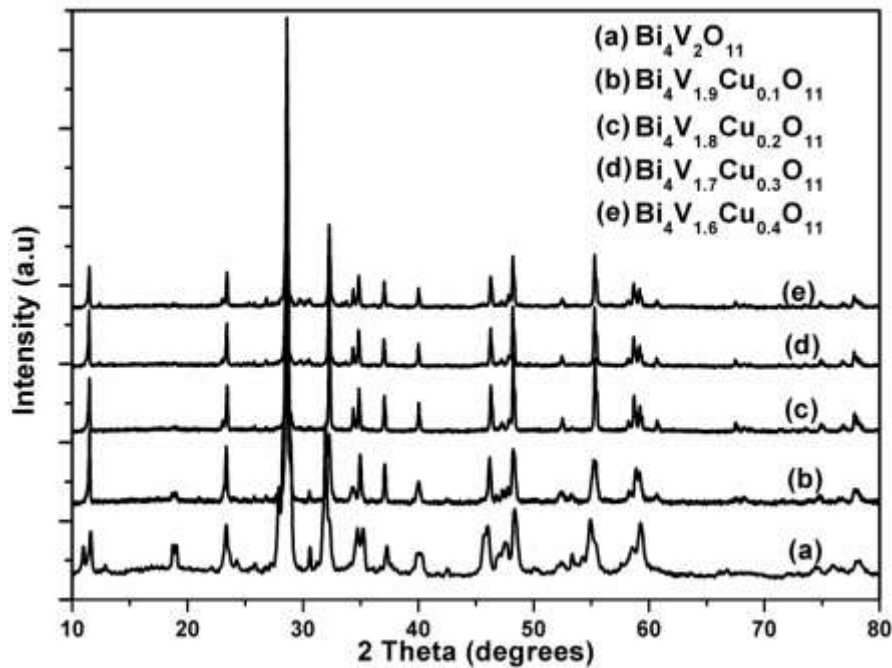


Fig. 4.13 X-ray diffractograms of $\text{Bi}_4\text{V}_{2-x}\text{Cu}_x\text{O}_{11}$ series

Fig. 4.13 displays the diffractograms of Cu doped $\text{Bi}_4\text{V}_2\text{O}_{11}$ compositions. $\text{Bi}_4\text{V}_2\text{O}_{11}$ is known to adopt three phases α , β and γ . Out of these three phases, γ is a high-temperature phase with high ionic conductivity [185]. α phase is characterized by a doublet in the region between 2 thetas 45.5° and 46.5° , whereas the β phase is characterised by the merging of this doublet in the singlet [156, 254]. The γ phase is characterized by a singlet in the region between 2 thetas 45.5° and 46.5° . Also, a doublet at 2 theta $\sim 32^\circ$ in case of α and β converges to a singlet in the case of γ phase. The high-temperature γ phase is basically a centrosymmetric tetragonal phase derived from the low temperature non-centrosymmetric orthorhombic (α) phase through a mid temperature centrosymmetric orthorhombic phase (β) [255]. The structural symmetry of $\text{Bi}_4\text{V}_2\text{O}_{11}$ increases with the increase in temperature, hence the merging of above-discussed diffraction peaks occur. As observed from the plots, in case of the pristine compositions the peaks at 46° and 32° showed very minute bifurcations indicating the presence of small amount of α or β phase. But after the doping of Cu ions, these

bifurcations were clearly not seen. Based on these observations we can say that we have been successful in stabilizing the high temperature γ phase at room temperature although with very low impurity level in case of pristine composition. It was also observed that the diffraction peaks were narrowed with the Cu doping indicating the increase in the crystallite size which is also confirmed by the crystallite sizes obtained from the diffractograms tabulated in Table 4.1.

Table 4.1 Crystallite size of $\text{Bi}_4\text{V}_{2-x}\text{Cu}_x\text{O}_{11}$

Composition	Crystallite Size (nm)
$\text{Bi}_4\text{V}_2\text{O}_{11}$	35
$\text{Bi}_4\text{V}_{1.9}\text{Cu}_{0.1}\text{V}_2\text{O}_{11}$	45
$\text{Bi}_4\text{V}_{1.8}\text{Cu}_{0.2}\text{O}_{11}$	48
$\text{Bi}_4\text{V}_{1.7}\text{Cu}_{0.3}\text{V}_2\text{O}_{11}$	49
$\text{Bi}_4\text{V}_{1.6}\text{Cu}_{0.4}\text{V}_2\text{O}_{11}$	49

4.2.3 $\text{Cu}_x\text{V}_{1-x}\text{SbO}_4$ system

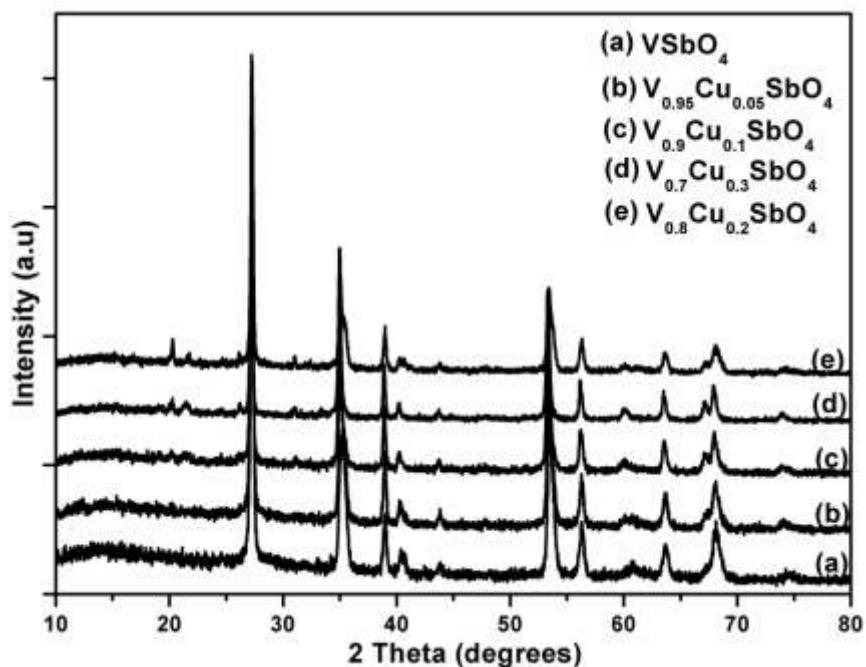


Fig. 4.14 X-ray diffractograms of $\text{Cu}_x\text{V}_{1-x}\text{SbO}_{4-\delta}$ series

Fig 4.14 displays the diffractograms of Cu doped VSbO₄ compositions. A single phase was obtained for first three compositions and matched well with the JCPDS card 16-0600, whereas, small impurities can be seen for the compositions with the highest compositions. These impurities are attributed to the CuO and some miscellaneous phases. The crystallite sizes calculated from the diffractograms are tabulated in table 4.2.

Table 4.2 Crystallite size of V_{1-x}Cu_xSbO₄

Composition	Crystallite Size (nm)
VSbO ₄	38
V _{0.95} Cu _{0.05} SbO ₄	37
V _{0.9} Cu _{0.1} SbO ₄	34
V _{0.8} Cu _{0.2} SbO ₄	36
V _{0.7} Cu _{0.3} SbO ₄	38

4.2.4 Cu_xK_yV_{1-x}Sb_{1-y}O₄ system

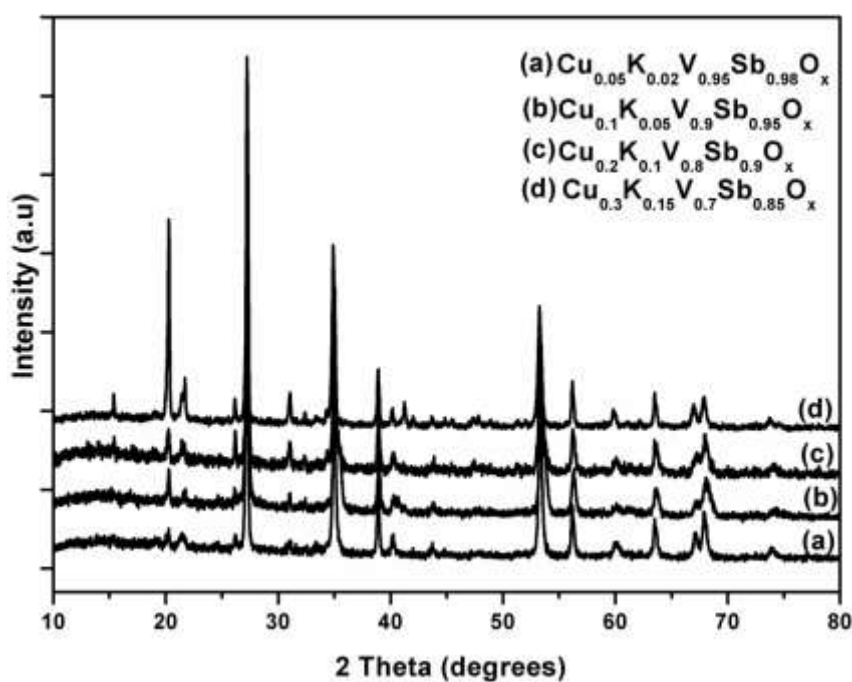


Fig. 4.15 X-ray diffractograms of Cu_xK_yV_{1-x}Sb_{1-y}O series

The XRD plots of $\text{Cu}_x\text{K}_y\text{V}_{1-x}\text{Sb}_{1-y}\text{O}_{4-\delta}$ are presented in the Fig. 4.15. These catalysts were prepared as the composite catalysts. The ionic size of K is very large as compared to the ionic sizes of V or Sb so it cannot be substituted for either of the ions. Therefore, single phase formations of the compositions were not observed. As observed from the diffractogram above the composition showed a mixture of many phases. But the main parent phase observed is VSbO_4 . The other phases are miscellaneous phases which might have various compositions depending upon the combination of metal elements present in the composite.

4.2.5 $\text{Bi}_2\text{Mo}_{1-x}\text{W}_x\text{O}_6$ system

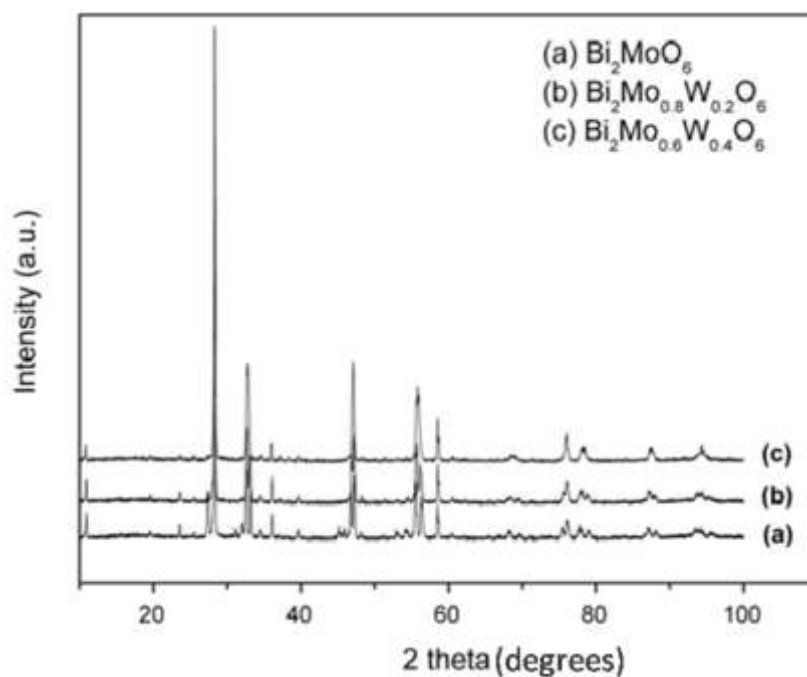


Fig. 4.16 X-ray diffractograms of $\text{Bi}_2\text{Mo}_{1-x}\text{W}_x\text{O}_6$ series

Table 4.3 Crystallite size of $\text{Bi}_2\text{Mo}_{1-x}\text{W}_x\text{O}_6$

Composition	Crystallite Size (nm)
Bi_2MoO_6	32
$\text{Bi}_2\text{Mo}_{1.8}\text{W}_{0.2}\text{O}_6$	35
$\text{Bi}_2\text{Mo}_{1.6}\text{W}_{0.4}\text{O}_6$	34

X-Ray diffractograms of $\text{Bi}_2\text{Mo}_{1-x}\text{W}_x\text{O}_6$ ($x = 0.0, 0.2$ and 0.4) compounds are shown in the Fig. 4.16. The observed d-spacings and peak intensities of the pristine and W doped compounds matched well with the JCPDS data (Card No. 21-0102). The crystallite sizes obtained from the XRD patterns are tabulated in Table 4.3. The crystallite sizes obtained were in the range of 32 -35 nm.

4.2.6 $\text{M}_3\text{V}_2\text{O}_8$ (M = Ca, Sr, and Ba)

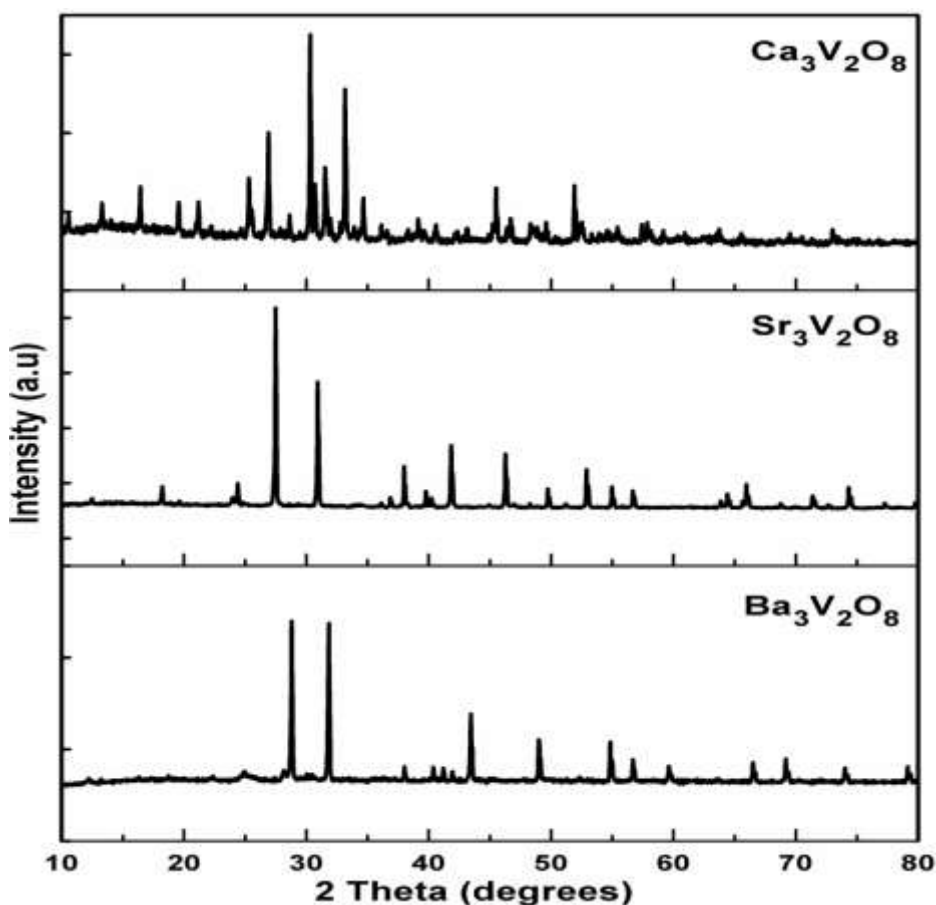


Fig. 4.17 X-ray diffractograms of $\text{M}_3\text{V}_2\text{O}_8$

Fig. 4.17 shows the XRD patterns of alkaline earth metal vanadates prepared at 750°C . The obtained spectra matched well with the JCPDS cards. $\text{Ca}_3\text{V}_2\text{O}_8$ and $\text{Sr}_3\text{V}_2\text{O}_8$ patterns were matched with the JCPDS cards 46-756 and 84-1844 respectively, whereas the $\text{Ba}_3\text{V}_2\text{O}_8$ powder pattern was compared with the card 71-2060. The crystallite sizes as obtained from the diffractograms were 40 nm, 38 nm and 37 nm for the $\text{Ca}_3\text{V}_2\text{O}_8$, $\text{Sr}_3\text{V}_2\text{O}_8$ and $\text{Ba}_3\text{V}_2\text{O}_8$ respectively.

4.2.7 RE-doped $\text{Ca}_3\text{V}_2\text{O}_8$ compositions.

Figs. 4.18 and 4.19 display the X-ray diffraction patterns of $\text{Ca}_{3-3x/2}\text{Tb}_x\text{V}_2\text{O}_8$, $\text{Ca}_{3-2x}\text{Tb}_x\text{Na}_x\text{V}_2\text{O}_8$ series respectively.

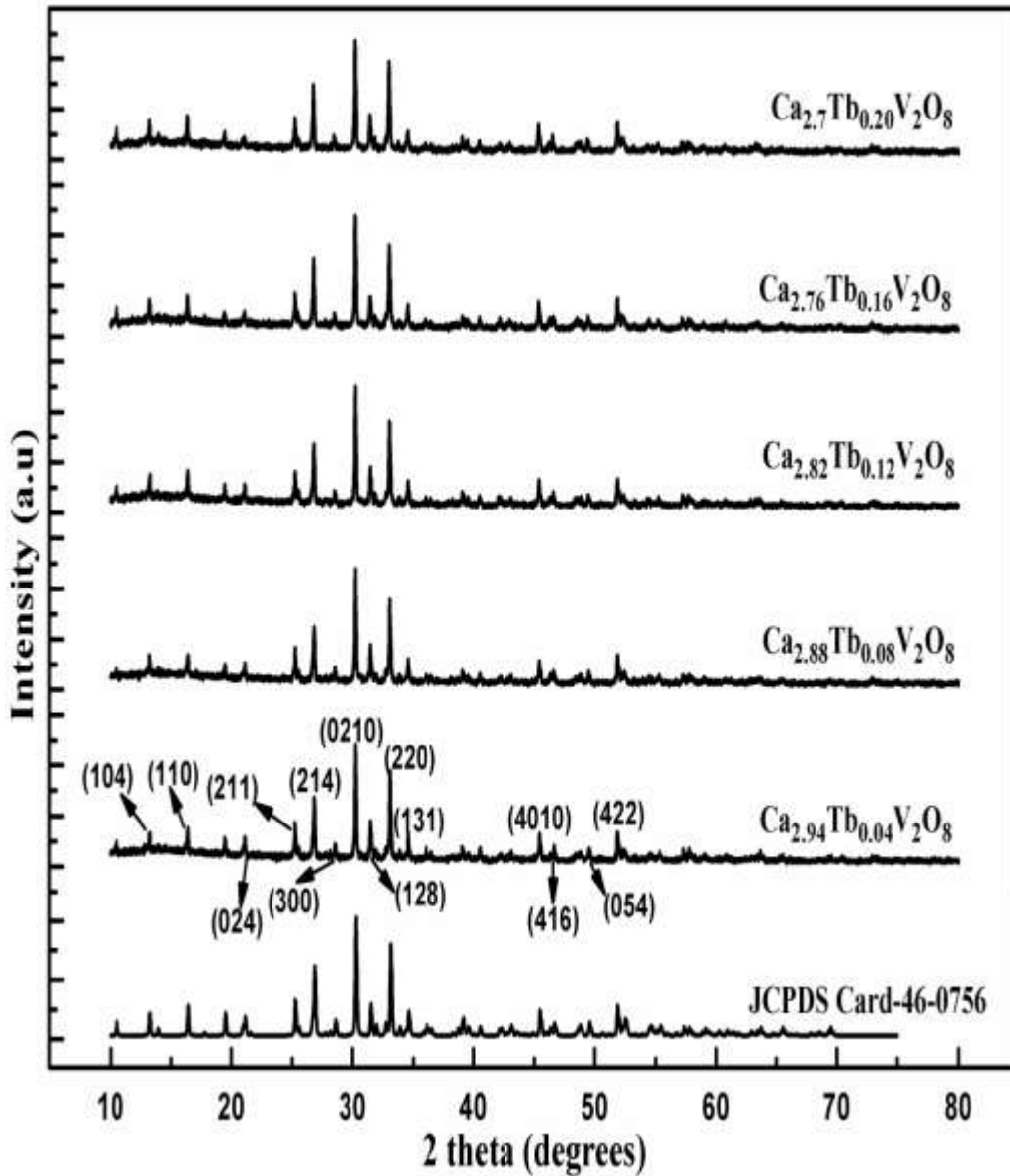


Fig. 4.18 XRD plots of $\text{Ca}_{3-3x/2}\text{Tb}_x\text{V}_2\text{O}_8$ series

The crystal structure of $\text{Ca}_3\text{V}_2\text{O}_8$ relates to the Rhombohedral crystal system having space group $R3c$ wherein Ca^{2+} has non-inversion symmetry. As evident from the plots the XRD patterns of both the prepared series matched well with the JCPDS card 46-0756.

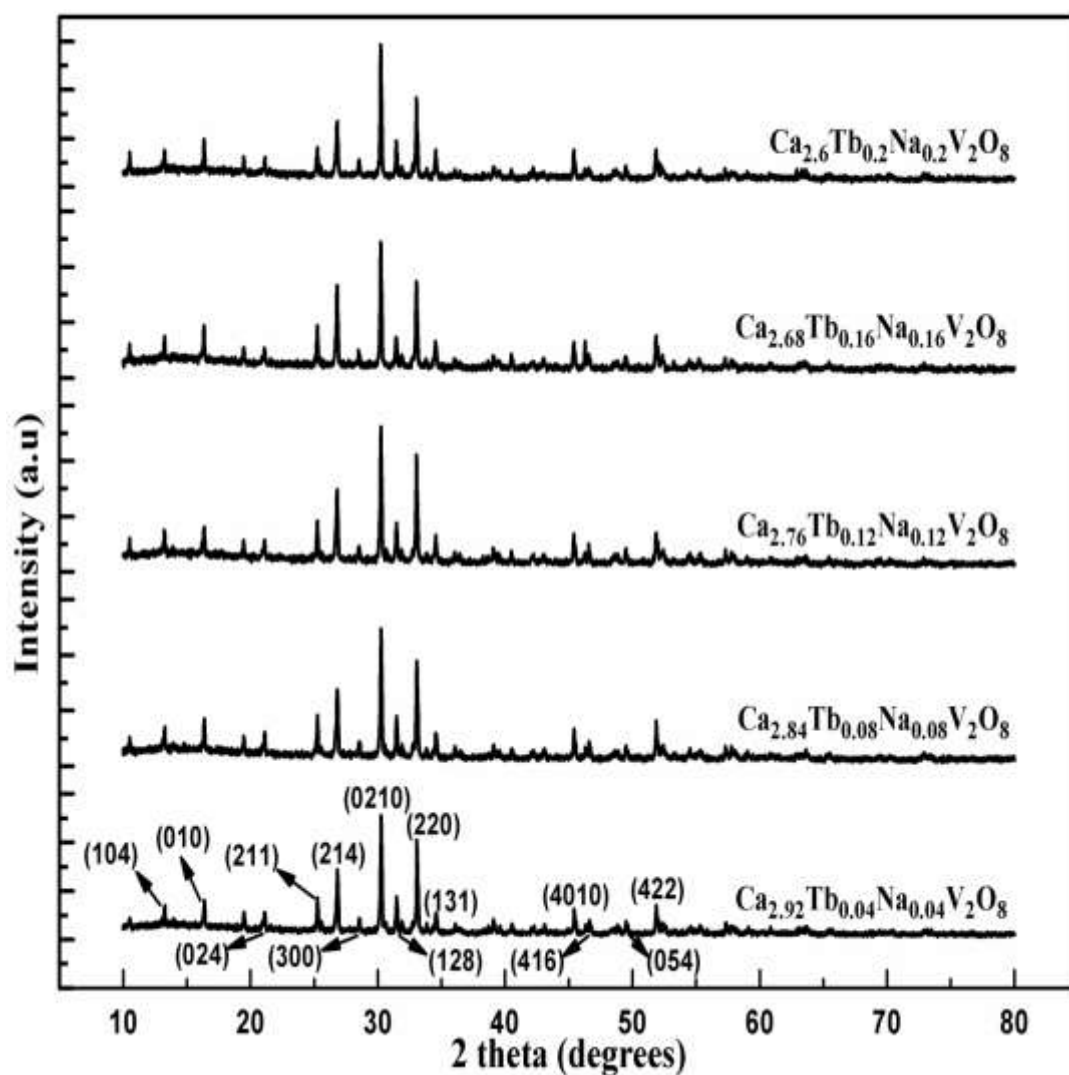


Fig. 4.19 XRD plots of $Ca_{3-2x}Tb_xNa_xV_2O_8$ series

In Tb singly doped series, three Ca^{2+} ions are substituted by two Tb^{3+} ions giving rise to the cation vacancies in the structure, the number of vacancies was obvious to increase as the doping concentration of Tb increased but this has not led to the collapse of the crystal structure as evident from the sharp and crystalline powder patterns, similarly in Na-Tb co-doped series no segregation of Na containing phases was seen confirming the success of preparative procedure. Moreover, no significant change in d-spacings were observed which has led us to propose minuscule change in the lattice dimensions which could also be expected due to fairly comparable sizes ($Ca^{2+} = 100$ pm, $Tb^{3+} = 92.3$ pm, $Na^{+} = 102$ pm) of all three metal ion components. The

x-ray diffractograms obtained in case of the both the above compositions matched well with the JCPDS card no. 46-0756.

Figs 4.20 and 4.21 display the X-ray diffractograms of $\text{Ca}_{2.94-3x/2}\text{Ce}_{0.04}\text{Tb}_x\text{V}_2\text{O}_8$ and $\text{Ca}_{2.48-3x/2}\text{Pb}_{0.4}\text{Tb}_{0.08}\text{Eu}_x\text{V}_2\text{O}_8$ respectively. As observed from the figures below, the diffractograms of both the series matched well with the JCPDS card No. 46-0756.

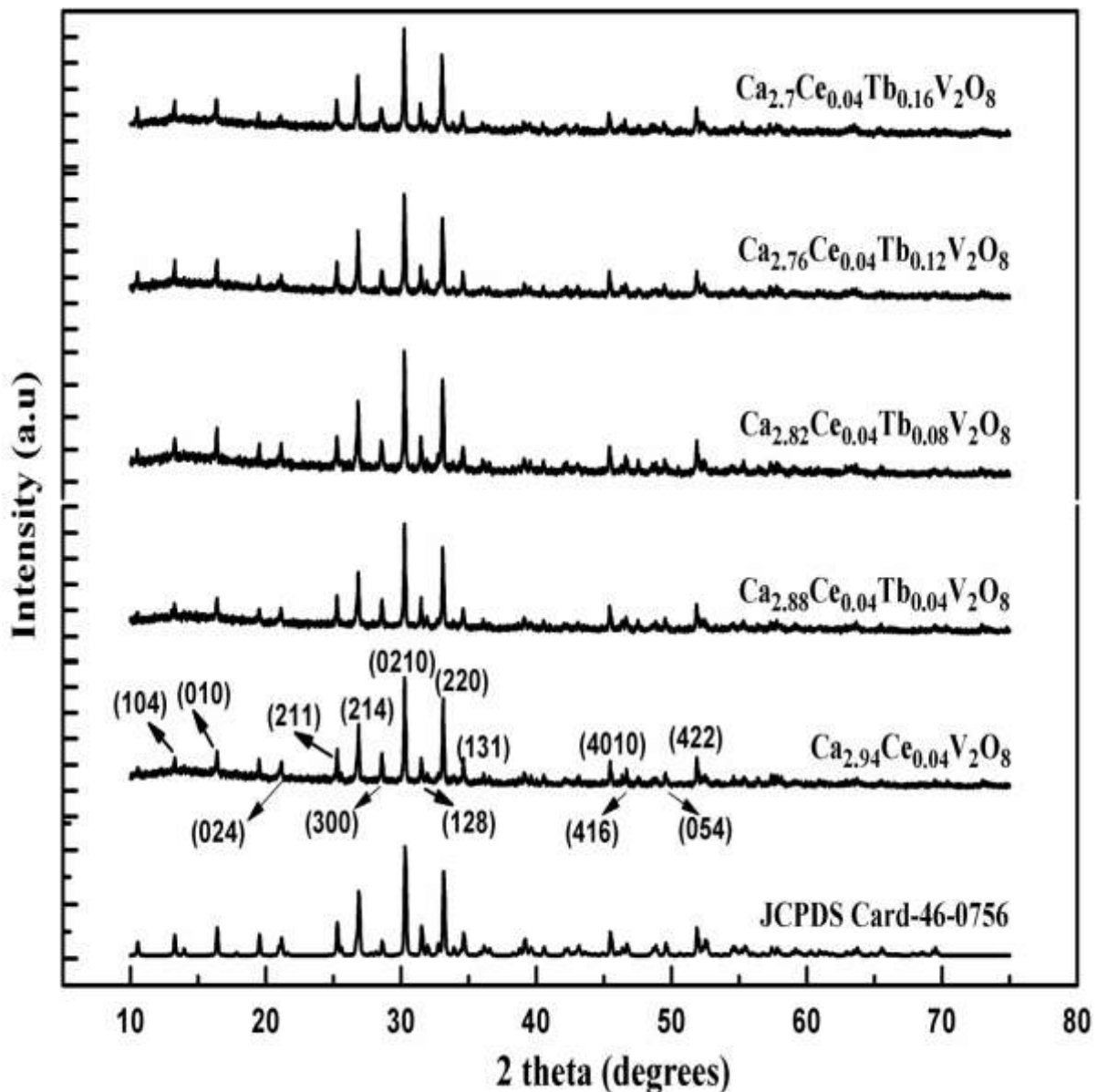


Fig. 4.20 XRD plots of $\text{Ca}_{2.94-3x/2}\text{Ce}_{0.04}\text{Tb}_x\text{V}_2\text{O}_8$ series

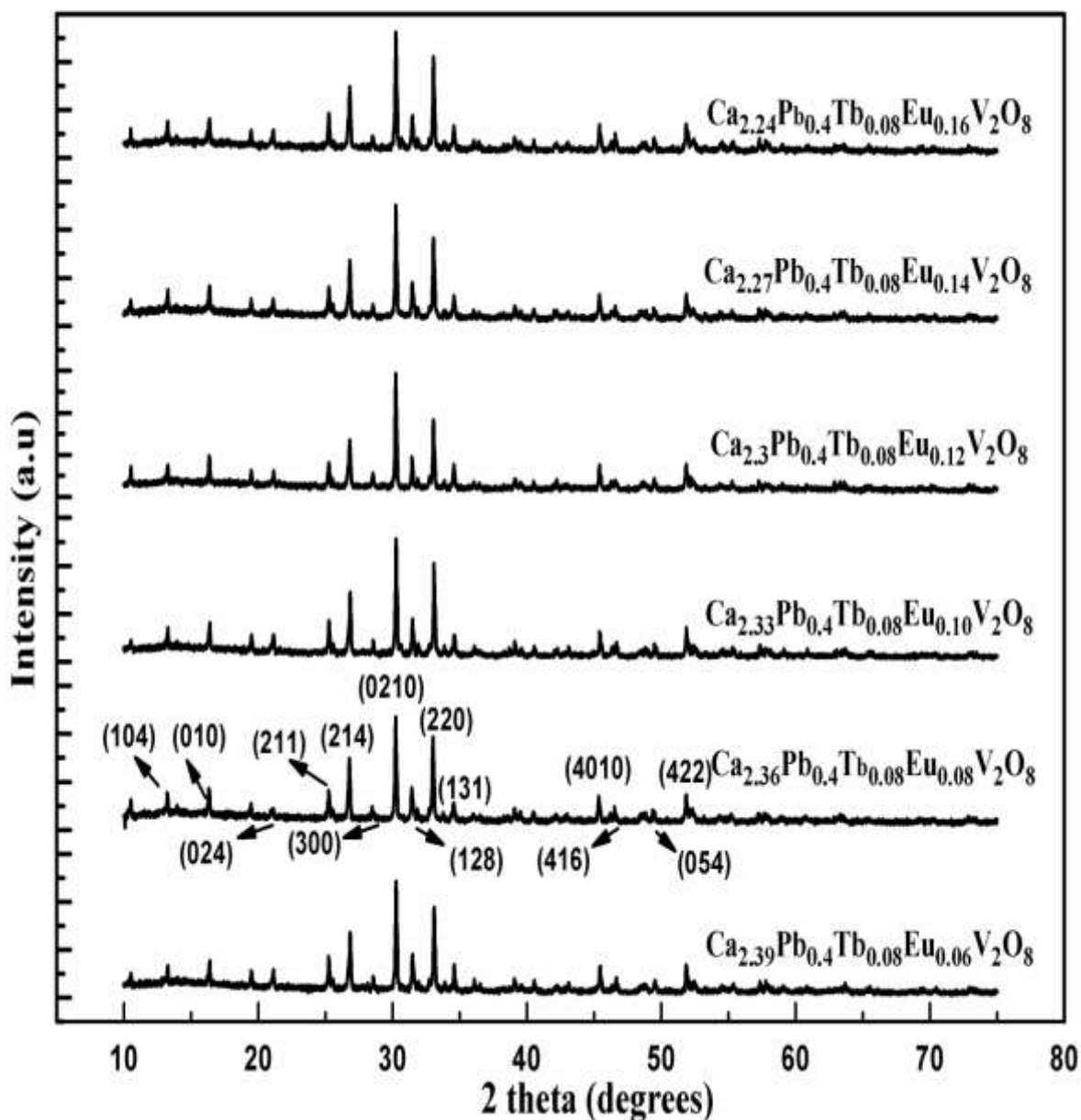


Fig. 4.21 XRD plots of $Ca_{2.48-3x/2}Pb_{0.4}Tb_{0.08}Eu_xV_2O_8$ series

In case of the Ce and Tb co-doped series, there was no occurrence of any impurities. As ionic sizes of Ce and Tb are comparable with the ionic size of Ca, therefore it seems that both the dopant ions have been incorporated in the crystal lattice.

Similarly, in case of the $Ca_{2.48-3x/2}Pb_{0.4}Tb_{0.08}Eu_xV_2O_8$ series, the Pb doping has not ruptured the host structure as can be observed from the perfectly matching diffractograms.

4.3 Infrared spectroscopic studies

Metal oxide compounds show characteristic bands in IR region related to the M-O linkages. Especially, in the case of molybdates and vanadates, the M-O bands are well defined. IR spectra, therefore, gave a very good qualitative estimate of the metal oxide structures.

4.3.1 Cu/Bi₂Mo₃O₁₂

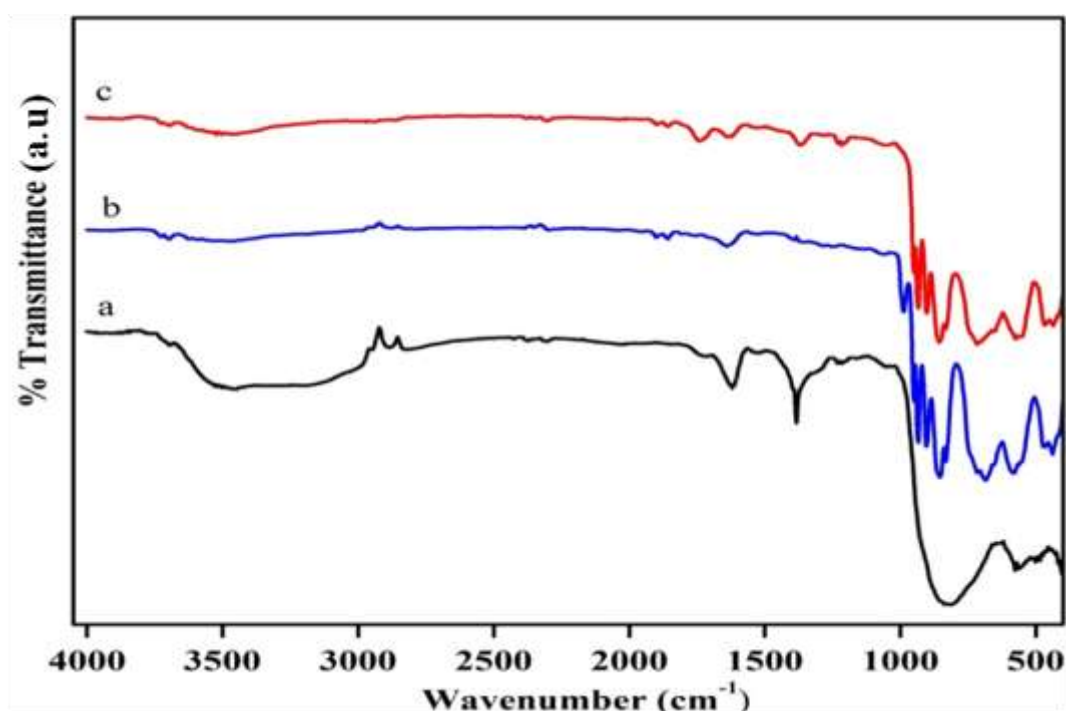


Fig. 4.22 Infrared spectra of a) Bi₂Mo₃O₁₂ b) α -Bi₂Mo₃O₁₂ c) 8% Cu/ Bi₂Mo₃O₁₂

Fig. 4.22 presents the infrared spectrum of Bi₂Mo₃O₁₂ precursor and its oxide. The plot 'a' presents the infrared spectrum of the co-precipitated precursor. A broad band was observed from 600 cm⁻¹ to 1000 cm⁻¹. This broad band was associated with the stretching vibrations of MoO₄ tetrahedra. The broad band has resulted from the overlap of different stretching modes of the tetrahedron. This lack of demarcation between the stretching modes indicates the amorphous nature of the co-precipitated product. The peak noticed at 1350 cm⁻¹ is attributed to the N-O stretchings. The source

of this residual $(\text{NO}_3)^{-1}$ moiety is $\text{Bi}(\text{NO}_3)_3$ or HNO_3 which were used as the source and solvent for the Bi^{3+} solution respectively. The broad and shallow band spanning the range from 3200 to 3600 cm^{-1} is associated with the stretching vibrations of H_2O molecule. The peak observed at 1630 cm^{-1} is associated with bending mode of water. Plot 'b' represents the spectrum of $\text{Bi}_2\text{Mo}_3\text{O}_{12}$ oxide, obtained after the calcination of the precursor at 450 °C for four hours. The IR bands in this spectrum were resolved indicative of well-formed and crystalline met oxide, the bands from 600 to 100 cm^{-1} are attributed to the MoO_4 tetrahedra. The bands that are observed below 600 cm^{-1} are attributable to the Bi-O stretchings [90, 256, 257]. The IR spectrum is well in accordance with the earlier literature reports. The plot 'b' represents the copper supported $\text{Bi}_2\text{Mo}_3\text{O}_{12}$ composition. The Cu-O stretching are observed below 500 cm^{-1} could not be seen and rightly so, as they were expected to merge in the more pronounced Bi-O stretching.

4.3.2 $\text{Bi}_4\text{V}_{2-x}\text{Cu}_x\text{O}_{11}$ system

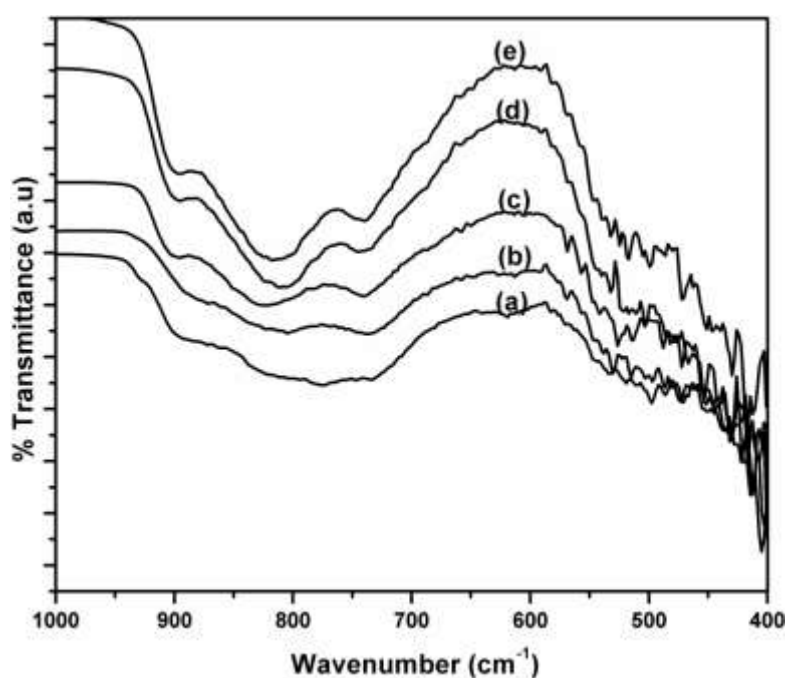


Fig. 4.23 Infrared spectra of $\text{Bi}_4\text{V}_{2-x}\text{Cu}_x\text{O}_{11}$ a) $\text{Bi}_4\text{V}_2\text{O}_{11}$ b) $\text{Bi}_4\text{V}_{1.9}\text{Cu}_{0.1}\text{O}_{11}$ c) $\text{Bi}_4\text{V}_{1.8}\text{Cu}_{0.2}\text{O}_{11}$ d) $\text{Bi}_4\text{V}_{1.7}\text{Cu}_{0.3}\text{O}_{11}$ e) $\text{Bi}_4\text{V}_{1.6}\text{Cu}_{0.4}\text{O}_{11}$

Fig. 4.23 displays the infrared spectra of pristine and Cu doped $\text{Bi}_4\text{V}_2\text{O}_{11}$ series. The $\text{Bi}_4\text{V}_2\text{O}_{11}$ structure is made up of the $(\text{VO}_4)^{3-}$ tetrahedron hence the spectrum is reflective of the standard stretching modes of a regular tetrahedron. The bands in the region below 500 cm^{-1} are attributed to the Bi-O stretching vibrations of $[\text{BiO}_6]$ octahedra [258, 259]. A broad band in the region from $650 - 900\text{ cm}^{-1}$ is attributed to symmetric and asymmetric vibrations of V-O bonds. The initial part of the band around 650 cm^{-1} is attributed to asymmetric vibrations of O-V-O bonds. The signal around 740 cm^{-1} is related to symmetric V-O stretching. The obtained spectra matched well with the earlier reports in the literature. The signal spanning from $800-900\text{ cm}^{-1}$ can be associated with the V-O asymmetric stretching. The obtained spectra matched well with the reports in the literature [185, 260]

4.3.3 $\text{Bi}_2\text{Mo}_{1-x}\text{W}_x\text{O}_6$

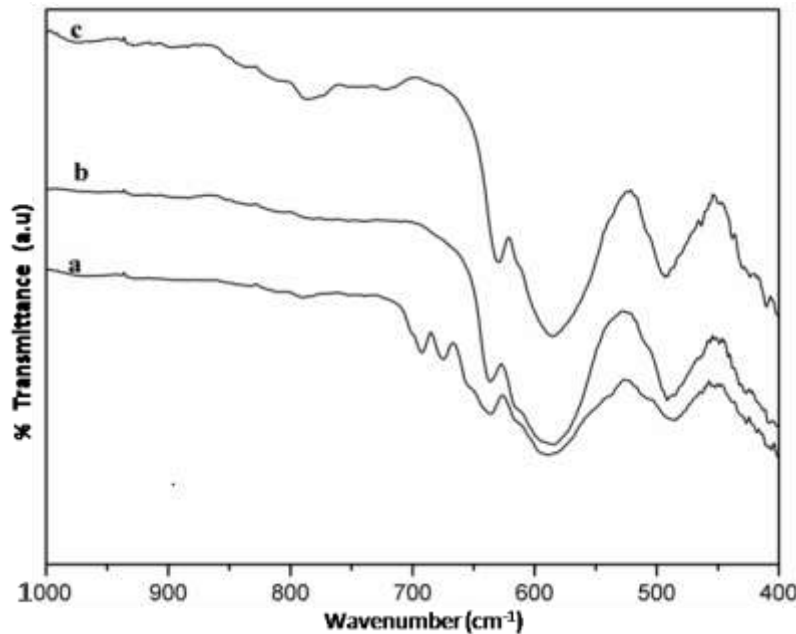


Fig. 4.24 Infrared spectra of $\text{Bi}_2\text{Mo}_{1-x}\text{W}_x\text{O}_6$ series.
a) Bi_2MoO_6 b) $\text{Bi}_2\text{Mo}_{0.8}\text{W}_{0.2}\text{O}_6$, c) $\text{Bi}_2\text{Mo}_{0.6}\text{W}_{0.4}\text{O}_6$

IR spectra displayed in Fig. 4.24 show broad bands in the region $400-900\text{ cm}^{-1}$ which can be attributed to the stretching vibrations of Bi-O and M-O (M= Mo or W)

from $[\text{BiO}_6]$ and MO_4 moieties. The peak appearing at around 490 cm^{-1} is related to the Bi-O octahedral stretching vibrations. The signal from around 600 to 800 cm^{-1} represents the M-O stretching vibrations. The obtained spectra were in accordance with the reports in the literature.

4.3.4 $\text{M}_3\text{V}_2\text{O}_8$ (M = Ca, Sr, and Ba)

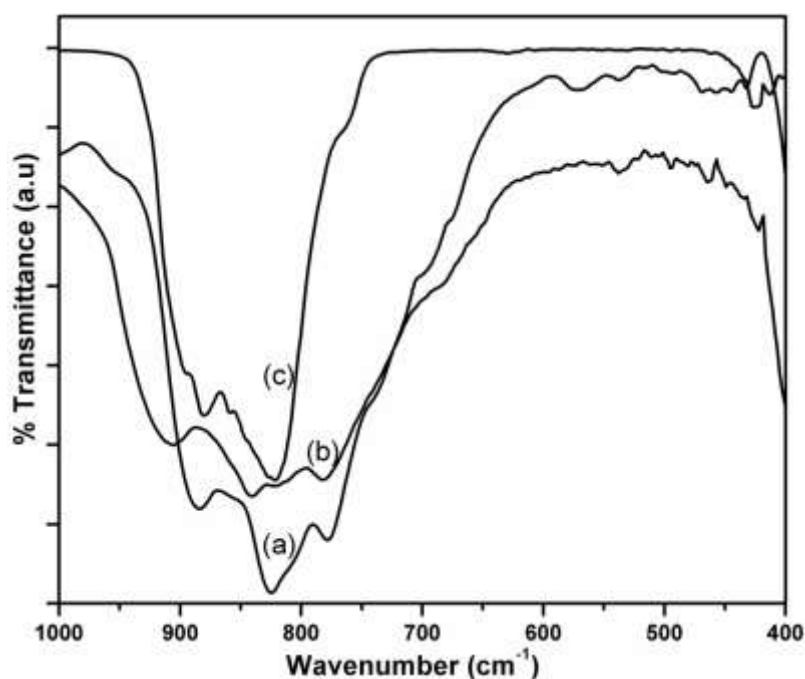


Fig. 4.25 Infrared spectra of $\text{M}_3\text{V}_2\text{O}_8$ series. (M = Ca, Sr and Ba)

a) $\text{Ca}_3\text{V}_2\text{O}_8$ b) $\text{Sr}_3\text{V}_2\text{O}_8$ and b) $\text{Ba}_3\text{V}_2\text{O}_8$

Fig. 4.25 display the Infrared spectra of prepared alkaline earth metal vanadates. The basic unit in the orthovanadates is VO_4^{3-} units. The Plot 'a' represents the IR spectrum of $\text{Ca}_3\text{V}_2\text{O}_8$. The strong signals obtained from 750 - 900 cm^{-1} are assigned to V-O stretching vibration [261]. IR spectra of $\text{Sr}_3\text{V}_2\text{O}_8$ (plot 'b') and $\text{Ba}_3\text{V}_2\text{O}_8$ (plot 'c'), similar signals were observed associated with V-O stretching. From the spectra it can be also observed that the $\text{Ba}_3\text{V}_2\text{O}_8$ signals were narrower than the rest of the two. Although the signals from all the three vanadates were derived from the same structural moiety but the signals were centred at different wavenumber. These

slight differences in the stretching vibrations of alkaline earth metal vanadates can be expected due to different size of counter cations and also due to variations in the crystal structures they adopt.

4.3.5 RE doped $\text{Ca}_3\text{V}_2\text{O}_8$ compositions

The infrared spectra of $\text{Ca}_{3-3x/2}\text{Tb}_x\text{V}_2\text{O}_8$, $\text{Ca}_{3-2x}\text{Tb}_x\text{Na}_x\text{V}_2\text{O}_8$, $\text{Ca}_{2.94-3x/2}\text{Ce}_{0.04}\text{Tb}_x\text{V}_2\text{O}_8$ and $\text{Ca}_{2.48-3x/2}\text{Pb}_{0.4}\text{Tb}_{0.08}\text{Eu}_x\text{V}_2\text{O}_8$ series are presented in the Figs 4.26, 4.27, 4.28 and 4.29 respectively.

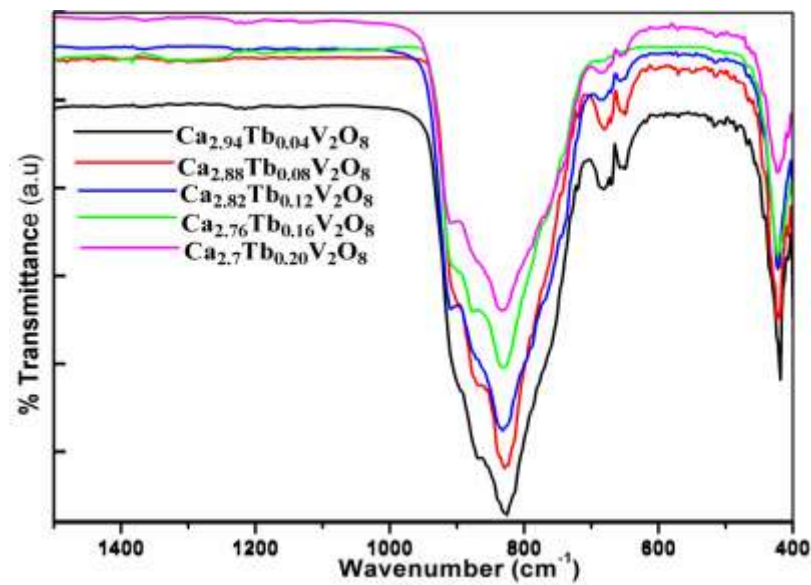


Fig. 4.26 Infrared spectra of $\text{Ca}_{3-3x/2}\text{Tb}_x\text{V}_2\text{O}_8$ series

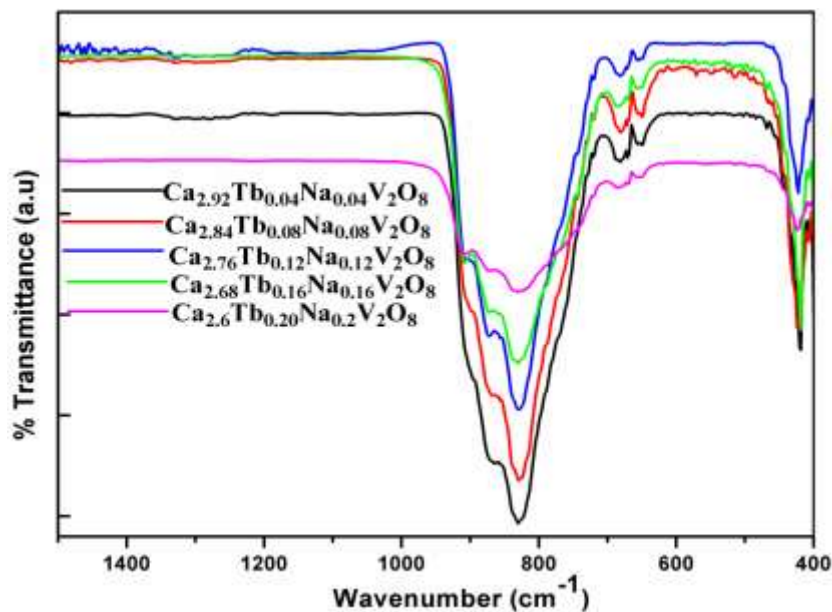


Fig. 4.27 Infrared spectra of $\text{Ca}_{3-2x}\text{Tb}_x\text{Na}_x\text{V}_2\text{O}_8$ series

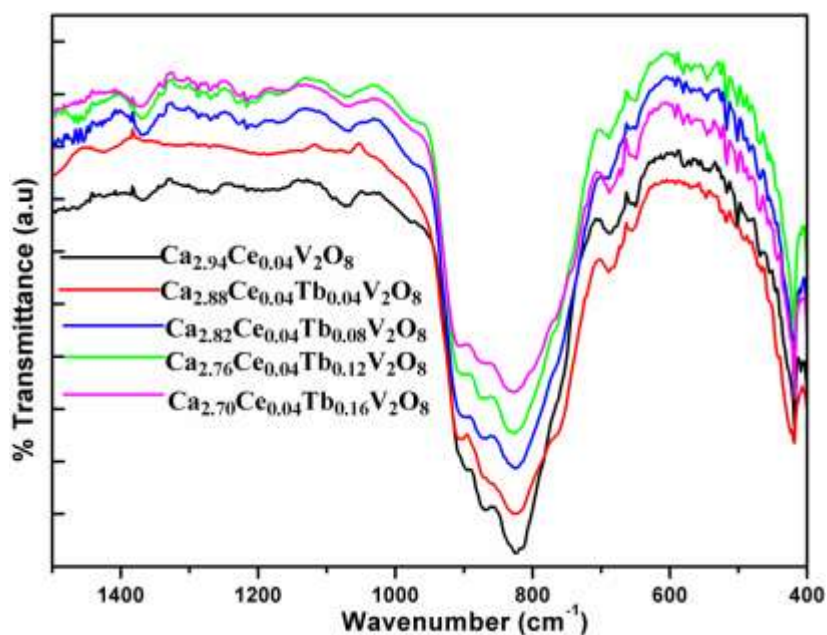


Fig. 4.28 Infrared spectra of $\text{Ca}_{2.94-3x/2}\text{Ce}_{0.04}\text{Tb}_x\text{V}_2\text{O}_8$ series

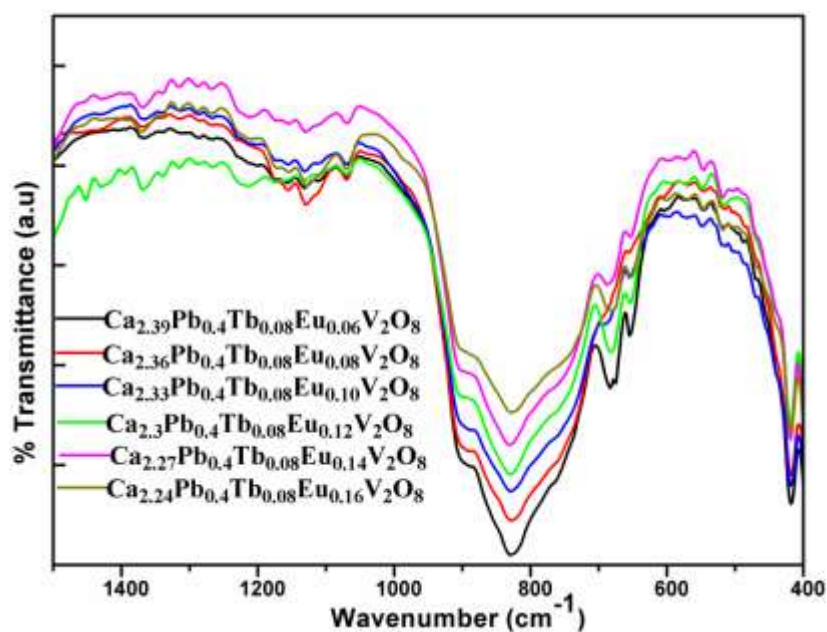


Fig. 4.29 Infrared spectra of $\text{Ca}_{2.48-3x/2}\text{Pb}_{0.4}\text{Tb}_{0.08}\text{Eu}_x\text{V}_2\text{O}_8$ series

The characteristic symmetric and asymmetric stretching bands of V-O were seen clearly in the region 600- 900 cm^{-1} . The peak observed at around 420 cm^{-1} in all the compositions was attributed to the Ca-O vibrations. The spectra obtained in case of all the four compositions were in line with the spectrum of pristine $\text{Ca}_3\text{V}_2\text{O}_8$ presented in

the earlier section (4.3.4). Slight shifts in the signals were observed as expected from the different cationic substitutions.

4.4 Raman spectroscopic studies

Raman spectroscopy is a very sensitive tool to evaluate the phase purity. It also gave reliable information regarding the local structure of prepared phosphors.

4.4.1 Raman spectra of Tb doped $\text{Ca}_3\text{V}_2\text{O}_8$

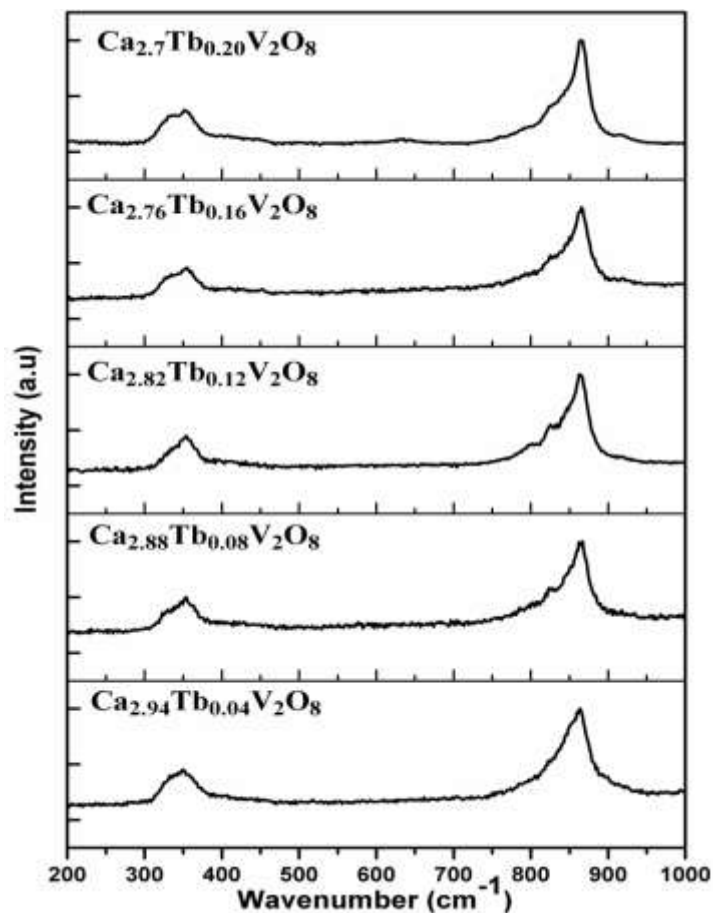


Fig. 4.30 Raman spectra of $\text{Ca}_{3-3x/2}\text{Tb}_x\text{V}_2\text{O}_8$ series

The Raman spectra of Tb and Na-Tb co-doped samples are presented in the Fig. 4.30 and 4.31 respectively. The vanadate moiety is present in the form of VO_4^{3-} . The internal modes of the tetrahedral VO_4^{3-} can be given as follows, ν_1 mode which relates to the stretching mode of A_1 symmetry, ν_2 is a bending mode that relates to the bending

mode associated with E symmetry. ν_3 is an anti-symmetric stretching mode that is associated with F_2 symmetry and finally the ν_4 bending mode of F_2 symmetry.

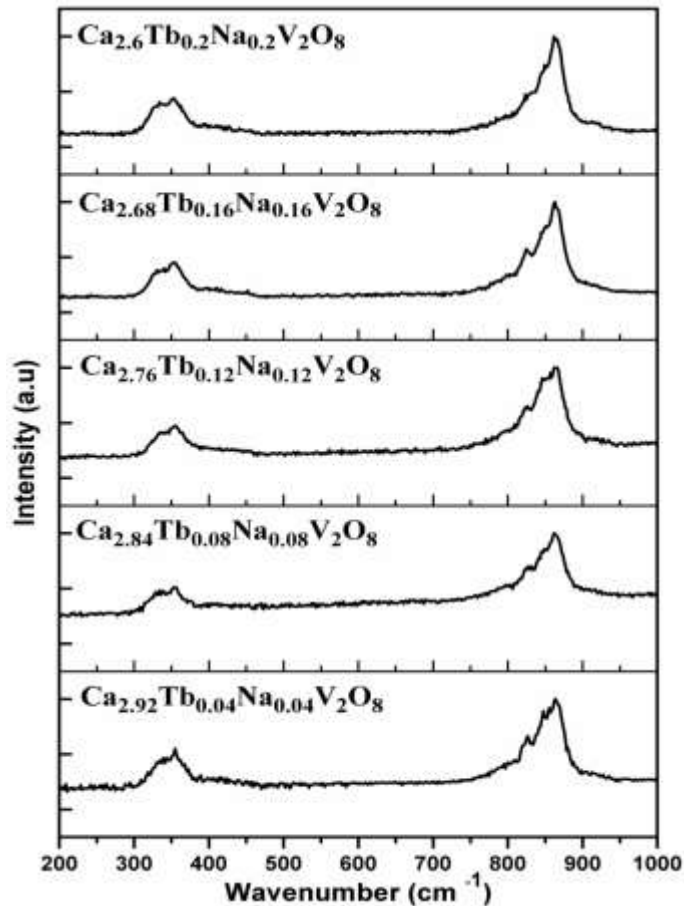


Fig. 4.31 Raman spectra of $Ca_{3-2x}Tb_xNa_xV_2O_8$ series

The obtained Raman spectra matched well with the reports in the literature by Grzechnik and Ivanowskii [262, 263]. It is reported in the literature that by the virtue of crystal lattice. There exists disorderliness due to the interactions of different oxygen with the different coordinating environments. This disorderliness leads to the overlap of many theoretically predicted modes at room temperature. In case of the Tb singly doped series, a prominent peak at 855 cm^{-1} was observed, this peak belongs to the symmetric stretching of V-O. On comparing the spectra of both the series it was observed that the compositions from Na-Tb co-doped series produced slightly more resolved peaks. These peaks can be observed at the 850 cm^{-1} and 825 cm^{-1} and are associated with ν_1

and ν_3 symmetric stretching of VO_4^{3-} tetrahedra respectively. In case of the Tb singly doped series, only the compounds with $\text{Tb} = 0.08$ and $\text{Tb} = 0.12$ showed the hint of a shoulder at 850cm^{-1} but did not show any signs of the ν_3 stretching at 825 cm^{-1} . The doublet observed at 350cm^{-1} associated with E symmetry, observed in all the compositions is attributed to the bending mode. This doublet was found to be more resolved in case of the Na-Tb co-doped samples. Above observation points towards the lack of disorder and higher crystallinity in case of vacancy compensated Na-Tb co-doped samples.

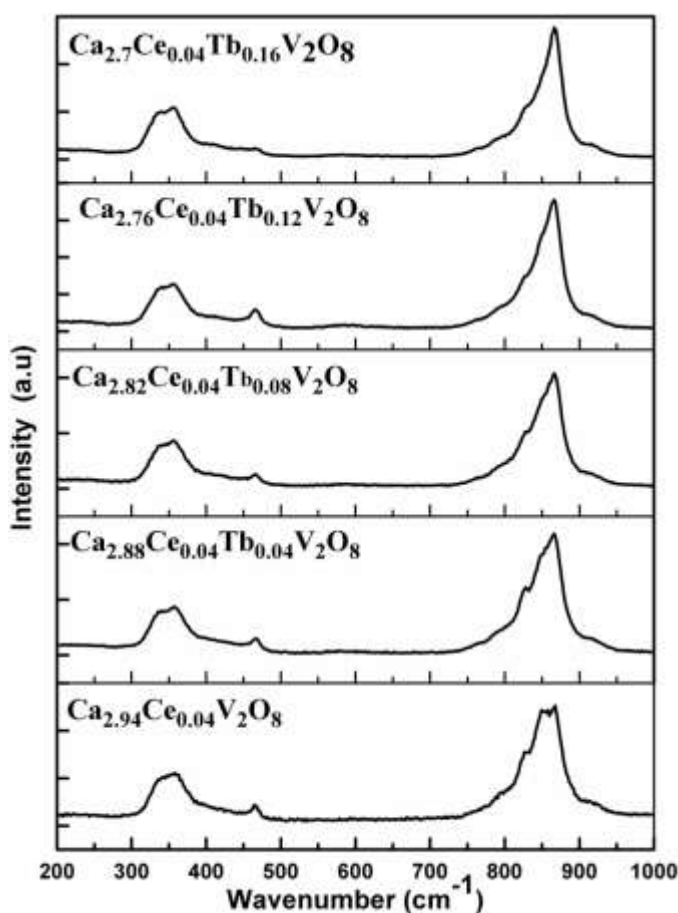


Fig. 4.32 Raman spectra of $\text{Ca}_{2.94-3x/2}\text{Ce}_{0.04}\text{Tb}_x\text{V}_2\text{O}_8$ series

Fig. 4.32 presents Raman spectra of Ce-Tb co-doped $\text{Ca}_3\text{V}_2\text{O}_8$ compositions. The spectra matched well with the reports in the literature. The spectra obtained are almost identical to the spectra obtained in the case of Tb and Na-Tb co-doped samples.

As can be noticed from the spectra the compositions with $Tb = 0.04$ and $Tb = 0.08$ showed a slight hint of peaks as shoulders around the major stretching peak of a ν_1 stretch. These shoulders were not observed in later compositions. Another feature found in the above spectra is the appearance of a hitherto absent small peak at around 460 cm^{-1} that can be associated with bending mode of F_2 symmetry.

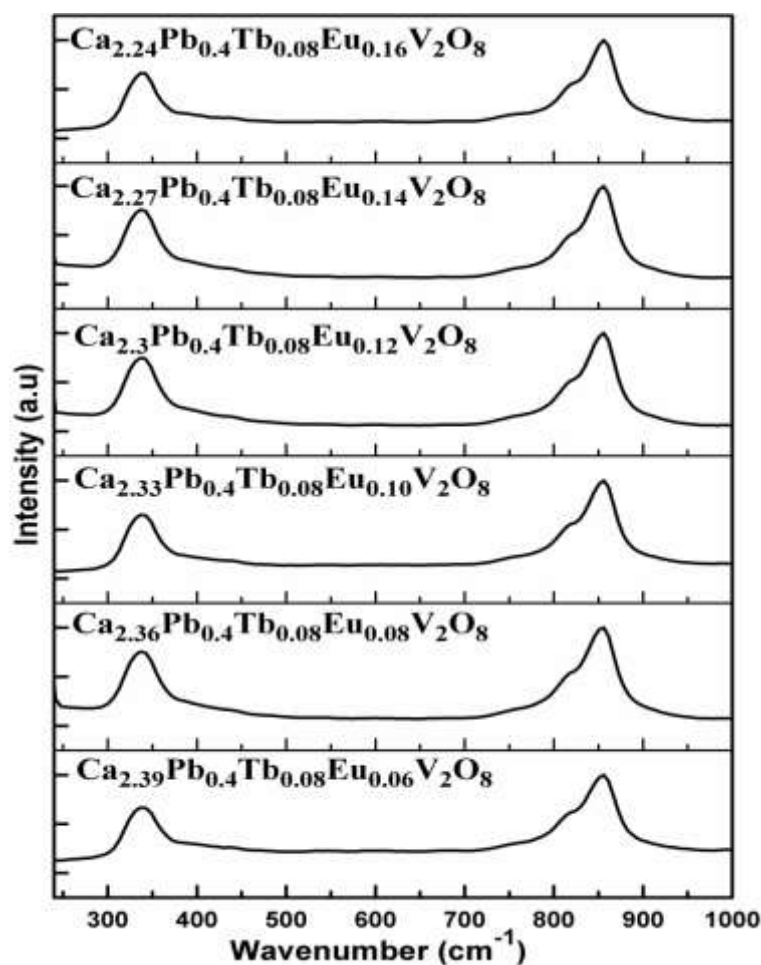


Fig. 4.33 Raman spectra of $Ca_{2.48-3x/2}Pb_{0.4}Tb_{0.08}Eu_xV_2O_8$ series

The Fig. 4.33 presents the Raman spectra of composition from the series $Ca_{2.48-3x/2}Pb_{0.4}Tb_{0.08}Eu_xV_2O_8$. The spectra did not show any peaks other than the expected peaks in the system. This confirms that there were no impurities present in the composition and also substantiates the results of X-ray diffraction. Interesting observations that can be made is the increase in the relative intensity of the bending doublet observed in the region around 350 cm^{-1} . Compared to the previous

compositions, the present compositions did not show any splitting of the doublet. This might indicate some local changes in the structure caused by the doping.

4.5 UV-DRS studies

UV-DRS technique offered important insights regarding the absorbance and band gap energy of the prepared compositions.

4.5.1 Cu inserted $\text{Bi}_4\text{V}_2\text{O}_{11}$

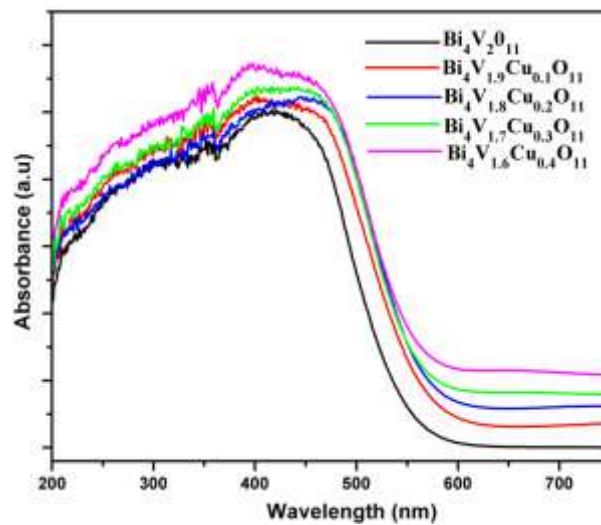


Fig. 4.34 UV-DRS spectra of Cu inserted $\text{Bi}_4\text{V}_2\text{O}_{11}$ series

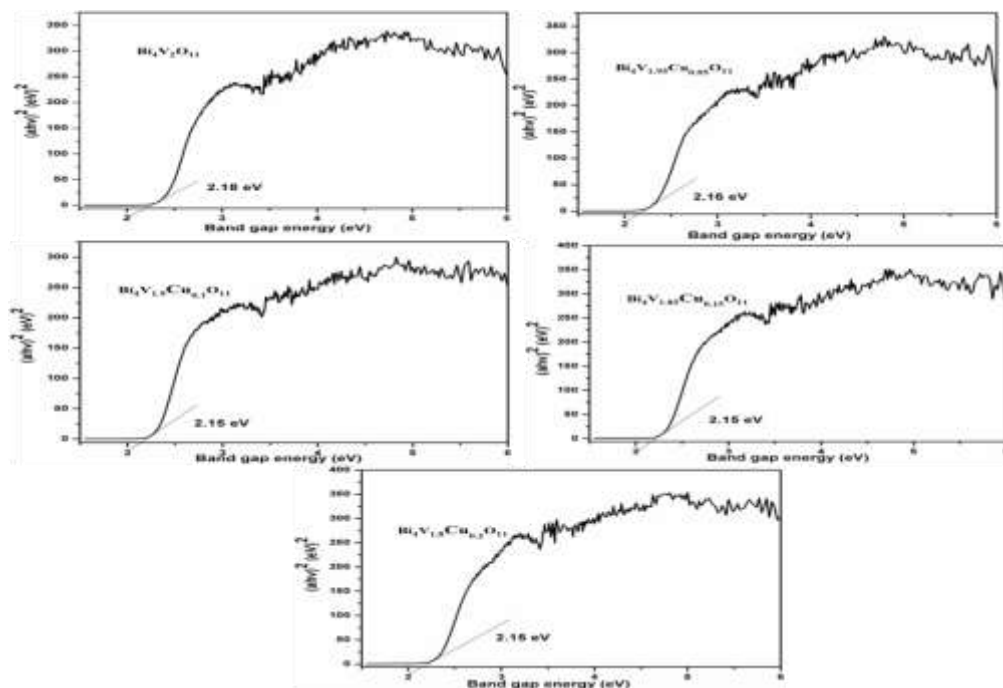


Fig.4.35 Tauc plots of Cu inserted $\text{Bi}_4\text{V}_2\text{O}_{11}$ compositions.

Fig. 4.34 displays the UV-DRS spectra of Cu inserted $\text{Bi}_4\text{V}_2\text{O}_{11}$ compositions. All the compositions showed considerable absorption in the visible light region. The Tauc plots and the band gap values are presented in the Fig.4.35 and Table 4.4 respectively.

Table 4.4 Band gap energy values of $\text{Bi}_4\text{V}_{2-x}\text{Cu}_x\text{O}_{11}$

Compositions	Band gap (eV)
$\text{Bi}_4\text{V}_2\text{O}_{11}$	2.18
$\text{Bi}_4\text{V}_{1.9}\text{Cu}_{0.1}\text{O}_{11}$	2.16
$\text{Bi}_4\text{V}_{1.8}\text{Cu}_{0.2}\text{O}_{11}$	2.15
$\text{Bi}_4\text{V}_{1.7}\text{Cu}_{0.3}\text{O}_{11}$	2.15
$\text{Bi}_4\text{V}_{1.6}\text{Cu}_{0.4}\text{O}_{11}$	2.15

Band gap values ranged from 2.15- 2.18 eV. Pristine $\text{Bi}_4\text{V}_2\text{O}_{11}$ showed the band gap of 2.18 eV. The Cu insertion decreased the band gap to a small extent as observed from the values. The decrease was not continuous as the last three compositions showed identical band gap. The band gap value of $\text{Bi}_4\text{V}_2\text{O}_{11}$ in the present case found to be higher than the value reported by Uma *et al* (2.0 eV) [169].

4.5.2 $\text{M}_3\text{V}_2\text{O}_8$ (M= Ca, Sr and Ba)

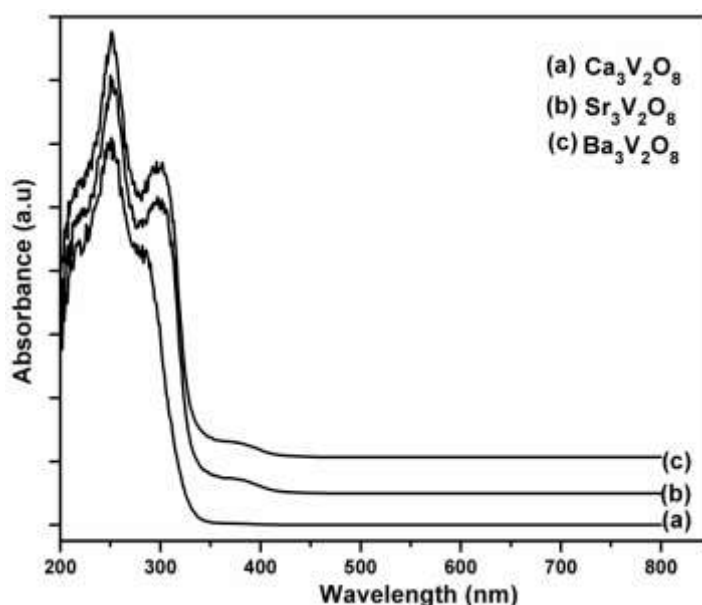


Fig. 4.36 UV-DRS spectra of $\text{M}_3\text{V}_2\text{O}_8$

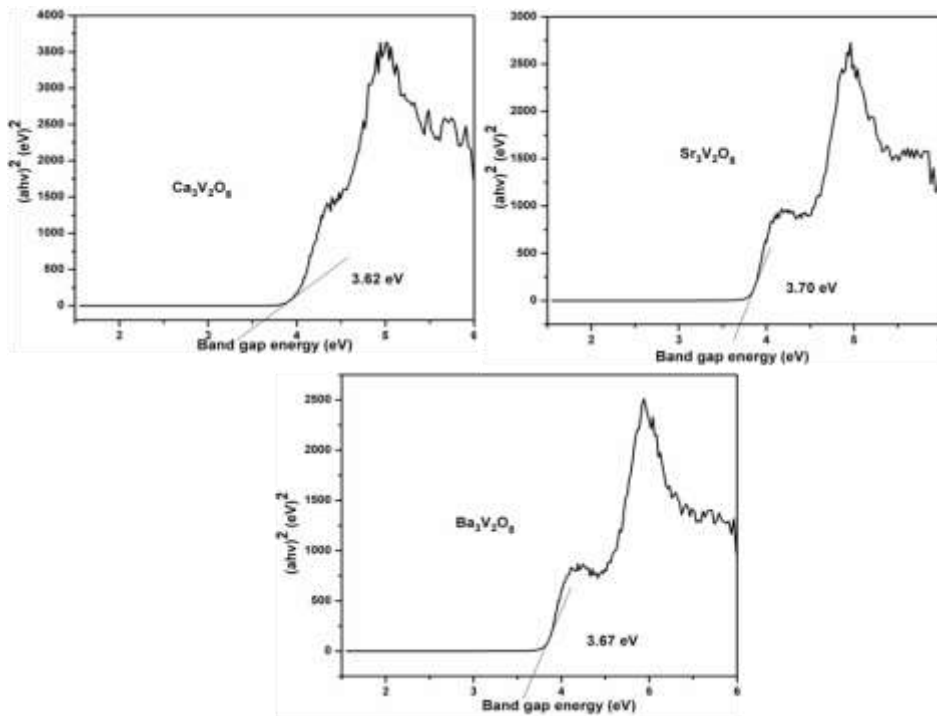


Fig. 4.37. Tauc plots of alkaline earth metal vanadates

Fig. 4.36 and 4.37 shows the DRS and Tauc plots of alkaline earth metal vanadates respectively. $\text{Ca}_3\text{V}_2\text{O}_8$ showed the lowest band gap among the compositions at 3.62 eV. $\text{Sr}_3\text{V}_2\text{O}_8$ and $\text{Ba}_3\text{V}_2\text{O}_8$ exhibited the band gap values of 3.70 eV and 3.67 eV respectively which were according to the trend observed in the literature [261].

4.5.3 R.E doped $\text{Ca}_3\text{V}_2\text{O}_8$ compositions

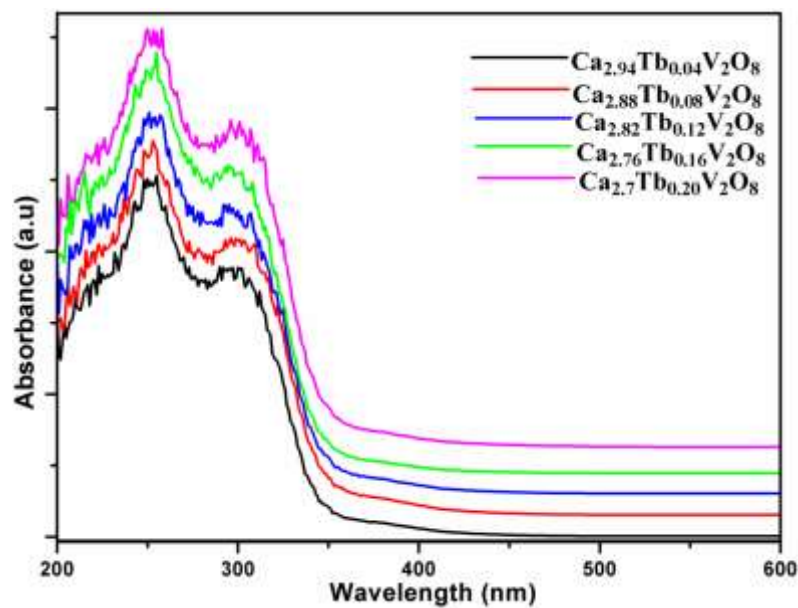


Fig. 4.38. UV-DRS spectra of $\text{Ca}_{3-3x/2}\text{Tb}_x\text{V}_2\text{O}_8$ series

The absorption of $\text{Ca}_3\text{V}_2\text{O}_8$ mainly occurs in the region between 200-400 nm. This absorption is associated with the charge transfer from O to V. This charge transfer transition takes place from HOMO to LUMO. The HOMO is formed by the overlap of O $2p$ non-bonding orbitals having 't' symmetry, whereas the LUMO is formed by a linear combination of O $2p$ orbital and anti-bonding V $3d$ orbital. The continuous absorption band is composed of two prominent components. The first component at 300 nm is attributed to the transition from $^1\text{A}_1$ to $^1\text{T}_1$ whereas the second component at 250 nm is attributed to the transition from $^1\text{A}_1$ to $^1\text{T}_2$. Tb transitions of $4f-5d$ also take place in the UV region [264-267].

Fig. 4.38 presents the UV-DRS spectra of the Tb singly doped compositions. The two basic components of charge transfer were clearly visible in the spectra. The fine absorptive structure of Tb was not seen as they are expected to get buried in the continuous charge transfer spectra of the $\text{Ca}_3\text{V}_2\text{O}_8$ host. Tauc plots derived from the absorbance spectra of each composition to find the band gap energy are displayed in Fig. 4.39. The obtained band gap values are tabulated in Table 4.5.

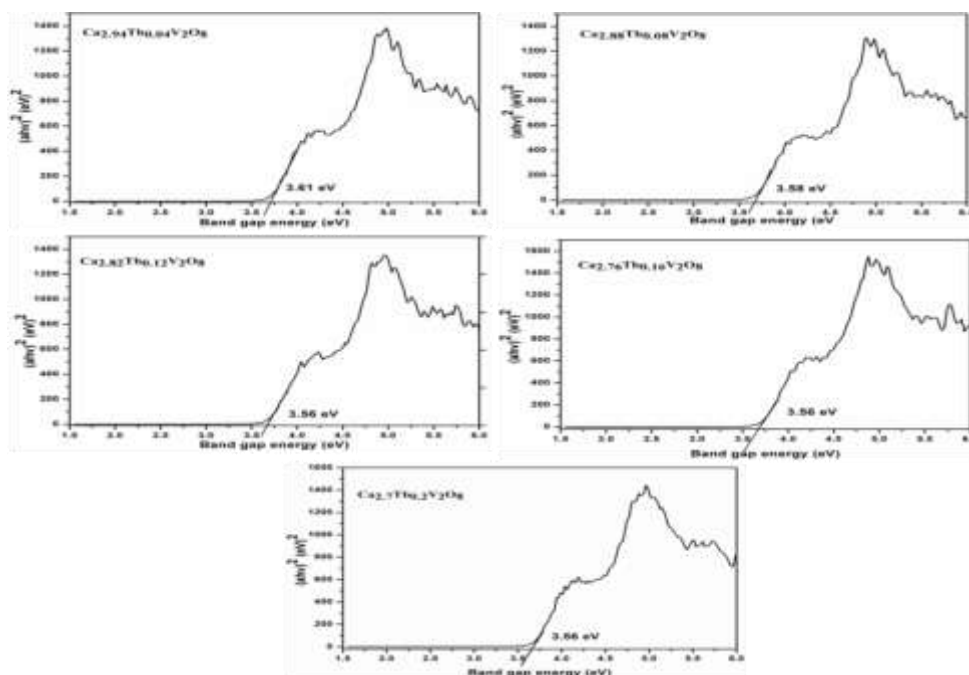


Fig. 4.39 The Tauc plots of $\text{Ca}_{3-3x/2}\text{Tb}_x\text{V}_2\text{O}_8$ compositions.

Table 4.5 Band gap energy values of $\text{Ca}_{3-3x/2}\text{Tb}_x\text{V}_2\text{O}_8$

Compositions	Band gap (eV)
$\text{Ca}_{2.94}\text{Tb}_{0.04}\text{V}_2\text{O}_8$	3.61
$\text{Ca}_{2.88}\text{Tb}_{0.08}\text{V}_2\text{O}_8$	3.58
$\text{Ca}_{2.82}\text{Tb}_{0.12}\text{V}_2\text{O}_8$	3.56
$\text{Ca}_{2.76}\text{Tb}_{0.16}\text{V}_2\text{O}_8$	3.56
$\text{Ca}_{2.7}\text{Tb}_{0.2}\text{V}_2\text{O}_8$	3.56

The band gap values were found to be in the range between 3.56 to 3.61 eV. A slight lowering of band gap values was seen as the Tb concentration increased.

The UV-DRS spectra of Na-Tb co-doped spectra are presented in Fig. 4.40. The Tauc plots and the band gap values are presented in the Fig 4.41 and Table 4.6 respectively.

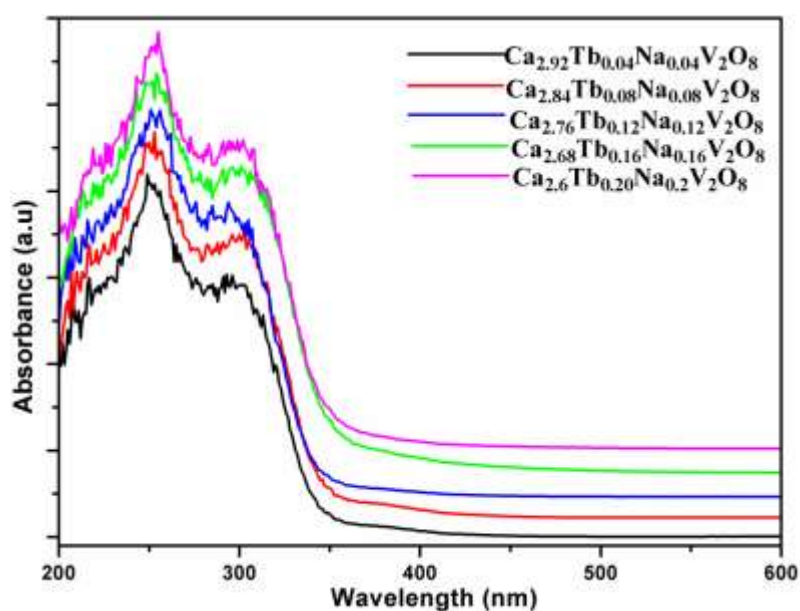


Fig. 4.40 Raman spectra of $\text{Ca}_{3-2x}\text{Tb}_x\text{Na}_x\text{V}_2\text{O}_8$ series

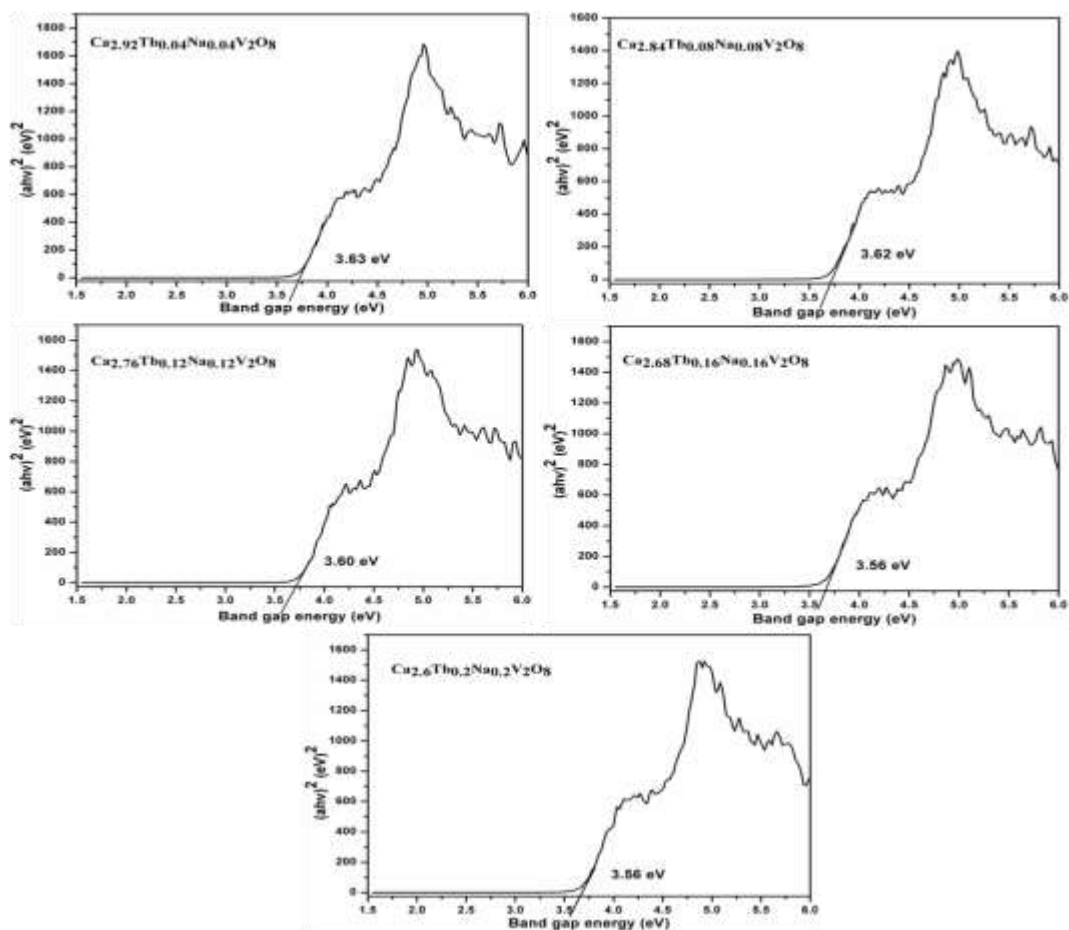


Fig. 4.41 Tauc plots of $Ca_{3-2x}Tb_xNa_xV_2O_8$ series

Table 4.6 Band gap energy values of $Ca_{3-2x}Tb_xNa_xV_2O_8$

Compositions	Band gap (eV)
$Ca_{2.92}Na_{0.04}Tb_{0.04}V_2O_8$	3.63
$Ca_{2.84}Na_{0.08}Tb_{0.08}V_2O_8$	3.62
$Ca_{2.76}Na_{0.12}Tb_{0.12}V_2O_8$	3.60
$Ca_{2.68}Na_{0.16}Tb_{0.16}V_2O_8$	3.56
$Ca_{2.6}Na_{0.2}Tb_{0.2}V_2O_8$	3.56

The absorbance pattern shown by Na-Tb co-doped series was almost similar to the Tb singly doped compounds. A slight lowering of band gap values was observed after the increase in doping. This decrease came to the halt at Tb and Na concentration of 0.16 as last two compositions had the same band gap value.

UV-DRS spectra of Ce-Tb co-doped samples are displayed in the Fig. 4.42.

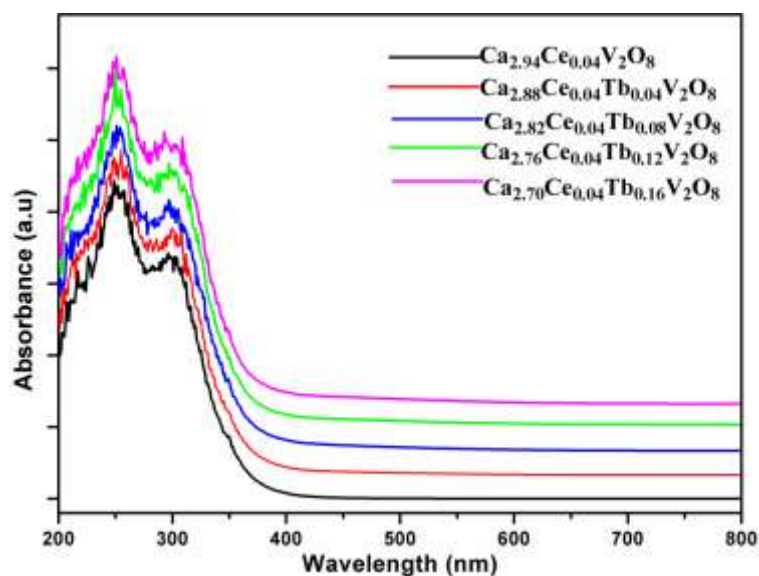


Fig. 4.42 UV-DRS spectra of $\text{Ca}_{2.94-3x/2}\text{Ce}_{0.04}\text{Tb}_x\text{V}_2\text{O}_8$ series

The absorbance spectra of compositions in this series showed the standard charge transfer transition of the vanadate moiety. Due to the continuous band absorbance showed by the host the fine absorption lines of both the R.E ions Ce and Tb were not visible in the absorbance spectra. The Tauc plots of the respective compositions and their band gap values are given in Fig. 4.43 and Table 4.7 respectively.

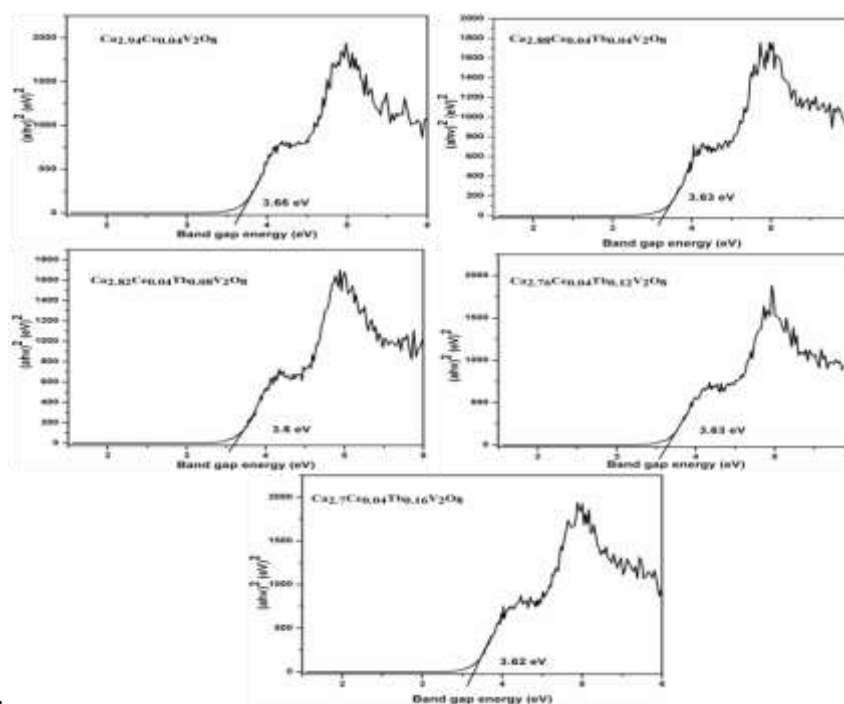


Fig. 4.43 Tauc plots of $\text{Ca}_{2.94-3x/2}\text{Ce}_{0.04}\text{Tb}_x\text{V}_2\text{O}_8$ series

Table 4.7 Band gap energy values of $\text{Ca}_{2.94-3x/2}\text{Ce}_{0.04}\text{Tb}_x\text{V}_2\text{O}_8$

Compositions	Band gap (eV)
$\text{Ca}_{2.94}\text{Ce}_{0.04}\text{V}_2\text{O}_8$	3.66
$\text{Ca}_{2.84}\text{Ce}_{0.04}\text{Tb}_{0.04}\text{V}_2\text{O}_8$	3.63
$\text{Ca}_{2.76}\text{Ce}_{0.04}\text{Tb}_{0.08}\text{V}_2\text{O}_8$	3.60
$\text{Ca}_{2.68}\text{Ce}_{0.04}\text{Tb}_{0.12}\text{V}_2\text{O}_8$	3.63
$\text{Ca}_{2.6}\text{Ce}_{0.04}\text{Tb}_{0.16}\text{V}_2\text{O}_8$	3.62

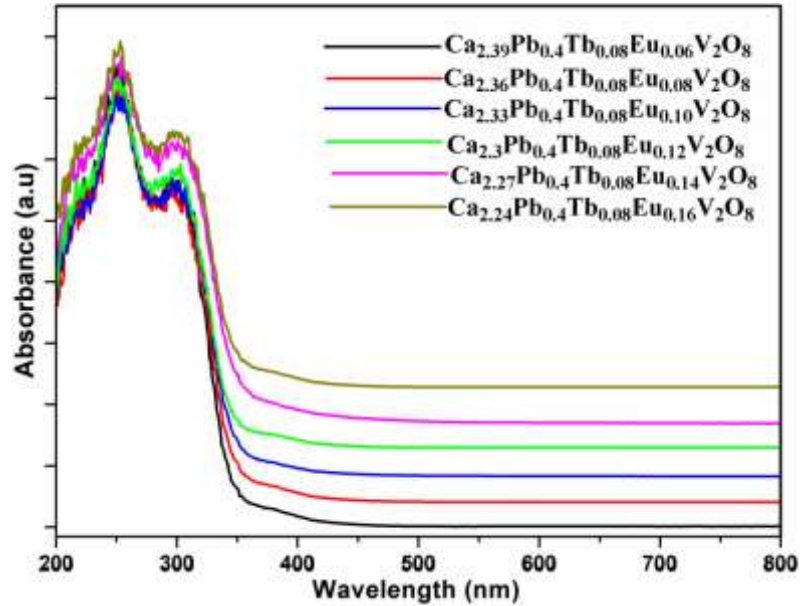
**Fig. 4.44** UV-DRS spectra of $\text{Ca}_{2.48-3x/2}\text{Pb}_{0.4}\text{Tb}_{0.08}\text{Eu}_x\text{V}_2\text{O}_8$

Fig. 4.44 presents the UV-DRS spectra of $\text{Ca}_{2.48-3x/2}\text{Pb}_{0.4}\text{Tb}_{0.08}\text{Eu}_x\text{V}_2\text{O}_8$. As can be seen from the absorbance spectra the basic features showed by the previous compositions are retained here indicating that the inclusion of Pb^{2+} has a little effect on the overall electronic structure of the host lattice. The Tauc plots and the band gap values are presented in Fig. 4.45 and Table 4.8 respectively.

Table 4.8 Band gap energy values of $\text{Ca}_{2.48-3x/2}\text{Pb}_{0.4}\text{Tb}_{0.08}\text{Eu}_x\text{V}_2\text{O}_8$

Compositions	Band gap (eV)
$\text{Ca}_{2.39}\text{Pb}_{0.4}\text{Tb}_{0.08}\text{Eu}_{0.06}\text{V}_2\text{O}_8$	3.59
$\text{Ca}_{2.36}\text{Pb}_{0.4}\text{Tb}_{0.08}\text{Eu}_{0.08}\text{V}_2\text{O}_8$	3.58
$\text{Ca}_{2.33}\text{Pb}_{0.4}\text{Tb}_{0.08}\text{Eu}_{0.10}\text{V}_2\text{O}_8$	3.57
$\text{Ca}_{2.30}\text{Pb}_{0.4}\text{Tb}_{0.08}\text{Eu}_{0.12}\text{V}_2\text{O}_8$	3.58
$\text{Ca}_{2.27}\text{Pb}_{0.4}\text{Tb}_{0.08}\text{Eu}_{0.14}\text{V}_2\text{O}_8$	3.56
$\text{Ca}_{2.24}\text{Pb}_{0.4}\text{Tb}_{0.08}\text{Eu}_{0.16}\text{V}_2\text{O}_8$	3.56

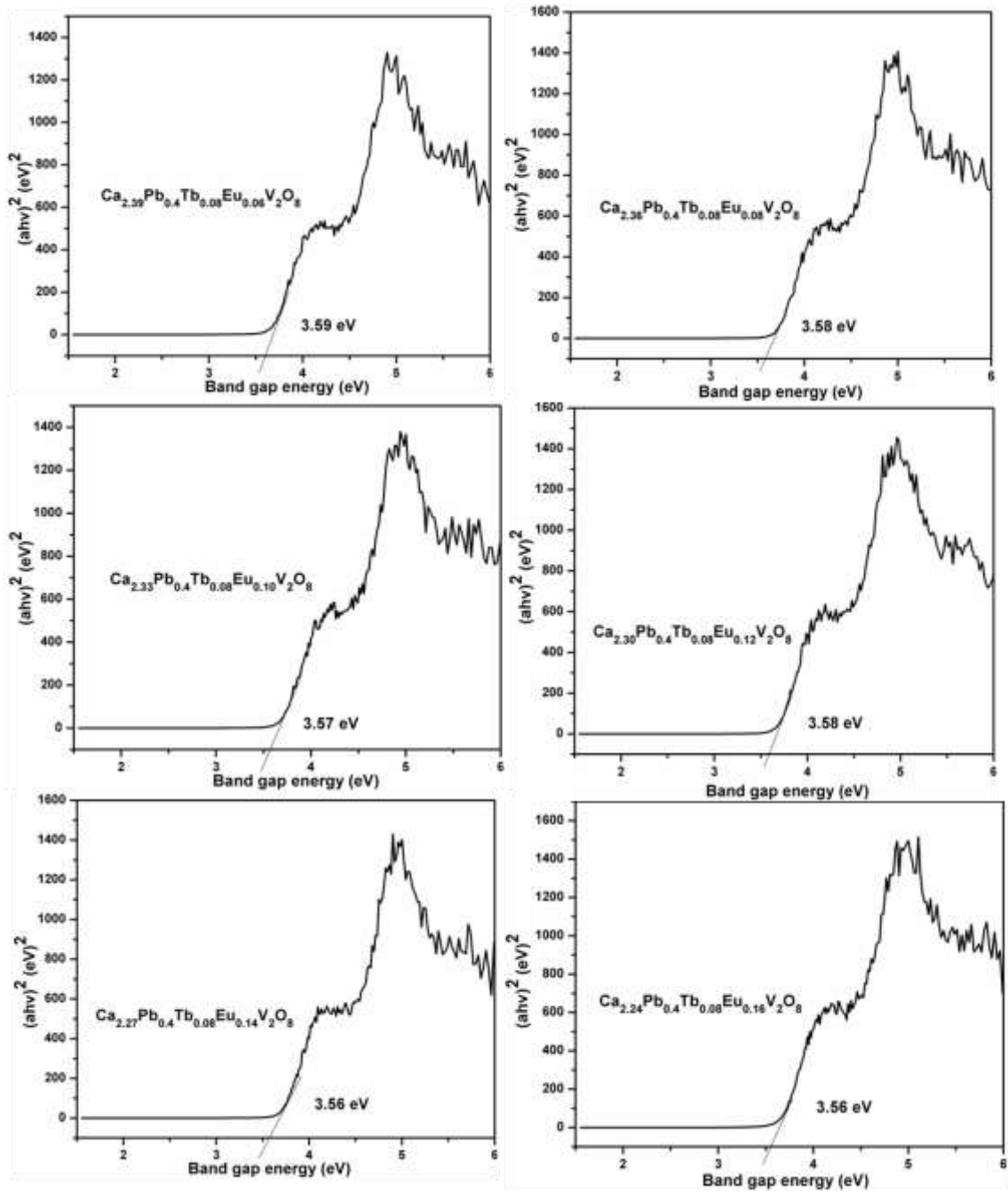


Fig. 4.45 Tauc plots of $\text{Ca}_{2.48-3x/2}\text{Pb}_{0.4}\text{Tb}_{0.08}\text{Eu}_x\text{V}_2\text{O}_8$ series

4.6 XPS studies

XPS studies provided the binding energy values of the constituent elements of the compounds and thus the oxidation states of the elements were determined.

4.6.1 Cu/Bi₂Mo₃O₁₂ catalysts

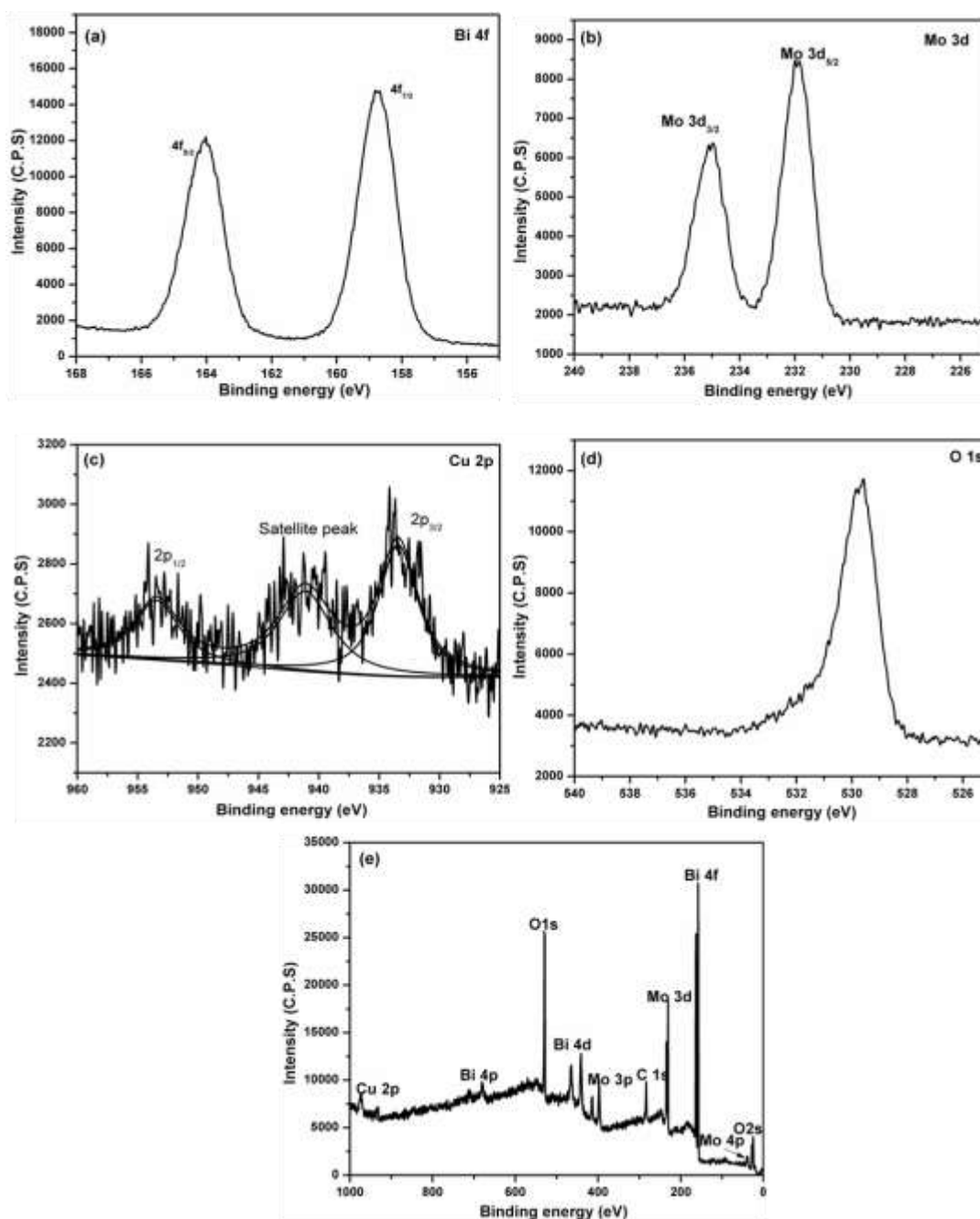


Fig. 4.46 XPS spectra of 2% Cu/Bi₂Mo₃O₁₂ catalysts (a) Bi 4f (b) Mo 3d (c) Cu 2p (d) O 1s and (e) Full survey scan.

Fig. 4.46 shows the XPS spectra of the 2% Cu/Bi₂Mo₃O₁₂ catalyst. The full survey scan of the composition showed the presence of all the expected elements in the composition without any impurities. Bi 4f scan showed the two peaks at 158.8 eV and 164.1 eV which are attributed to the binding energies of 4f_{7/2} and 4f_{5/2} respectively. The difference between the two peaks was 5.3 eV. This observation substantiates the presence of Bi³⁺ in system [268, 269]. Mo 3d scan showed the presence of two peaks at around 232.2 eV and 235.2 eV for 3d_{5/2} and 3d_{3/2} respectively, signifying the presence of Mo in 6+ oxidation state [270]. Cu 2p scan is presented in the above figure showed the two peaks at 934.0 eV and 953.8 eV attributable to 2p_{3/2} and 2p_{1/2} respectively confirming the presence of Cu in 2+ oxidation state [271]. O 1s peak was spanned from 530 eV signifying the lattice oxygen.

4.6.2 Bi₂Mo_{1-x}W_xO₆ series

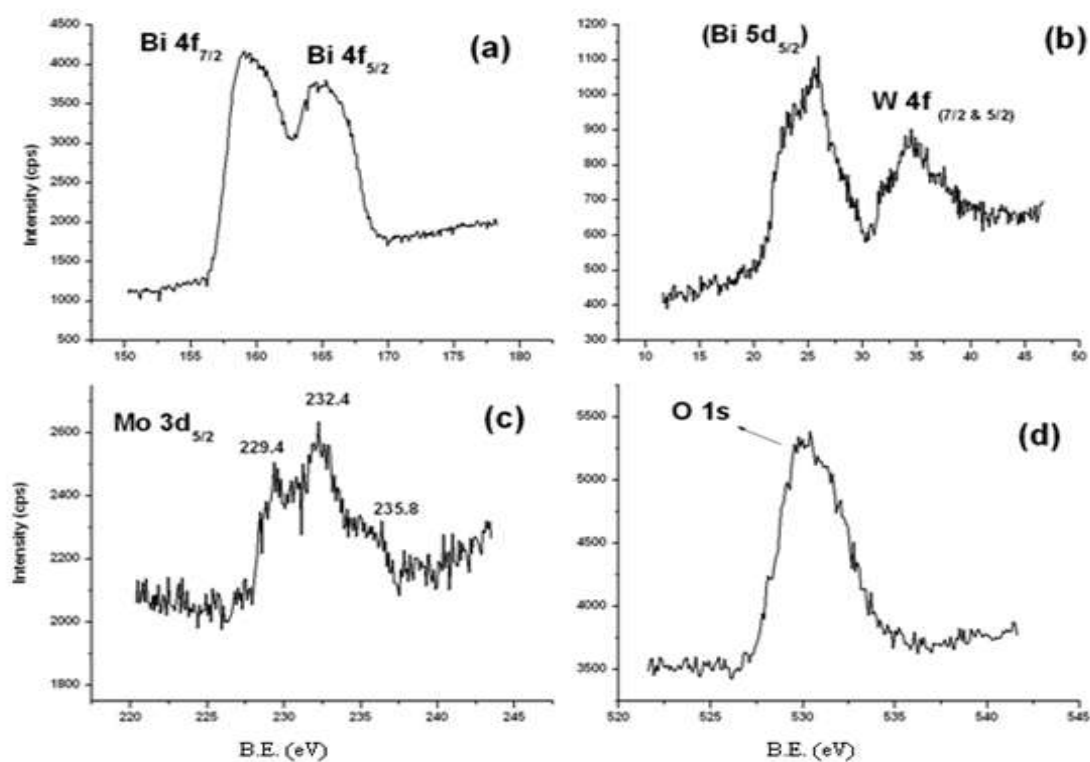


Fig. 4.47 XPS spectra of Bi₂Mo_{0.6}W_{0.4}O₆ (a) Bi 4f. (b) Bi 5d, W 4f. (c) Mo 3d. (d) O 1s.

XPS studies confirmed the presence of all three metal components without any impurities. XPS spectra of $\text{Bi}_2\text{Mo}_{0.6}\text{W}_{0.4}\text{O}_6$ are presented in Fig. 4.47. Bi $4f_{5/2}$ and Bi $4f_{7/2}$ spin-orbit splitting photoelectrons are located at 164.4 and 159.1 eV respectively as displayed in Fig. 4.47(a) confirming the presence of Bi^{3+} in the crystal lattice. Fig. 4.47(b) shows W $4f_{7/2}$ and W $4f_{5/2}$ spin-orbit splitting photoelectrons from WO_6 octahedra which showed binding energies at 35.20 and 36.60 eV respectively. A typical Mo 3d spectrum is displayed in Fig. 4.47(c). The Mo $3d_{5/2}$ binding energy peaks were seen between 232.4 and 235.8 eV denoting Mo^{6+} species. The peak at 229.4 eV is assigned to the Mo^{4+} , confirming that there are two oxidation states present for molybdenum. Except for the occurrence of Mo^{4+} , all the above observations are in accordance with the reported XPS studies. The occurrence of Mo^{4+} in the composition can be attributed to the residual carbon adhering intimately to the material's surface, this carbon may get oxidized by taking oxygen from the lattice thus reducing Mo^{6+} in the process.

Fig. 4.47 (d) presents XPS peak for the O species, attributed to crystal lattice oxygen and adsorbed oxygen. In the literature, XPS is considered to be a potent means to estimate oxygen mobility in the crystal lattice. Among the three types of oxygen reported, I, II and III, Type I oxygen has lowest binding energy (~530 eV) and is bonded strongly to the metal ions, type II is the oxygen which has highest binding energy (~533 eV) and is weakly bonded to the oxide surface whereas the type III oxygen with intermediate binding energy is considered as the measure of oxygen mobility. Broadening of the XPS spectra towards the higher binding energy values is indicative of a decrease in the valence electron density around oxygen making its bonding with the Mo or W weak rendering more mobility to the lattice oxygen. As can be seen from the Fig. 4.47(d) the broadened XPS spectra indicate the presence of

mobile oxygen species [272]. This phenomenon is reported earlier by Rangel et al. [123] for similar compositions such as $\text{Bi}_2\text{Mo}_{0.75}\text{W}_{0.25}\text{O}_6$ in explaining its enhanced catalytic activity for CO oxidation.

4.6.3 $\text{V}_{1-x}\text{Cu}_x\text{SbO}_4$

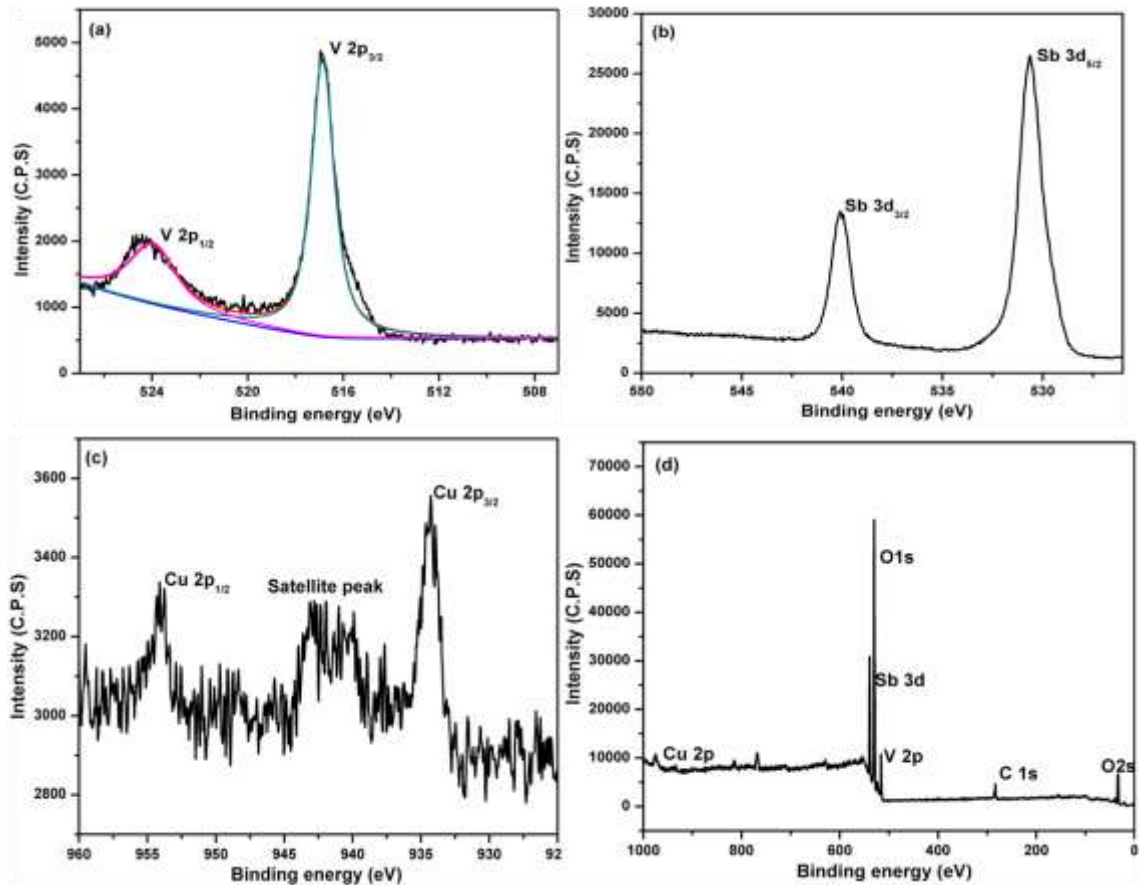


Fig. 4.48 XPS scan of $\text{V}_{0.9}\text{Cu}_{0.1}\text{SbO}_4$ (a) V 2p (b) Sb 3d (c) Cu 2p and (d) Full survey scan.

Fig. 4.48 presents the XPS spectra of $\text{V}_{0.9}\text{Cu}_{0.1}\text{SbO}_4$ composition. The full survey scan presented above showed all the expected constituent elements of the composition. V 2p scan showed the peaks at 516.5 eV and 524.0 eV attributed to the V $2p_{3/2}$ and V $2p_{1/2}$ respectively, confirming the V^{4+} state in the composition [273]. A possibility of occurrence of V^{3+} in small amounts cannot be ruled out as it can get easily lost in the major component of V $2p_{3/2}$ of 4+ state. On deconvolution no significant component of V^{3+} was detected. Sb 3d showed the peaks at 530.5 eV and 539.9 eV, these peaks are

attributable to $3d_{5/2}$ and $3d_{3/2}$ components of Sb respectively. The obtained binding energy values are characteristic of Sb^{5+} state [274]. Cu 2p scan displayed above, showed the characteristic peaks at 934.0 eV and 953.7 eV which are assigned to Cu $2p_{3/2}$ and $2p_{1/2}$ components respectively confirming the presence of Cu in 2+ state.

4.6.4 Cu-K-V-Sb-O composition

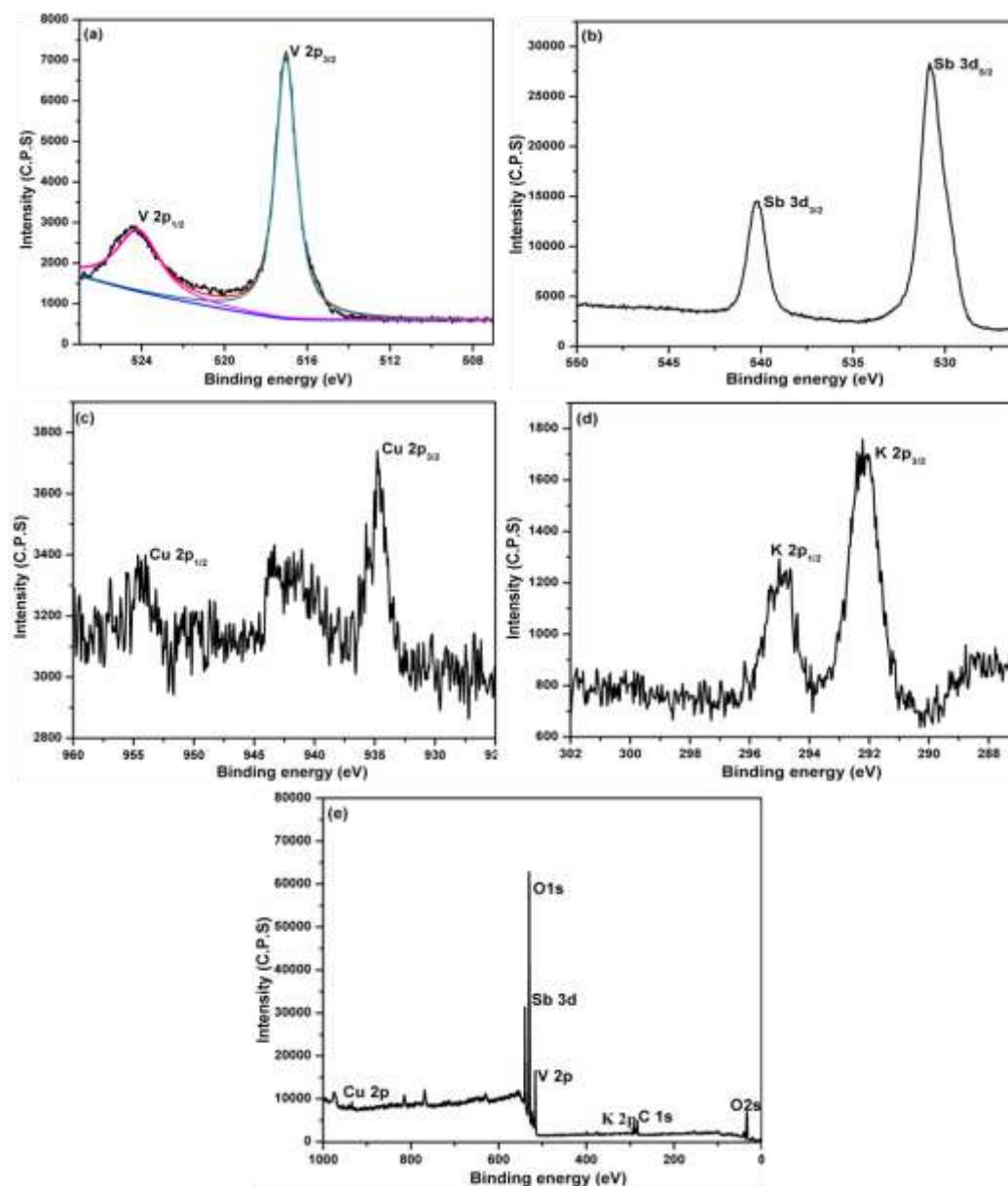


Fig. 4.49 XPS scan of $Cu_{0.2}K_{0.1}V_{0.8}Sb_{0.9}O$ (a) V 2p (b) Sb 3d (c) Cu 2p (d) K 2p and (e) Full survey scan

Fig. 4.49 presents the XPS spectra of $\text{Cu}_{0.2}\text{K}_{0.1}\text{V}_{0.8}\text{Sb}_{0.9}\text{O}$ composition. The full survey scan indicated the presence of all the constituent elements in the composite catalyst. V 2p scan showed peaks at 516.8 eV and 524.0 eV which are assigned to $2p_{3/2}$ and $2p_{1/2}$ component of V. These characteristic peaks indicated the presence of V^{4+} in the composition. The peaks observed at 530.7 eV and 539.9 eV in case of individual scan of Sb 3d are attributed to the $3d_{5/2}$ and $3d_{3/2}$ components respectively. These peaks substantiated the presence of Sb^{5+} in the composition. The characteristic lines of Cu 2p were observed at 934.6 eV and 954.0 eV corresponding to the $2p_{3/2}$ and $2p_{1/2}$ lines respectively. A satellite peak in between these two peaks was observed. This observation substantiates the presence of Cu^{2+} in the composition. The characteristic lines of K^+ were observed at 292.0 eV and 294.7 eV corresponding to $2p_{3/2}$ and $2p_{1/2}$ lines respectively.

4.6.5 Tb and Na-Tb co-doped $\text{Ca}_3\text{V}_2\text{O}_8$

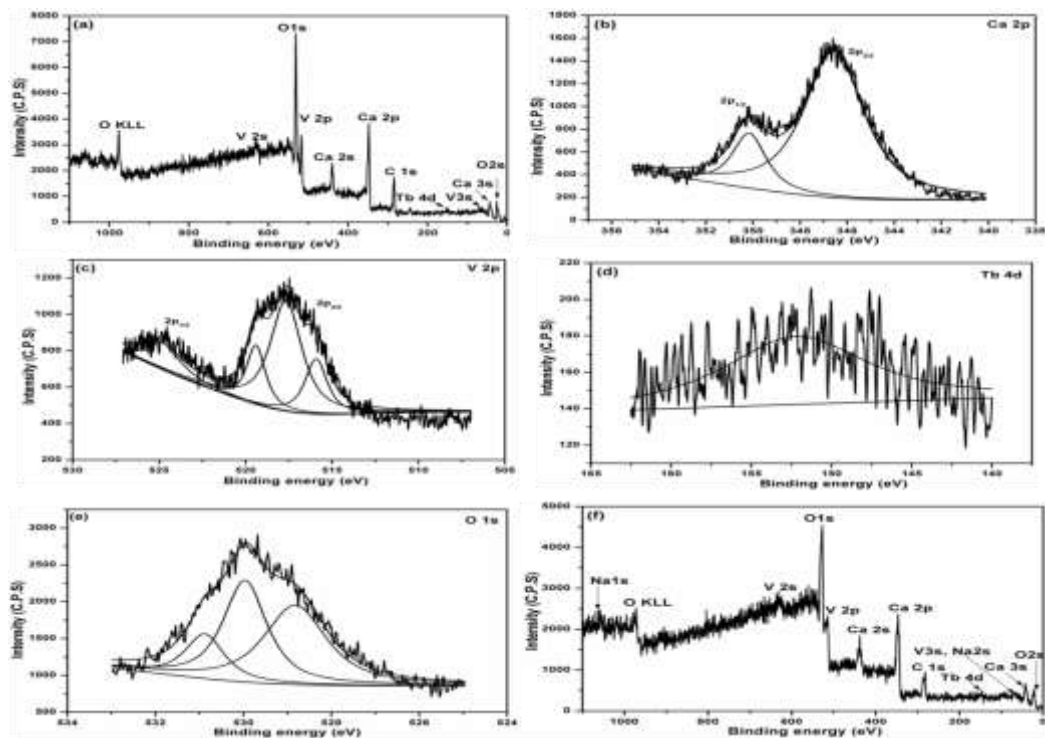


Fig. 4.50 XPS spectra, (a) Full scan of $\text{Ca}_{2.94}\text{Tb}_{0.04}\text{V}_2\text{O}_8$, (b) Ca 2p scan, (c) V 2p scan, (d) Tb 4d scan, (e) O 1s scan and (f) Full scan of $\text{Ca}_{2.92}\text{Tb}_{0.04}\text{Na}_{0.04}\text{V}_2\text{O}_8$

The full elemental scans of $\text{Ca}_{2.94}\text{Tb}_{0.04}\text{V}_2\text{O}_8$ and $\text{Ca}_{2.92}\text{Tb}_{0.04}\text{Na}_{0.04}\text{V}_2\text{O}_8$ are presented in the Fig 4.50 (a) and 4.50 (f) respectively. The main identifying peaks of the expected elements in both the compositions are marked in the spectra. No peaks corresponding to any other element was located in the spectra confirming that no impurities were introduced in the compositions during the preparative process.

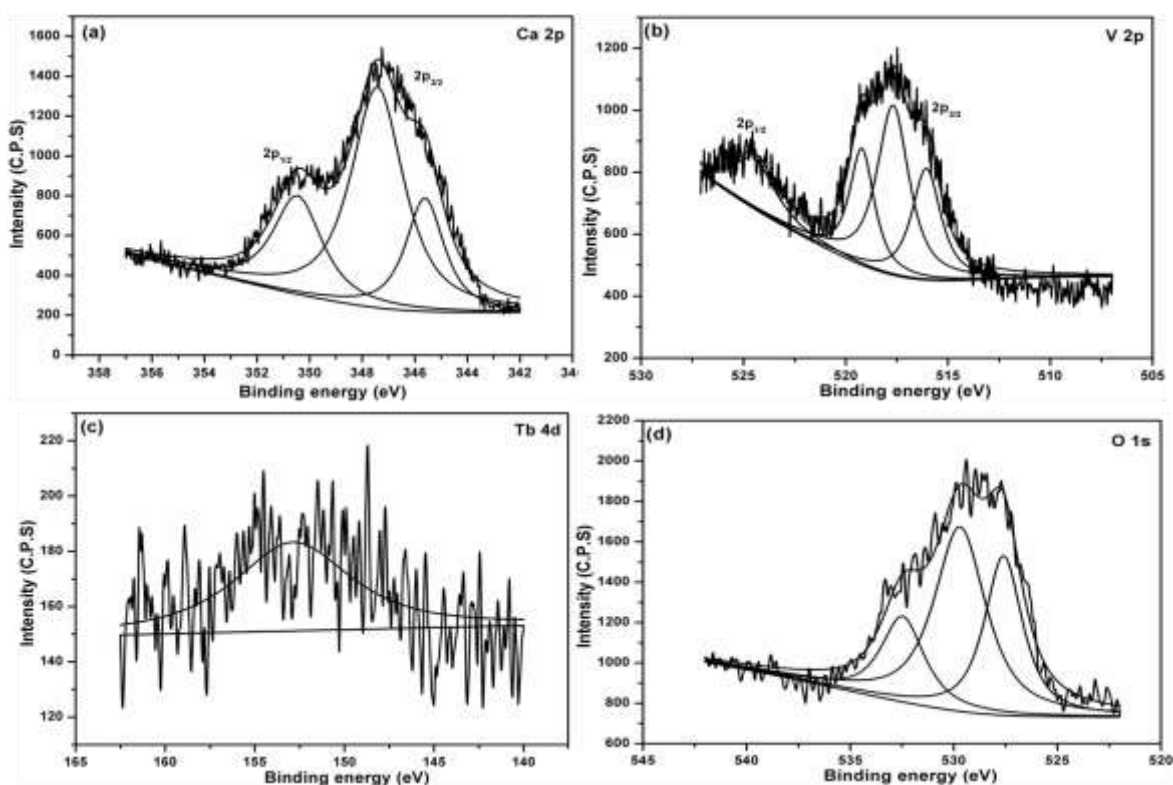


Fig. 4.51 (a)Ca 2p scan, (b) V 2p scan, (c) Tb 4d scan, (d) O 1s scan of $\text{Ca}_{2.92}\text{Tb}_{0.04}\text{Na}_{0.04}\text{V}_2\text{O}_8$

Individual elemental scans of Ca 2p, V 2p, Tb 4d and O 1s of $\text{Ca}_{2.94}\text{Tb}_{0.04}\text{V}_2\text{O}_8$ and $\text{Ca}_{2.92}\text{Tb}_{0.04}\text{Na}_{0.04}\text{V}_2\text{O}_8$ are presented in the Figs. 4.50 and 4.51 respectively. In case of $\text{Ca}_{2.94}\text{Tb}_{0.04}\text{V}_2\text{O}_8$, the Ca 2p_{3/2} and Ca 2p_{1/2} components were observed at 346.5 and 350.1 eV respectively confirming the Ca²⁺ state [261, 275]. V 2p_{3/2} and 2p_{1/2} peaks were observed at 517.6 and 525.eV respectively confirming the oxidation state of 5+. V 2p_{3/2} was deconvoluted in a lower energy component located at 515.9eV which might consider belonging to V⁴⁺. In the literature, some authors have reported the presence of all the oxidation states of V namely 3+, 4+, 5+ [276, 277]. In our case, we could not

trace the 3+ oxidation state. Tb 4d peak found at 150 eV confirms Tb³⁺ in the composition. O 1s peak centred at around 530 eV constituted of overlaps signifying the presence of adsorbed and different type of oxygen ions present in the crystal lattice.

Similarly, in case of Ca_{2.92}Tb_{0.04}Na_{0.04}V₂O₈, Ca 2p_{3/2} and 2p_{1/2} were located at 517.6 and 525.0 eV respectively, whereas V 2p_{3/2} and V 2p_{1/2} were located at 517.6 e and 524.6 eV respectively. Thus, confirming the Ca²⁺ and V⁵⁺ states. V 2p_{3/2} component here was also seen to be deconvoluted into lower energy peak which again can be attributed to the presence of some V⁴⁺ in the crystal lattice. Tb was observed at around 150 eV confirming its 3+ state. O 1s was deconvoluted in a similar pattern as was for Ca_{2.94}Tb_{0.04}V₂O₈ indicating different types of oxygen ions present in the crystal lattice.

4.7 SEM studies

SEM studies provided the information regarding the morphology and texture of the prepared catalysts and phosphors.

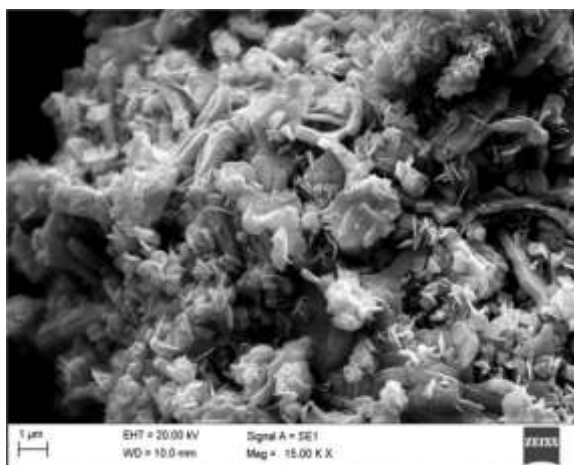


Fig. 4.52 SEM image of 4% Cu/Bi₂Mo₃O₁₂

Fig. 4.52 displays the representative SEM image of 4% Cu/Bi₂Mo₃O₁₂ catalysts. An agglomerated morphology was seen in the image. Flake or whisker like particles were homogeneously scattered on big agglomerated particles throughout. The smaller

particles are considered to be the CuO particles supported on bigger $\text{Bi}_2\text{Mo}_3\text{O}_{12}$ particles. The SEM image therefore suggests homogeneous distribution of Cu species on the $\text{Bi}_2\text{Mo}_3\text{O}_{12}$ catalyst surface.

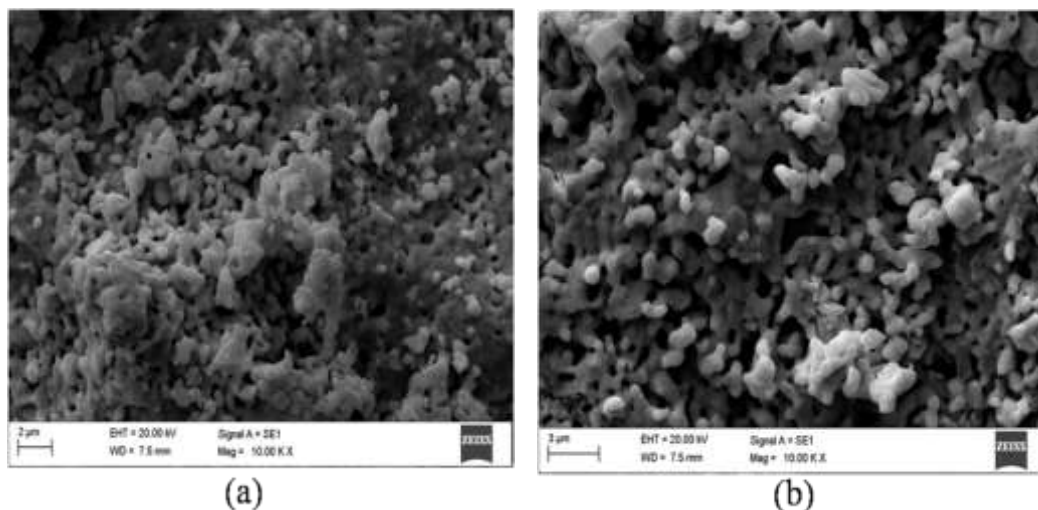


Fig. 4.53 SEM images of (a) $\text{Bi}_4\text{V}_2\text{O}_{11}$ and (b) $\text{Bi}_4\text{V}_{1.8}\text{Cu}_{0.2}\text{O}_{11}$

Fig. 4.53(a) and (b) represents the SEM micrographs of $\text{Bi}_4\text{V}_2\text{O}_{11}$ and $\text{Bi}_4\text{V}_{1.8}\text{Cu}_{0.2}\text{O}_{11}$ respectively. The porous morphology was seen in both the compositions. No significant change in morphology was observed with the Cu doping.

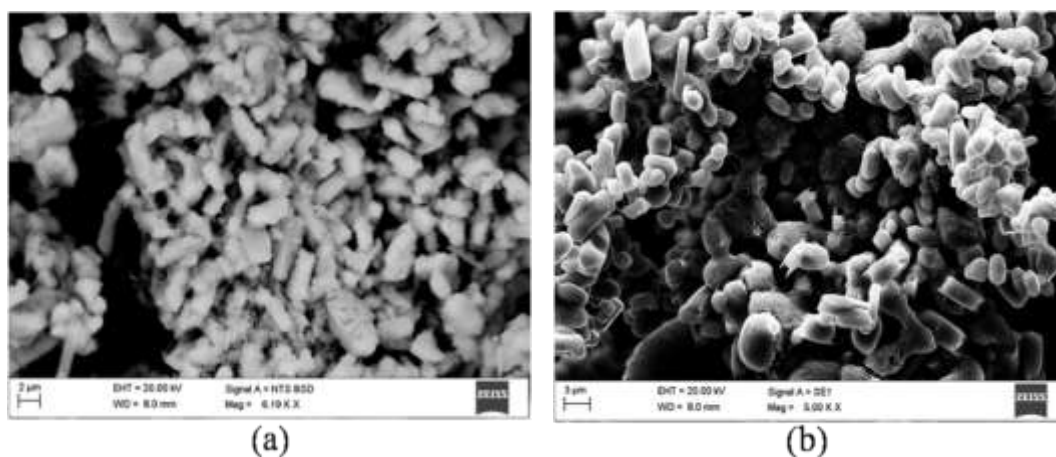


Fig. 4.54 SEM images of (a) $\text{V}_{0.9}\text{Cu}_{0.1}\text{O}_4$ and (b) $\text{Cu}_{0.1}\text{K}_{0.05}\text{V}_{0.9}\text{Sb}_{0.98}\text{O}$

Figs 4.54 (a) and 4.54 (b) display the SEM micrographs of $\text{V}_{0.9}\text{Cu}_{0.1}\text{O}_4$ and $\text{Cu}_{0.1}\text{K}_{0.05}\text{V}_{0.9}\text{Sb}_{0.98}\text{O}$ respectively. Both the compositions showed agglomerated morphology. $\text{V}_{0.9}\text{Cu}_{0.1}\text{O}_4$ composition majorly showed the rod or spindle shaped

morphology whereas, the SEM image of the composite catalysts along with the presence of rod like morphology, showed mixed morphology consisting of spherical shaped particles indicating the presence of mixture of more than one phase in the catalysts system.

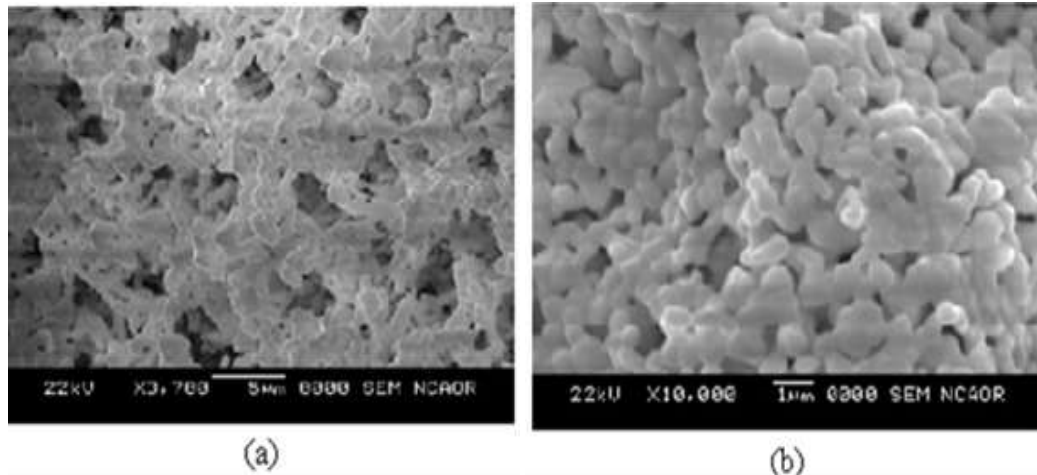


Fig. 4.55 SEM images of (a) Bi_2MoO_6 (b) $\text{Bi}_2\text{Mo}_{0.6}\text{W}_{0.4}\text{O}_6$

Fig. 4.55 (a) and (b) presents the SEM images of Bi_2MoO_6 and $\text{Bi}_2\text{Mo}_{0.6}\text{W}_{0.4}\text{O}_6$ showing the porous but agglomerated morphology. A particular change in morphology was not seen after the W doping as can be seen from the above images.

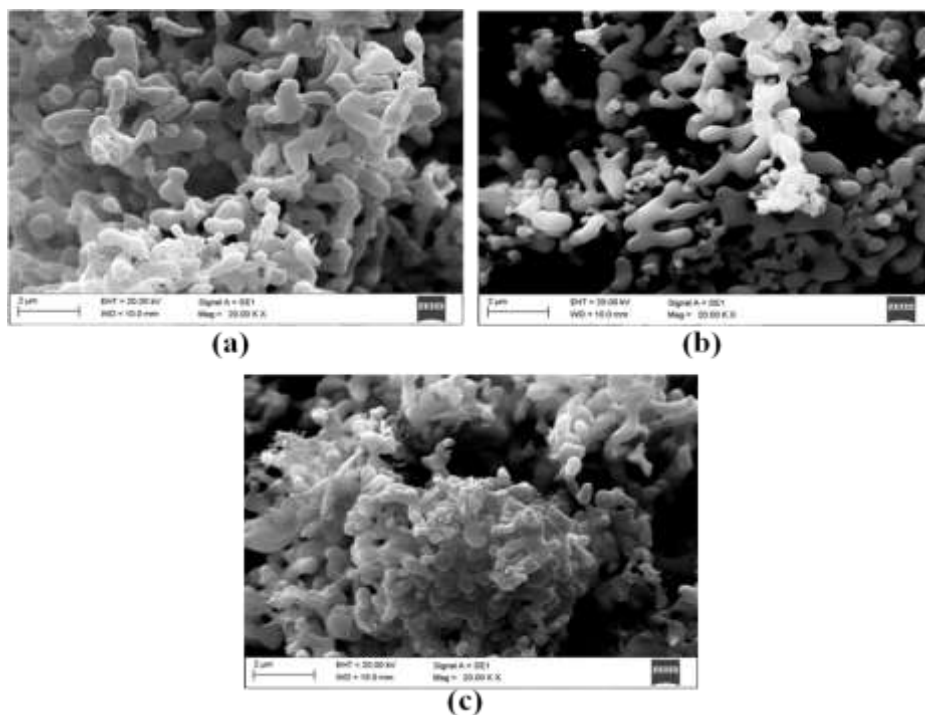


Fig. 4.56 SEM images of (a) $\text{Ca}_3\text{V}_2\text{O}_8$ (b) $\text{Sr}_3\text{V}_2\text{O}_8$ and (c) $\text{Ba}_3\text{V}_2\text{O}_8$

Fig. 4.56 (a) (b) and (c) display the SEM images of alkaline earth metal vanadates. As can be seen from the images, all the three composition showed similar morphology which is agglomerated and flake like. Out of the three compositions, $\text{Ca}_3\text{V}_2\text{O}_8$ showed lesser agglomeration as compared to $\text{Sr}_3\text{V}_2\text{O}_8$ and $\text{Ba}_3\text{V}_2\text{O}_8$, in which more conjointed particles were seen indicative of diffusion and sintering of the particles.

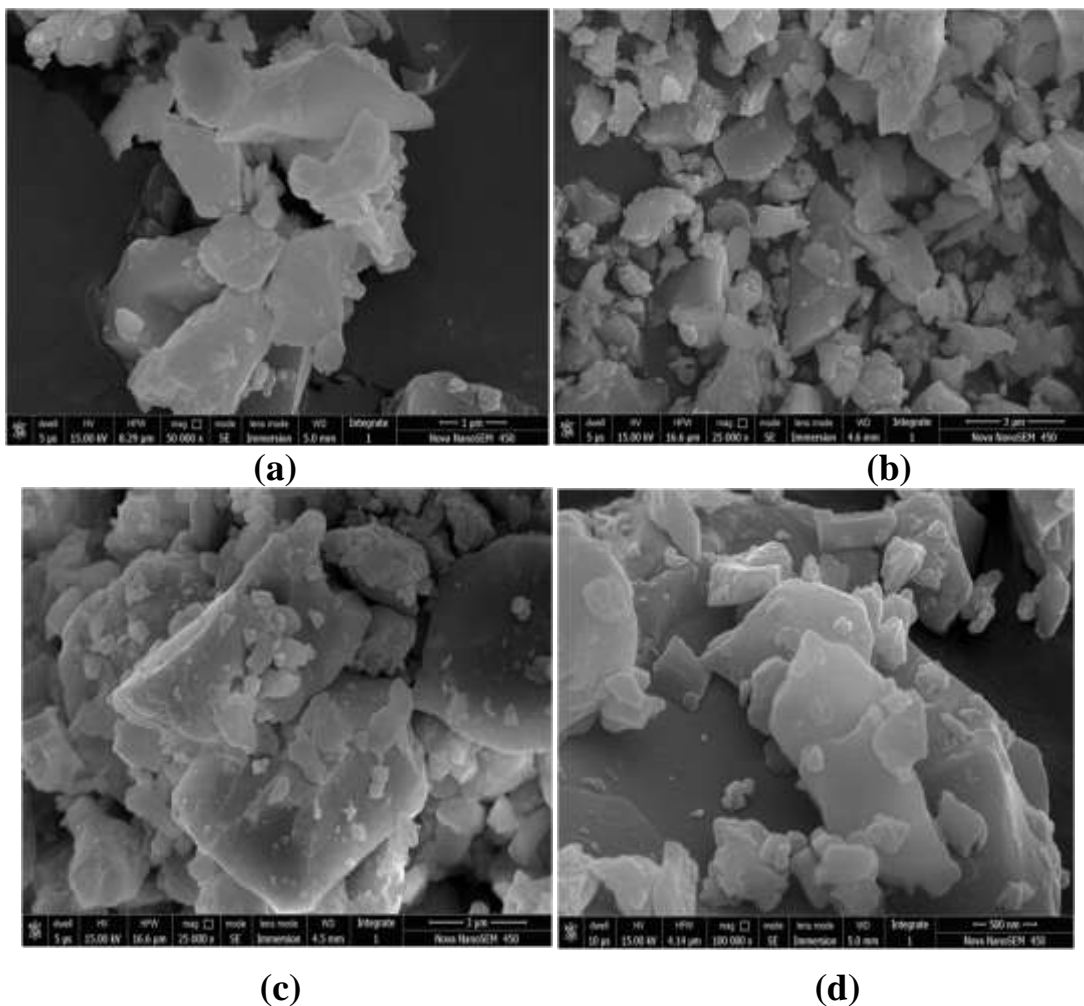


Fig. 4.57 SEM images of (a) $\text{Ca}_{2.94}\text{Tb}_{0.04}\text{V}_2\text{O}_8$, (b) $\text{Ca}_{2.92}\text{Tb}_{0.04}\text{Na}_{0.04}\text{V}_2\text{O}_8$, (c) $\text{Ca}_{2.88}\text{Ce}_{0.04}\text{Tb}_{0.04}\text{V}_2\text{O}_8$ and (d) $\text{Ca}_{2.39}\text{Pb}_{0.4}\text{Tb}_{0.08}\text{Eu}_{0.06}\text{V}_2\text{O}_8$

SEM images of representative samples from each phosphor series are presented in the Fig. 4.57(a)-(d). As can be seen from the images above, all the samples were found to be well sintered and compact. The compact nature of the materials confirmed that the treatment at 1000 °C in the form of pellet initiated a very facile sintering. All

the samples showed comparable texture in the morphology. The morphological features were found to be fairly consistent throughout the images. The apparent dense and compact form of the material seems to keep no room for porosity which is detrimental to the luminescence properties of the phosphor. In totality, dense materials with no signs of porosity were obtained with the preparative procedure used.

4.8 TEM studies

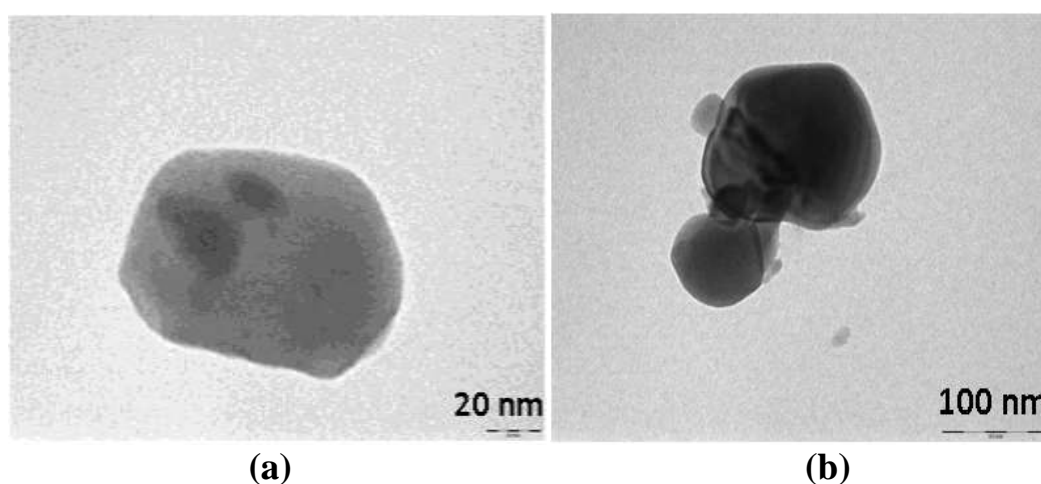


Fig. 4.58 Presents the TEM images of 2% Cu/Bi₂Mo₃O₁₂.

As observed from the images above the two types of particles were seen. The bigger particles can be said to be of Bi₂Mo₃O₁₂ as SEM images already have showed the agglomerated morphology whereas the small particles seen adhering to the catalyst surface are of supported CuO particles. The images indicate very good support-substrate interactions.

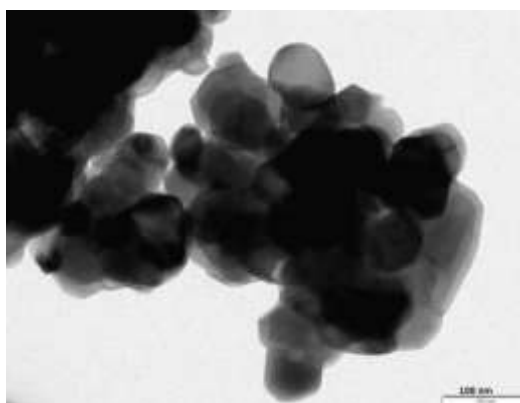


Fig. 4.59 TEM image of Bi₄V_{1.8}Cu_{0.2}O₁₁

Fig. 4.59 presents a representative TEM image from $\text{Bi}_4\text{V}_{2-x}\text{Cu}_x\text{O}_{11}$ series. The particle size was found to be in the range of 60- 70 nm with the spherical morphology and agglomeration.

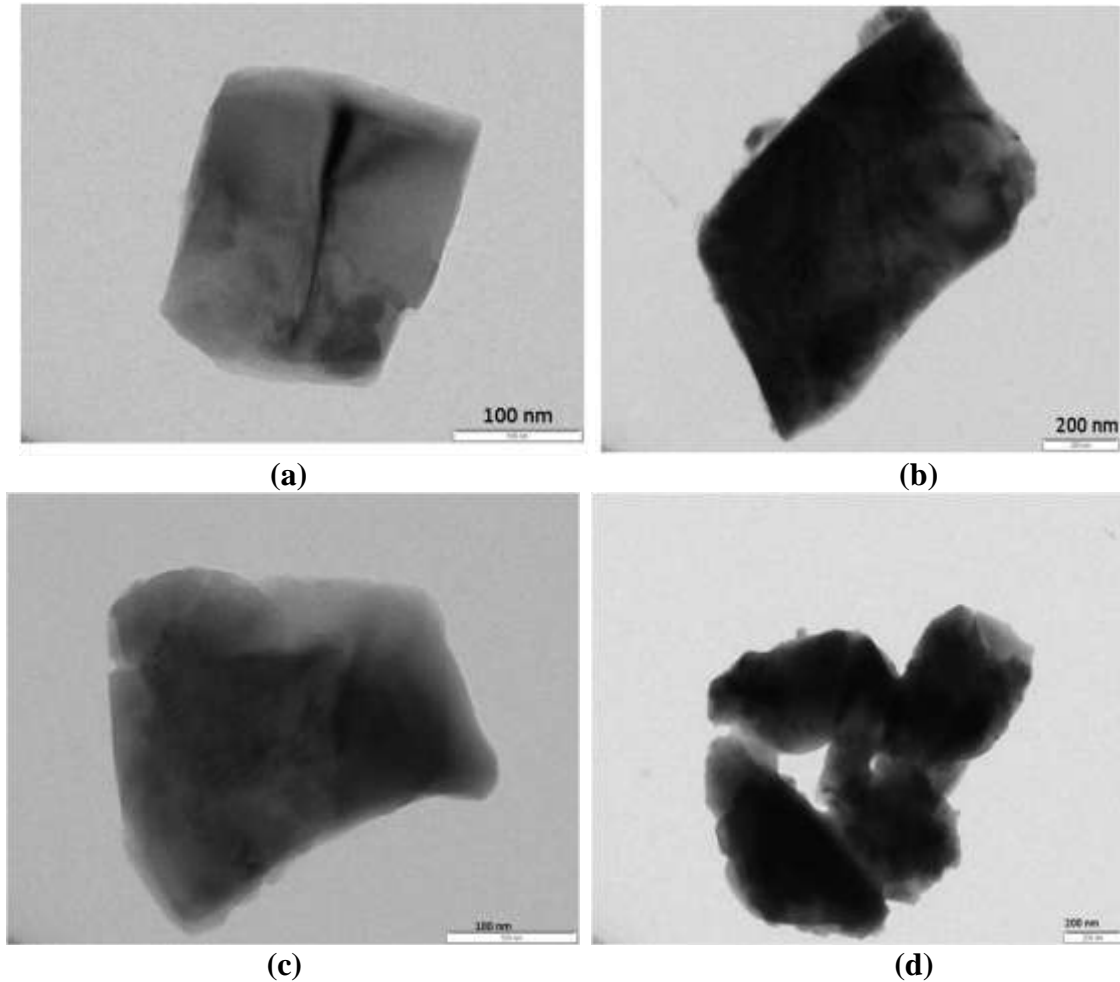


Fig. 4.60 TEM images of (a) $\text{Ca}_{2.94}\text{Tb}_{0.04}\text{V}_2\text{O}_8$, (b) $\text{Ca}_{2.92}\text{Tb}_{0.04}\text{Na}_{0.04}\text{V}_2\text{O}_8$, (c) $\text{Ca}_{2.39}\text{Pb}_{0.4}\text{Tb}_{0.08}\text{Eu}_{0.06}\text{V}_2\text{O}_8$ (d) $\text{Ca}_{2.88}\text{Ce}_{0.04}\text{Tb}_{0.04}\text{V}_2\text{O}_8$

The above figures from 4.60 (a)-(b) represent the TEM images of representative samples from each phosphor series. As evident from the images the particles size of the material can be located in micron range which is in accordance with the SEM studies discussed earlier. The particle size of the materials is found to be in the range of 0.5 to 1 μm . The Tb and Na-Tb co-doped sample showed loosely rhomboidal particle shapes. The Ce-Tb co-doped sample showed a trapezoidal shape. Whereas the Eu-Tb co-doped showed irregular shapes of the particles.

4.9 Luminescence studies

4.9.1 $\text{Ca}_{3-3x/2}\text{Tb}_x\text{V}_2\text{O}_8$ and $\text{Ca}_{3-2x}\text{Tb}_x\text{Na}_x\text{V}_2\text{O}_8$ series

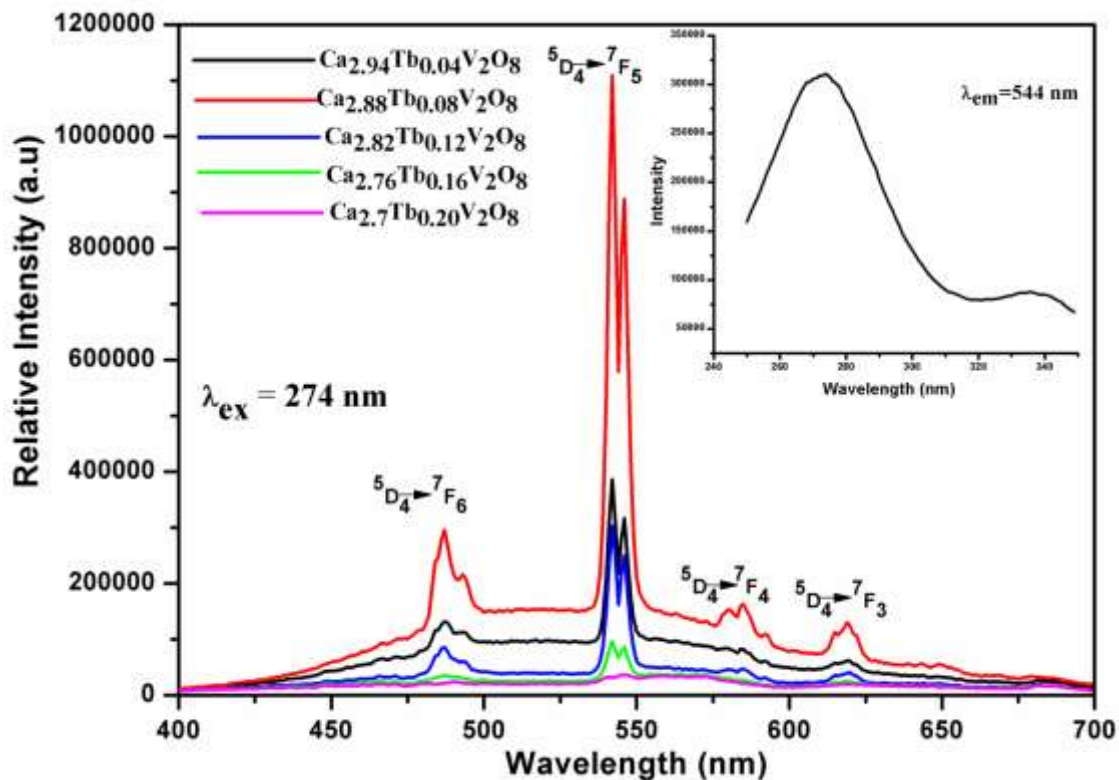


Fig. 4.61 Emission spectra of $\text{Ca}_{3-3x/2}\text{Tb}_x\text{V}_2\text{O}_8$ excited at 274 nm, Inset shows excitation spectrum monitored at 544 nm for $\text{Ca}_{2.88}\text{Tb}_{0.08}\text{V}_2\text{O}_8$

The inset of the above Fig. 4.61, shows the excitation spectrum of the composition $\text{Ca}_{2.88}\text{Tb}_{0.08}\text{V}_2\text{O}_8$, monitored at 544 nm. 544 nm is considered as a main green emission of Tb ions. As can be noticed from the spectrum, the maximum of the excitation spectrum was located at around 274 nm. The obtained excitation spectrum is in good accordance with the absorbance spectra of the phosphors discussed in the earlier section of UV-DRS studies. The excitation of Tb is considered to be mainly due to the $4f^8 \longrightarrow 4f^7 5d^1$ transition [266]. Tetrahedral VO_4^{3-} moieties are known to show the charge transfer in and around the same region and are also known to sensitize the rare earth ions [267]. Therefore, it can be concluded that the obtained excitation spectrum to be the admixture of both the above-discussed transitions. Taking into

consideration the excitation spectrum, all the Tb singly doped compositions were excited at 274 nm.

The emission spectra of Tb singly doped phosphors excited at 274 nm are displayed in Fig. 4.61. The major green emission was centred at 544 nm which corresponds to the $^5D_4-^7F_5$ transition. This transition was accompanied by less pronounced blue emission at 489 nm, yellow emission at 580 nm and red emission at 618 nm. All these emissions can be assigned to $5D_4-^7F_6$, $5D_4-^7F_4$ and $5D_4-^7F_3$ transitions respectively. Another set of emissions, that are characteristics of Tb arise from $5D_3-^7F_J$ ($J = 3-6$) transitions. These emissions must be very weak as they were not seen clearly in the emission pattern. The major green emission observed at 544 nm split into two nearby components and can be attributed to the stark effect in the crystal lattice [278]. The emission intensity was found to increase with the increase in Tb concentration up to $Tb = 0.08$. The composition with $Tb = 0.08$ showed intense green emission but the emission intensity of subsequent compositions started to dwindle down. The lowering of emission intensity after $Tb = 0.08$ can be attributed partly to the concentration quenching. In the concentration quenching, after an optimum concentration, the energy is transferred from one ion to another in a serial manner. This leads to the loss of energy through non-radiative processes ultimately leading to the weak emissions. This phenomenon is characteristic of activator rare earth ions. As Tb^{3+} ions are doped in the $Ca_3V_2O_8$ crystal lattice, to maintain electroneutrality three Ca^{2+} ions make a place for two Tb^{3+} ions, and as the doping concentrations increase in the lattice the number of vacancies also increase. The generated vacancies in the crystal lattice are known to have a detrimental effect on the emission intensities as these cation vacancies can affect the local electronic environment. The cation vacancies can also

provide the routes for non-radiative relaxation processes and quenching that leads to an overall decrease in the emission intensity [220, 228, 242].

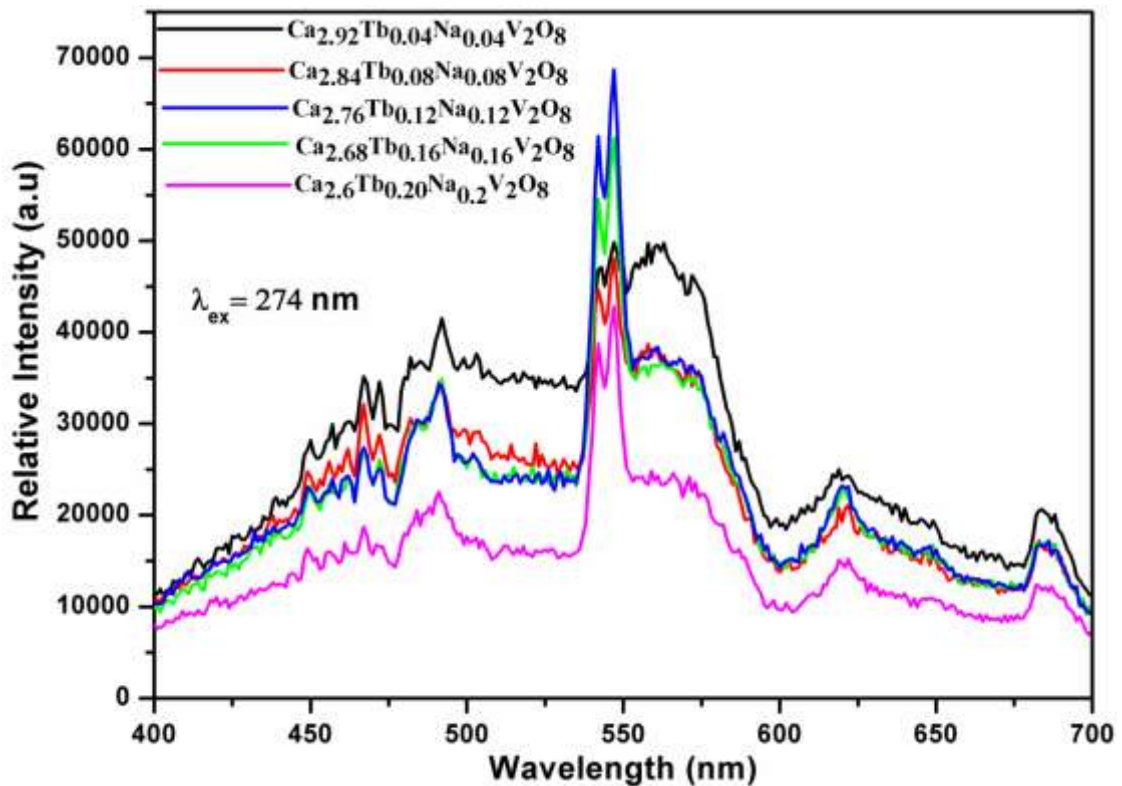


Fig 4.62 Emission spectra of $Ca_{3-2x}Tb_xNa_xV_2O_8$ excited at 274 nm

The Na-Tb co-doped phosphors were excited at 274 nm. The spectra are presented in the Fig. 4.62. One can see from the Fig. 4.62 that the prominent green emission was maintained in all the compositions. But the overall intensity of the emissions decreased drastically with the difference also seen in the emission pattern of the phosphors. Although the emission intensities and the pattern changed, the positions of the emission lines did not change. This observation indicates the change in the local structure around the emission centres. This might have arisen due to the change in the electronic environment brought about by the Na co-doping. The change in local structure and the electronic environment has made the phosphors less receptive towards the excitation wavelength of 274 nm. Thus a change in sensitizing mechanism could be predicted.

The excitation spectra of Na-Tb co-doped samples were recorded by monitoring the emission at 544 nm. The excitation spectrum of $\text{Ca}_{2.76}\text{Tb}_{0.12}\text{Na}_{0.12}\text{V}_2\text{O}_8$ is displayed in Fig. 4.63 (inset). The excitation maximum, in this case, was located at 320 nm.

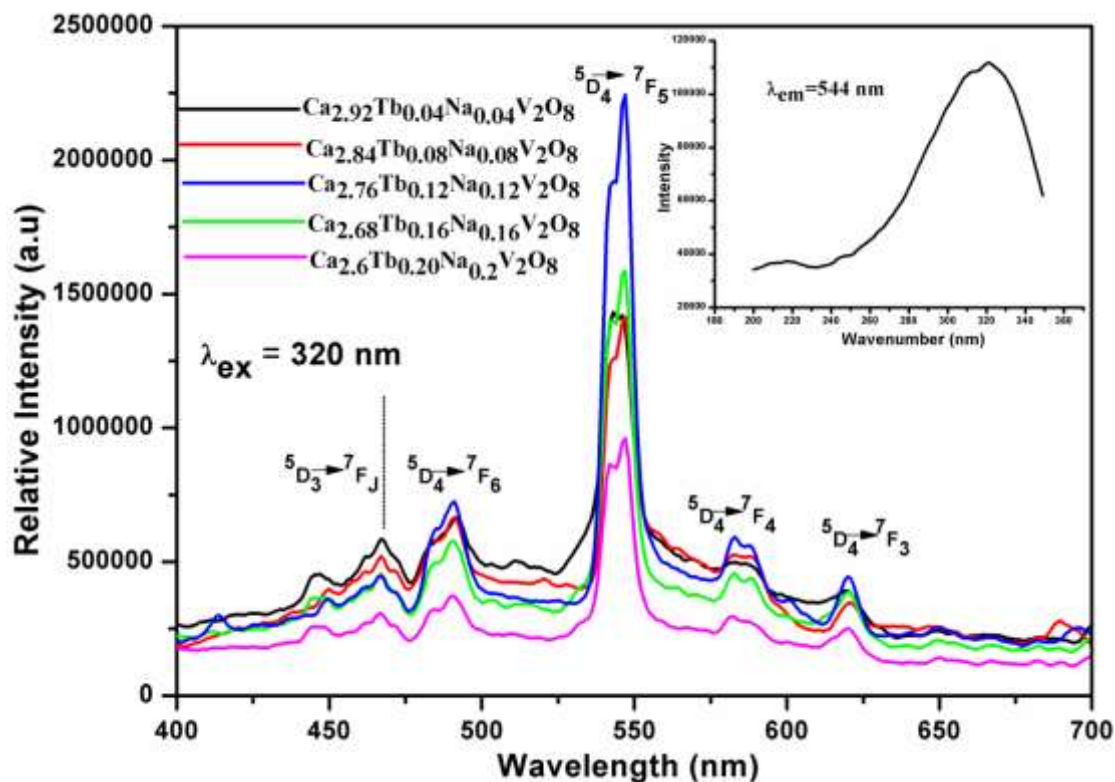


Fig. 4.63 Emission spectra of $\text{Ca}_{3-2x}\text{Tb}_x\text{Na}_x\text{V}_2\text{O}_8$ excited at 320 nm, Inset shows excitation spectrum monitored at 544 nm for $\text{Ca}_{2.76}\text{Tb}_{0.12}\text{Na}_{0.12}\text{V}_2\text{O}_8$

The emission spectra of co-doped phosphors excited at 320 nm are given in Fig. 4.63. The resolution of emission peaks, in this case, was distinct as compared to the Tb singly doped compounds. The splitting of emission at 544 nm due to Stark effect was observed to a very less extent as compared to Tb singly doped compositions. The absence of cation vacancies have minimised the local disorder considerably in Na-Tb co-doped compositions as observed and discussed previously in the context of Raman spectra. This has led to the formation of well separated and demarcated energy. The optimum concentration of Tb, in this case, was found to be $\text{Tb} = 0.12$, after which the luminescence intensity followed the usual decline. But the decrease in luminescence intensity was not as extreme as observed in the singly doped series. The loss of

luminescence after $Tb = 0.12$ is mainly due to the typical concentration quenching of rare earth ions. In the co-doped series, it can be proposed that the homo ion interactions of the Tb^{3+} ions are lowered. These homo ion interactions when present are responsible for the serial transfer of energy from one ion to the next leading to the loss of energy due to non-radiative processes and thermal dissipation. Therefore, Na doping not only controlled the effects caused due to the vacancies but also minimised the homo ion interactions to a considerable extent. This has resulted in sustained luminescence even after the optimum doping concentration [279].

4.9.2 $Ca_{2.94-3x/2}Ce_{0.04}Tb_xV_2O_8$ series

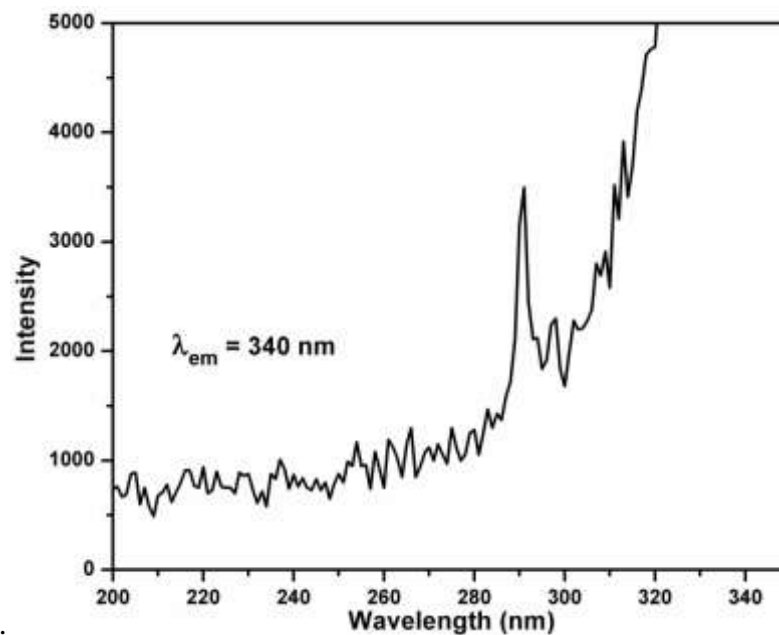


Fig. 4.64 Excitation spectrum of $Ca_{2.94}Ce_{0.04}V_2O_8$ monitored at 340 nm.

The Fig. 4.64 presents the excitation spectrum of $Ca_{2.94}Ce_{0.04}V_2O_8$ monitored at 340 nm. To investigate the excitation wavelength for Ce^{3+} emission, the excitation was monitored at 340 nm as it is known that the major emission of Ce takes place in the range between 340-390 nm. As the above spectrum reveals, the excitation peak was located at 290 nm which can be attributed to the $4f-5d$ transition of Ce [266].

Further, to investigate the Tb excitation in the Ce-Tb co-doped compositions, the excitation spectrum for the composition $\text{Ca}_{2.88}\text{Ce}_{0.04}\text{Tb}_{0.04}\text{V}_2\text{O}_8$ was run by monitoring the green emission of Tb at 547 nm. The resultant excitation spectrum is presented in the Fig. 4.65. As evident from the figure that there is an intense peak centred at 270 nm. Beside this peak, there is a less intense hump covering the area from 300-340 nm. The excitation peak can be attributed to the $4f - 5d$ transition of the Tb^{3+} ion, which constitutes most of its excitation. The slight hump observed after the peak could not be attributed to any systematic transition.

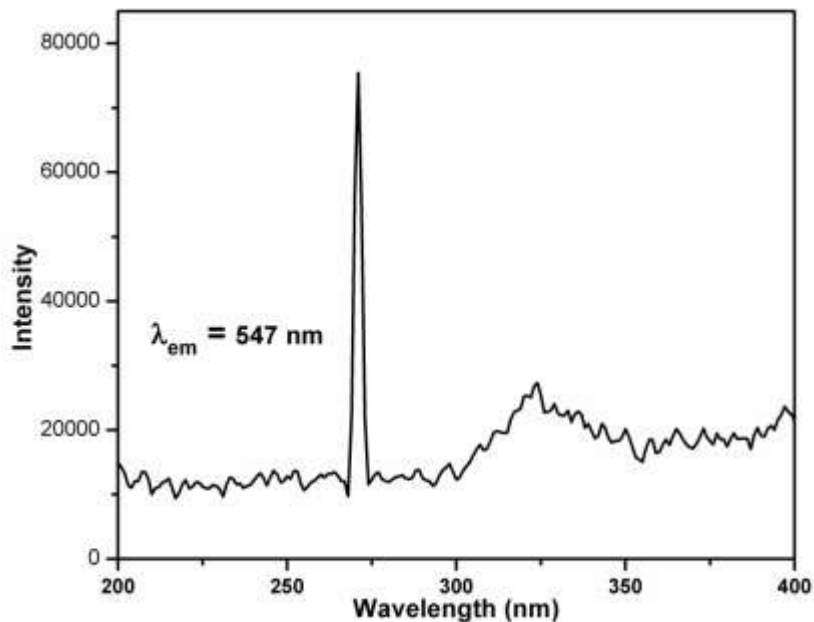


Fig. 4.65 Excitation spectra of $\text{Ca}_{2.88}\text{Ce}_{0.04}\text{Tb}_{0.04}\text{V}_2\text{O}_8$ monitored at 547 nm

Ce^{3+} ion is known to be a very good sensitizer ion to the rare earth ions. Especially, the Ce-Tb combinations have been studied for their energy transfer and white light applications. The composition $\text{Ca}_{2.88}\text{Ce}_{0.04}\text{Tb}_{0.04}\text{V}_2\text{O}_8$ was excited at 290 nm. The emission spectrum is presented in the Fig. 4.66. The spectrum shows a sharp emission peak at 340 nm followed by a broad hump up to 450 nm. These both emissions can be associated with the Ce $5d - 4f$ relaxations.

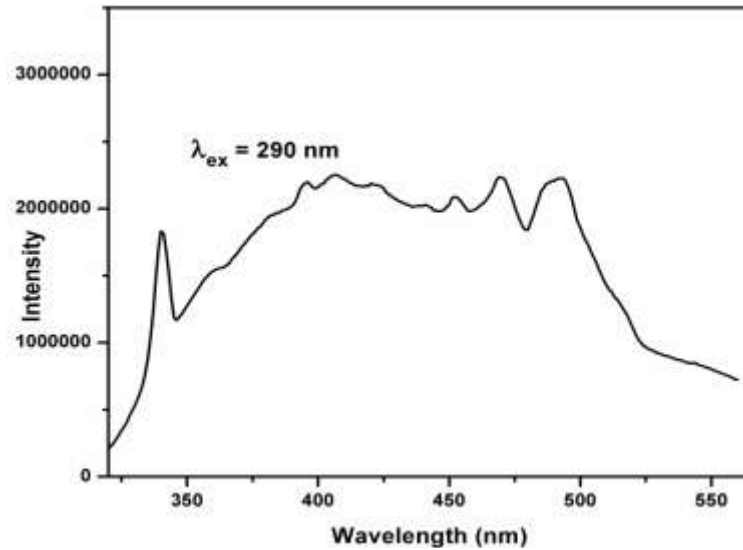


Fig. 4.66 Emission spectrum of $\text{Ca}_{2.88}\text{Ce}_{0.04}\text{Tb}_{0.04}\text{V}_2\text{O}_8$ excited at 290 nm.

The emission peaks observed after 450 nm up to 500 nm are the Tb emissions from $^5\text{D}_3$ - $^7\text{F}_J$ ($J=3-6$) and initial $^5\text{D}_3$ - $^7\text{F}_4$ transition which is observed at around 500 nm. Apart from this, the major green emission of Tb observed at 547 nm was not observed. Therefore, it can be said that the excitation at 290 nm has not excited the Tb^{3+} centres responsible for the green emission. Later, all the compositions were excited at 270 nm. The emission spectra are presented in Fig. 4.67

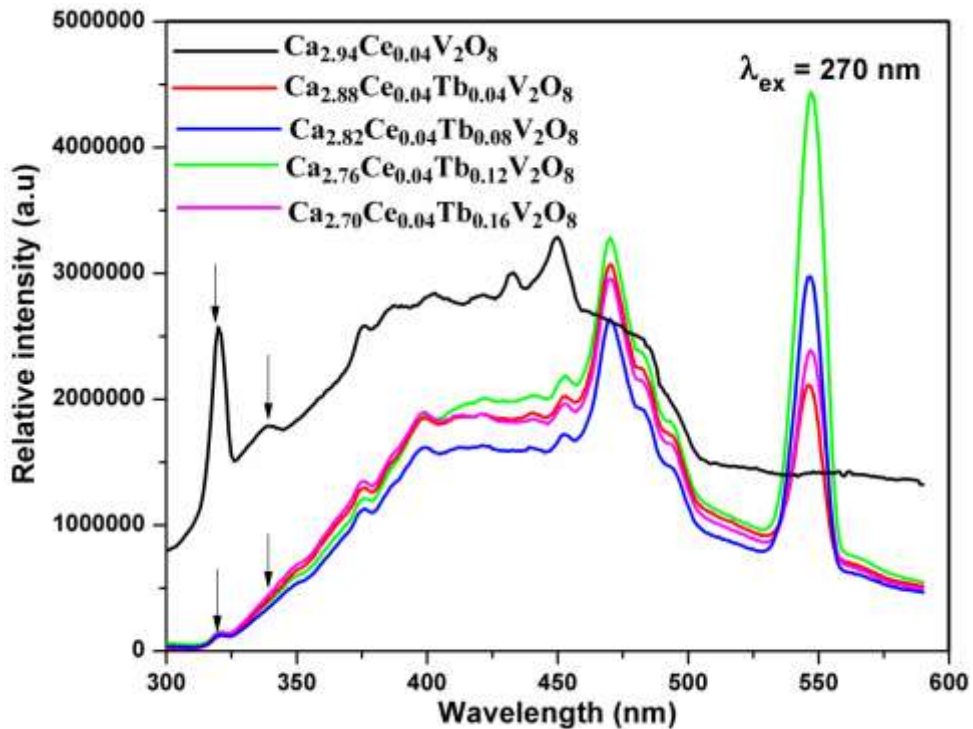


Fig. 4.67 Emission spectra of $\text{Ca}_{2.94-3x/2}\text{Ce}_{0.04}\text{Tb}_x\text{V}_2\text{O}_8$ compositions

As observed from the figure, all the Tb containing compositions showed the intense green emission at around 547 nm. The first composition of the series (Ce singly doped) showed a peak at 320 nm with a small hump at around 340 nm. This is succeeded by the broad emission up to 450 nm. An interesting observation that can be made from the spectra is that the intensity of the peak at 320 nm found in case of Ce doped sample is significantly lowered in case of Tb doped samples. Also, the peak at 340 nm has nearly vanished. It was observed earlier in the case of the excitation spectrum for the Tb emission, that a small hump was spanning the area between 320-340 nm. Also in our studies on Tb singly doped compounds (discussed in section 4.9.1) we found a similar hump after the major excitation peak centred at 274 nm. This just might suggest that the Tb ions in $\text{Ca}_3\text{V}_2\text{O}_8$ might have this section of wavelength associated with their excitation. In the present case, the initial emissions of Ce relating to the Ce $5d-4f$ transitions are found to be in the region of 320-340 nm. The decrease in their intensities after the introduction of Tb, therefore, suggests an energy transfer from Ce to Tb. The exact effect of this energy transfer on the emission intensities, that is the quantification of Tb emission intensities due to the energy transfer from Ce was difficult to decipher from the type of spectra observed in this case. Nevertheless, the highest green emission intensity was observed in case of Tb = 0.12, with further increase in Tb, the intensity decreased mainly because of concentration quenching brought about by increasing homo-ion interactions. The lowest emission intensity was found for the composition with Tb = 0.04.

4.9.3 $\text{Ca}_{2.48-3x/2}\text{Pb}_{0.4}\text{Tb}_{0.08}\text{Eu}_x\text{V}_2\text{O}_8$ series

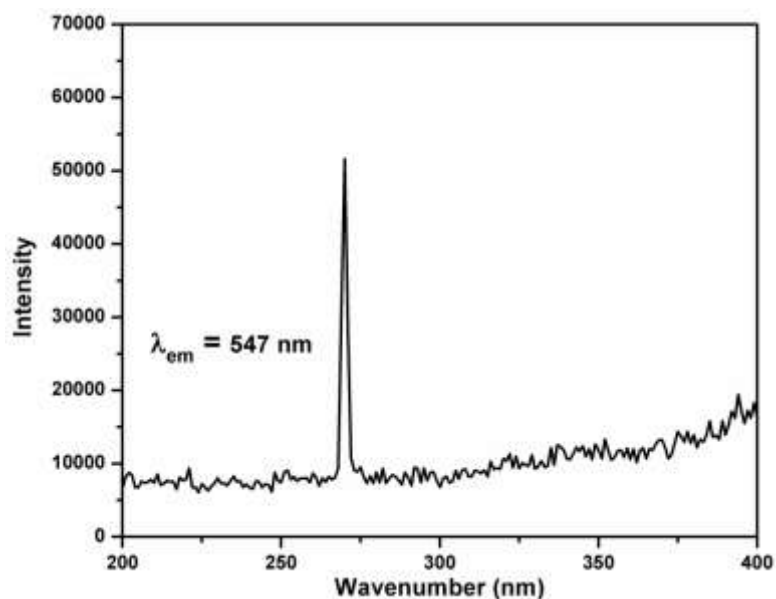


Fig. 4.68 Excitation spectrum of monitored at 547 nm.

The excitation spectrum of the composition, $\text{Ca}_{2.36}\text{Pb}_{0.4}\text{Tb}_{0.08}\text{Eu}_{0.08}\text{V}_2\text{O}_8$ monitored for the green emission is presented in the Fig. 4.68. The excitation spectrum is centred on 270 nm and is attributed to the Tb 4*d*-5*f* transitions. The excitation spectrum for the same composition monitored for the red emission of Eu at 615 nm is presented in the Fig. 4.69. The well-defined excitation pattern is the characteristic of the Eu^{3+} ion [237]. As can be seen from the spectra the excitation wavelengths mainly were found in the region higher than 300 nm.

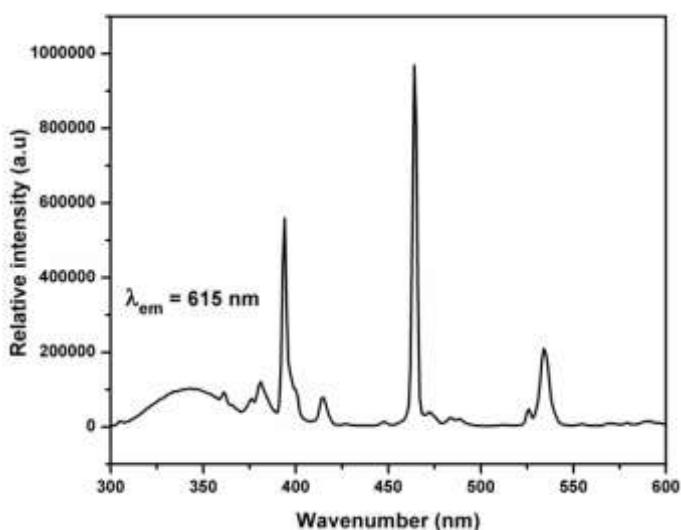


Fig. 4.69 Excitation spectrum of $\text{Ca}_{2.36}\text{Pb}_{0.4}\text{Tb}_{0.08}\text{Eu}_{0.08}\text{V}_2\text{O}_8$

The excitation peak observed at around 540 nm is attributed to ${}^7F_1-{}^5D_1$ transition. The most intense peak observed at around 465 nm is associated with the ${}^7F_0-{}^5F_2$ transition whereas, the peak observed at 420 nm and 400 nm are attributed to ${}^7F_1-{}^5D_3$ and ${}^7F_0-{}^5L_6$ transitions respectively [237].

A wavelength nearer to excitation wavelengths of both Eu and Tb was tentatively chosen so as to see if the simultaneous excitation of both ions was possible. Therefore, the wavelength of 304 nm was used to excite. The wavelength 304 nm was chosen as Eu has shown the excitation hump in this region as seen from the Fig. 4.69 and also it was nearer to the excitation wavelength region of Tb which generally falls in 270- 320 nm [272]. The emission spectra of all the compositions excited at 304 nm are presented in the Fig. 4.70.

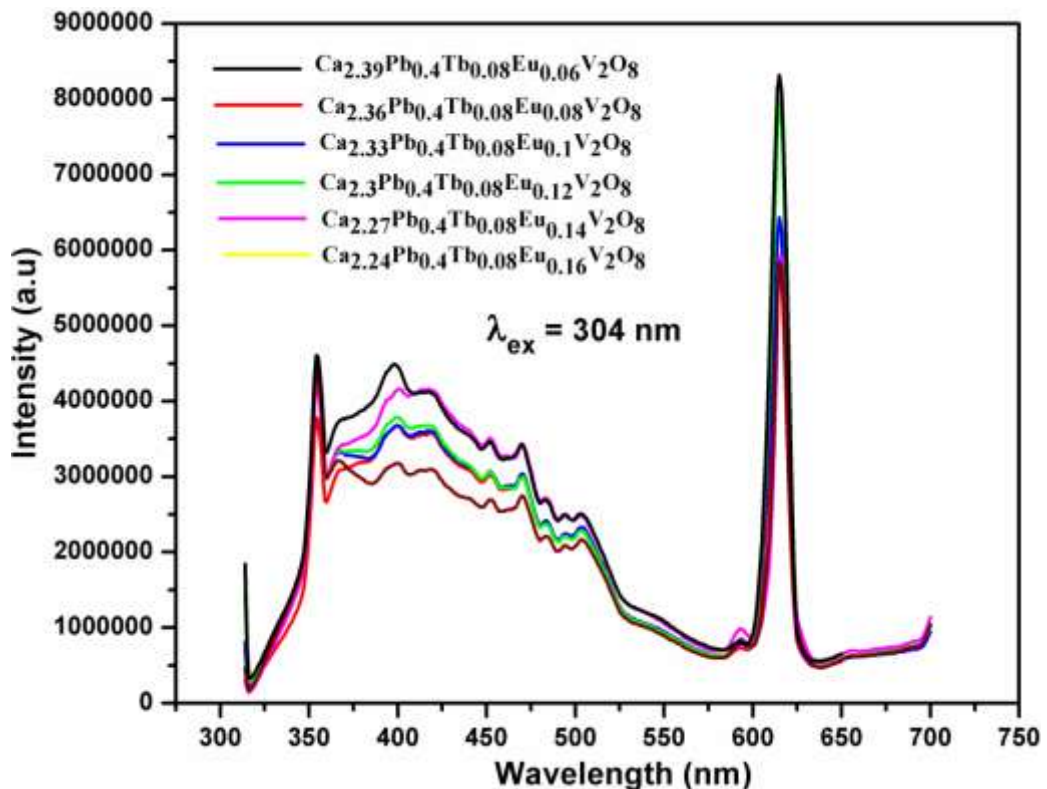


Fig. 4.70 Emission spectra of $Ca_{2.48-3x/2}Pb_{0.4}Tb_{0.08}Eu_xV_2O_8$ series.

As observed from the figure, the emission spectra show initial emissions from 350 to 500 nm which can be attributed to the mixture of Pb^{2+} and host emissions. The

intense emission at 614 nm was seen but no sign of green emission of Tb was seen. This proves that the excitation wavelength applicable to Eu cannot excite the Tb emissions thus a simultaneous red and green emission could not be achieved. Fig. 4.71 presents the emission spectra of series excited at 270 nm.

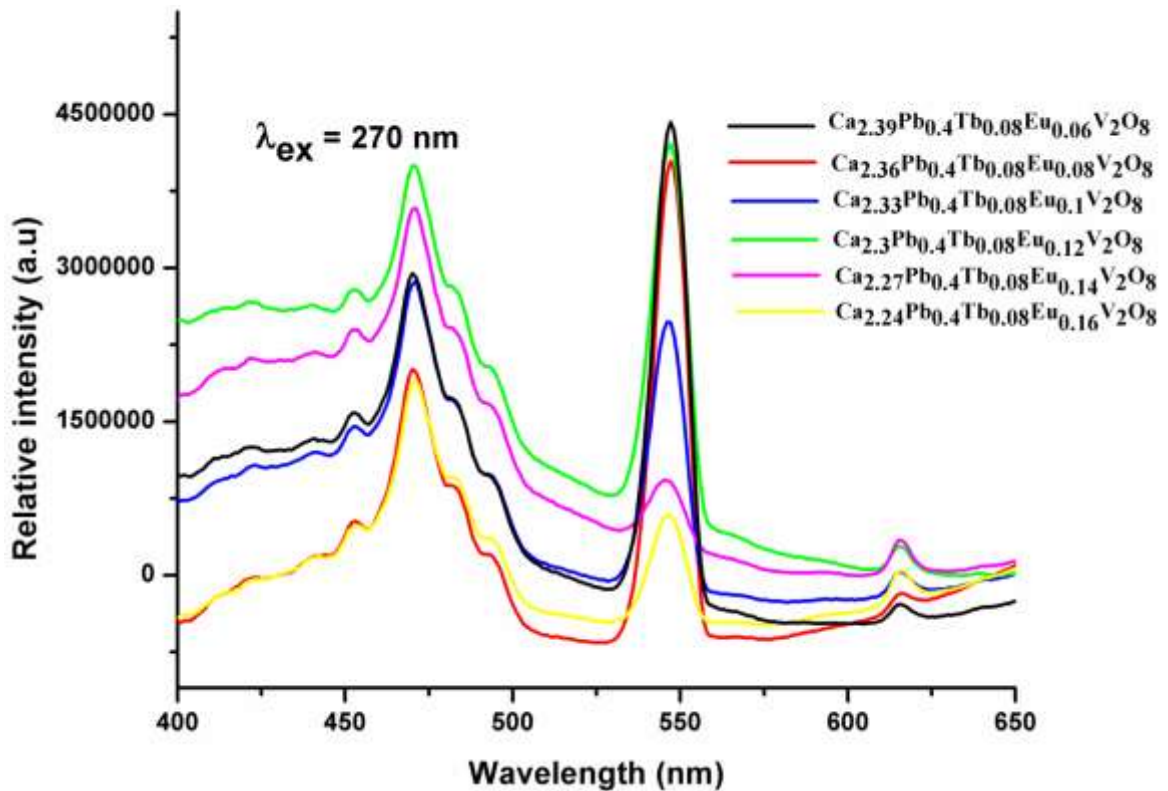


Fig. 4.71 Emission spectra of $\text{Ca}_{2.48-3x/2}\text{Pb}_{0.4}\text{Tb}_{0.08}\text{Eu}_x\text{V}_2\text{O}_8$ series excited at 270 nm.

From the figure it can be observed that along with the routine emission of Tb, the major emission peak of Eu, which is the red emission, has shown its existence at around 615 nm. Although the emissions are weaker than the green emissions their existence on the excitation wavelength of 270 nm is significant as the well-defined define excitation spectrum Eu^{3+} had all the excitation peaks above 300 nm. Therefore, it suggests an energy transfer from Tb to Eu as it is the only option by which the Eu can emit its characteristic emission. Unfortunately, due to the instrumental limitation, the spectra obtained is not of the finest quality and therefore the Tb and Eu excitation

wavelengths could not be linked accurately. As one can observe from the spectra the emission pattern contains the emissions at 480 nm (blue), 547 nm (green) and 645 nm (red), which are the basic components of the white light therefore it can be said that the compositions can prove to be the potential candidates for the white light emissions

5. CATALYTIC STUDIES

This chapter presents the catalytic studies conducted over the prepared catalysts. BET surface area measurements of all the catalysts are given. An account of the partial oxidation of propene to acrolein is presented. The conversion of propene and selectivity towards acrolein with respect to the temperature are reported. The product distributions, at the highest conversion temperature or at the temperature where the catalysts show highest selectivity towards acrolein are presented in the tabular form. Finally, the catalytic activity of the catalysts is discussed.

5.1 BET Surface area measurements.

Surface area is an important characteristic property of any heterogeneous catalyst system. The measurement of the surface area of the catalyst indicates the exposure of the active catalytic sites to the incoming gaseous reactants, thus it is considered an important measure to evaluate the catalytic activity. It is also a well-known fact that the surface area is not the only parameter on which the performance of the catalysts depends. Along with the surface area, local structure and composition of the surface active sites also play an important part especially in the case of reactions such as partial oxidation of hydrocarbons. The BET surface area measurements of all the catalytic systems prepared are presented in Table 5.1.

Table 5.1. BET Surface area of the prepared compositions.

Sr. No.	Compositions	Surface area (m ² /g)
Cu/Bi₂Mo₃O₁₂		
1.	Bi ₂ Mo ₃ O ₁₂	2.6
2.	2% Cu/Bi ₂ Mo ₃ O ₁₂	2.5

3.	4% Cu/Bi ₂ Mo ₃ O ₁₂	2.5
4.	8% Cu/Bi ₂ Mo ₃ O ₁₂	2.4
Bi₄V_{2-x}Cu_xO₁₁		
5.	Bi ₄ V ₂ O ₁₁	16.8
6.	Bi ₄ V _{1.9} Cu _{0.1} O ₁₁	15.2
7.	Bi ₄ V _{1.8} Cu _{0.2} O ₁₁	14.8
8.	Bi ₄ V _{1.7} Cu _{0.3} O ₁₁	14.1
9.	Bi ₄ V _{1.6} Cu _{0.4} O ₁₁	12.8
Cu_xV_{1-x}SbO₄		
10.	VSbO ₄	29.0
11.	Cu _{0.05} V _{0.95} SbO ₄	27.1
12.	Cu _{0.1} V _{0.9} SbO ₄	26.4
13.	Cu _{0.2} V _{0.8} SbO ₄	25.3
14.	Cu _{0.3} V _{0.7} SbO ₄	21.0
Cu-K-V-Sb-O		
15.	Cu _{0.05} K _{0.02} V _{0.95} Sb _{0.98} O _x	32.3
16.	Cu _{0.1} K _{0.05} V _{0.9} Sb _{0.95} O _x	35.7
17.	Cu _{0.2} K _{0.1} V _{0.8} Sb _{0.90} O _x	37.8
18.	Cu _{0.3} K _{0.15} V _{0.7} Sb _{0.85} O _x	41.2
Bi₂Mo_{1-x}W_xO₆		
19.	Bi ₂ MoO ₆	2.0
20.	Bi ₂ Mo _{0.8} W _{0.2} O ₆	2.6
21.	Bi ₂ Mo _{0.6} W _{0.4} O ₆	2.3

M₃V₂O₈ (M = Ca, Sr and Ba)		
22.	Ca ₃ V ₂ O ₈	48.3
23.	Sr ₃ V ₂ O ₈	36.8
24.	Ba ₃ V ₂ O ₈	34.0

The BET surface area of both the Bi-Mo containing compositions i.e. Cu/Bi₂Mo₃O₁₂ and Bi₂Mo_{1-x}W_xO₆ was found to be in the range of 2- 3 m²/g. The range of BET surface area obtained is known to be the characteristic of Bismuth molybdate phases prepared by conventional methods such as co-precipitation and sol-gel. In case of the Cu/Bi₂Mo₃O₁₂ compositions, a negligible decrease in the surface area was observed after the Cu loadings. Surface area values in case of W doped Bi₂MoO₆ series did not show a trend as such but the W doped compositions showed slightly higher surface area than pristine Bi₂MoO₆.

The Cu inserted Bi₄V₂O₁₁ compositions showed the surface area values in the range of 12-17 m²/g. The surface area gradually decreased on the inclusion of copper in the crystal lattice. This decrease is also reflective of the increase in crystallite size observed after the Cu inclusion as deduced from the X-ray diffraction studies.

The Cu doped VSbO₄ compositions showed the surface area in the range of 21- 29 m²/g whereas the composite catalysts Cu-K-V-Sb-O showed the surface area in the range of 32- 41 m²/g. The higher surface area values in case of composite catalysts as compared to the Cu doped VSbO₄ series can be due to the presence of different mixed phases in the composite. Similarly, the increase in surface area within the composite compositions can be due to the increase in these constituent phases. The surface area values obtained for the alkaline earth metal vanadates were in the range of 34- 48 m²/g.

The $\text{Ca}_3\text{V}_2\text{O}_8$ showed the highest surface area whereas $\text{Ba}_3\text{V}_2\text{O}_8$ showed the lowest surface area among the alkaline earth metal vanadates.

5.2 Partial oxidation of Propene

All the results regarding partial oxidation of propene are compiled in the following sections.

5.2.1 $\text{Cu}/\text{Bi}_2\text{Mo}_3\text{O}_{12}$ catalysts

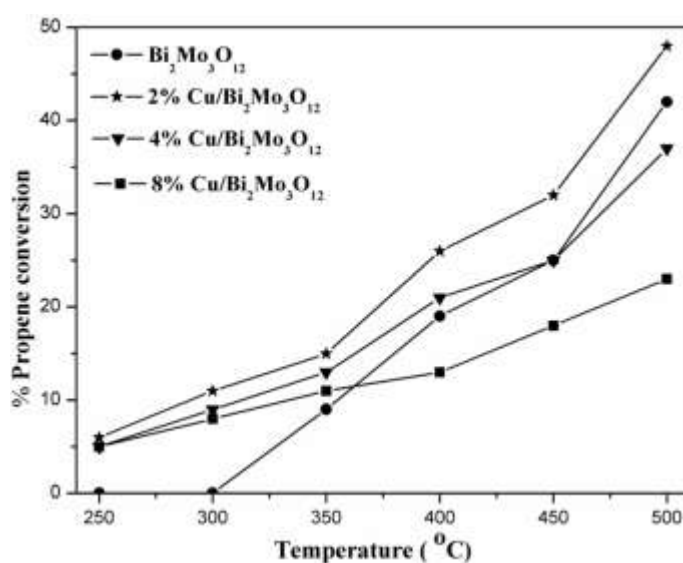


Fig. 5.1 Partial oxidation of Propene over $\text{Cu}/\text{Bi}_2\text{Mo}_3\text{O}_{12}$ catalysts.

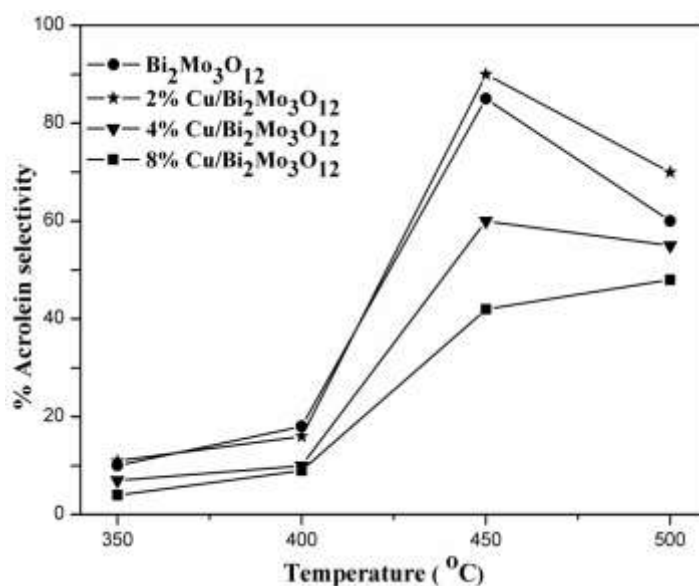


Fig. 5.2 Acrolein selectivity profile of $\text{Cu}/\text{Bi}_2\text{Mo}_3\text{O}_{12}$ catalysts.

Fig. 5.1 displays the conversion of propene and the Fig. 5.2 presents the selectivity towards the production of acrolein. Conversion of propene increased with the temperature. The significant yield of oxygenated products over pristine $\text{Bi}_2\text{Mo}_3\text{O}_{12}$ started from 300 °C. The $\text{Cu}/\text{Bi}_2\text{Mo}_3\text{O}_{12}$ catalysts showed the conversion of propene as early as 250 °C. Though the yield of oxygenated products at 250 °C was less, it showed the striking difference from the pristine $\text{Bi}_2\text{Mo}_3\text{O}_{12}$ catalysts. Bismuth molybdates catalysts are known to supply the oxygen to the substrates from the lattice. The oxygen mobility in the catalysts needs a sufficient thermal appeasement which is not possible at the lower temperatures and hence the significant catalytic activities of monophasic Bismuth molybdates are reported only after 350 °C. In this particular case, it seems that the presence of copper over the active support $\text{Bi}_2\text{Mo}_3\text{O}_{12}$ has resulted in the redox activity at the lower temperatures which looks to be surface driven and not lattice driven. The catalysts with 2% and 4% Cu loadings showed better conversion than the pristine $\text{Bi}_2\text{Mo}_3\text{O}_{12}$ whereas the catalysts with 4% Cu loading showed lowest propene conversion.

From the Fig. 5.2, it can be noted that the selectivity profiles of $\text{Bi}_2\text{Mo}_3\text{O}_{12}$ and 2% $\text{Cu}/\text{Bi}_2\text{Mo}_3\text{O}_{12}$ catalysts towards acrolein were almost identical. At the temperature intervals of 450 °C and 500 °C, the 2% Cu loaded catalysts showed slightly higher selectivity towards the acrolein whereas the catalyst with the 8% Cu loading showed the lowest selectivity towards the acrolein.

Table 5.2. Product distribution of pristine and Cu/Bi₂Mo₃O₁₂ catalysts

Catalyst	Temperature (°C)	Propylene Conversion (%)	Selectivity (%)		
			Acrolein	Acetaldehyde	Carbon oxides
Bi ₂ Mo ₃ O ₁₂	450	25	85	5	5
	500	42	60	3	35
2% Cu / Bi ₂ Mo ₃ O ₁₂	450	32	90	6	4
	500	48	70	2	25
4% Cu / Bi ₂ Mo ₃ O ₁₂	450	25	60	4	32
	500	37	55	1	39
8% Cu / Bi ₂ Mo ₃ O ₁₂	450	18	42	3	40
	500	23	48	3	45

The product distribution over the catalysts at the temperature intervals of 450 °C and 500 °C is presented in Table 5.2. Acrolein selectivity was highest at 450 °C but lowered subsequently at 500 °C. This pattern was observed in all the catalysts. The formation of completely oxidized products, CO/CO₂ increased at this stage. A negligible production of acetaldehyde was also observed. The catalysts with the 4% and 8% Cu loadings showed the highest formation of carbon oxides.

From the above observation made regarding the catalytic activity measurements, it can, therefore, be said that the 2% Cu loadings have slightly improved the conversion and selectivity of pristine Bi₂Mo₃O₁₂ catalysts but the subsequent higher Cu loadings were detrimental towards obtaining the selectivity towards acrolein. 2% Cu loading showed better conversion than pristine Bi₂Mo₃O₁₂ whereas the 4% Cu loading showed the conversion in line with the pristine Bi₂Mo₃O₁₂. As the Cu loadings increased over the Bi₂Mo₃O₁₂ catalysts it can be speculated that the Cu species covered the molybdate surface which hindered the availability of Mo sites, which authors credit for the propene adsorption or activation and therefore the conversion rates can be said to have gone down. It is also observed from the XPS analysis that the Cu is present in the 2+

oxidation state, which is said to be the least selective oxidation state of Cu for partial oxidation and therefore, the heavy yield of carbon oxides was due to the deep oxidation of the propene molecule carried out by the Cu sites. The 2% copper, therefore, can be said to have brought an optimum synergetic effect by its interaction with the $\text{Bi}_2\text{Mo}_3\text{O}_{12}$ surface.

5.2.2 $\text{Bi}_4\text{V}_{2-x}\text{Cu}_x\text{O}_{11}$ catalysts

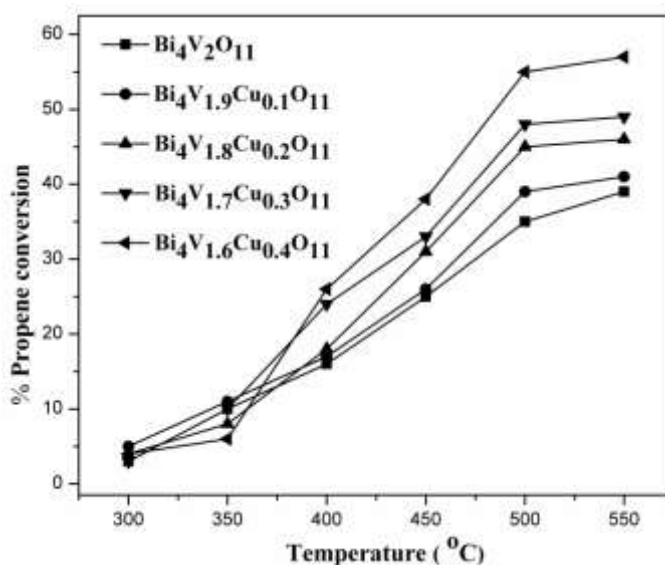


Fig. 5.3 Partial oxidation of Propene over $\text{Bi}_4\text{V}_{2-x}\text{Cu}_x\text{O}_{11}$ catalysts.

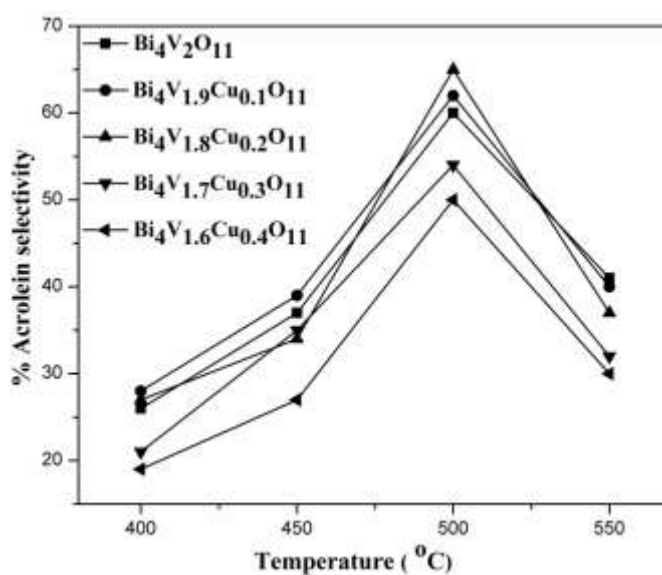


Fig. 5.4 Acrolein selectivity profile of $\text{Bi}_4\text{V}_{2-x}\text{Cu}_x\text{O}_{11}$ catalysts.

Figs. 5.3 and 5.4 display the conversion of propene and selectivity towards the acrolein respectively. The conversion starts from 300 °C over all the catalysts in the series. Conversion of propene increased with the increase in temperature. Propene conversion rate was found to increase rapidly after 400 °C which slowed down after 500 °C. The increase in Cu content was also found to have a positive effect on the conversion as the propene conversion increased with the Cu content. The selectivity of all the catalysts displayed in Fig. 5.4, shows lower selectivity towards the acrolein at a lower temperature. At the lower temperatures, the catalysts were found to favour the formation of acetaldehyde over acrolein. But as the temperature increased the acrolein selectivity also increased with the highest selectivity recorded at 500 °C, which indicates that the higher temperature was needed for the propene activation to get acrolein whereas the acetaldehyde was produced from the cleavage of the C-C bond. After 500 °C the acrolein selectivity dropped down. The product distribution over all the catalysts at 500 °C is presented in Table. 5.3.

Table 5.3. Product distribution over pristine and $\text{Bi}_4\text{V}_{2-x}\text{Cu}_x\text{O}_{11}$ catalysts

Catalyst	Temperature (°C)	Propene Conversion (%)	Selectivity (%)		
			Acrolein	Acetaldehyde	Carbon oxides
$\text{Bi}_4\text{V}_2\text{O}_{11}$	500	35	60	20	20
$\text{Bi}_4\text{V}_{1.9}\text{Cu}_{0.1}\text{O}_{11.5}$	500	39	62	26	12
$\text{Bi}_4\text{V}_{1.8}\text{Cu}_{0.2}\text{O}_{11.5}$	500	45	65	18	17
$\text{Bi}_4\text{V}_{1.7}\text{Cu}_{0.3}\text{O}_{11.5}$	500	48	54	20	26
$\text{Bi}_4\text{V}_{1.6}\text{Cu}_{0.4}\text{O}_{11.5}$	500	55	50	15	35

As observed from the Table 5.3. The highest acrolein selectivity of 65% was obtained over $\text{Bi}_4\text{V}_{1.8}\text{Cu}_{0.2}\text{O}_{11}$ catalyst. The subsequent compositions with higher Cu loading showed the decline in the selectivity towards the acrolein. The pristine

$\text{Bi}_4\text{V}_2\text{O}_{11}$ and $\text{Bi}_{4.9}\text{Cu}_{0.1}\text{O}_{11-\delta}$ showed the highest selectivity for acetaldehyde. The selectivity towards acetaldehyde did not show a trend as such which suggest that the acetaldehyde formation mechanism were the culmination of decomposition of acrolein and the separate mechanistic pathway for acrolein formation. The CO/CO_2 formation is seen to increase rapidly with the increase in the temperature and Cu content.

The increase in the propene conversion with the inclusion of Cu can be attributed towards the increased adsorption of propene over the catalyst as copper is known to be a very good activating site for the propene molecule. The vacancies created by the aliovalent doping of Cu in place of V can also be credited with the increase in the propene adsorption. The surface of the catalysts can be expected to get enriched majorly with the Bi^{+3} which is said to be the propene activating site, affecting the secondary hydrogen abstraction from allyl radical which might again facilitate the conversion of propene. All these factors are speculated to work in a concerted manner resulting in the overall increase in the propene conversion.

As discussed above, the selectivity has not taken the same trend as the conversion and was found to be the highest for the optimum concentration of $\text{Cu}_{0.2}$. The selectivity towards acrolein depends upon the selective oxygen insertion from the lattice and also on the easy removal of the formed product from the surface, as the prolonged stay on the catalyst surface could oxidize the products further resulting in the lower selectivity due to the decomposition or complete oxidation of partially oxidized products. As deduced from the XRD studies the copper inclusion has stabilized the higher temperature tetragonal phase which is known for the high ionic conductivity. The higher ionic conductivity can be associated with the higher oxygen mobility. Therefore, the reduction in the selectivity towards acrolein and the increase in the formation of carbon dioxides indicates that the catalysts are working as the oxygen sink

preventing the selective insertion of oxygen. The presence of Cu on the surface has led to the further oxidation of acrolein and acetaldehyde giving the complete oxidation products like oxides of carbon.

5.2.3 $\text{Cu}_x\text{V}_{1-x}\text{SbO}_4$ catalysts

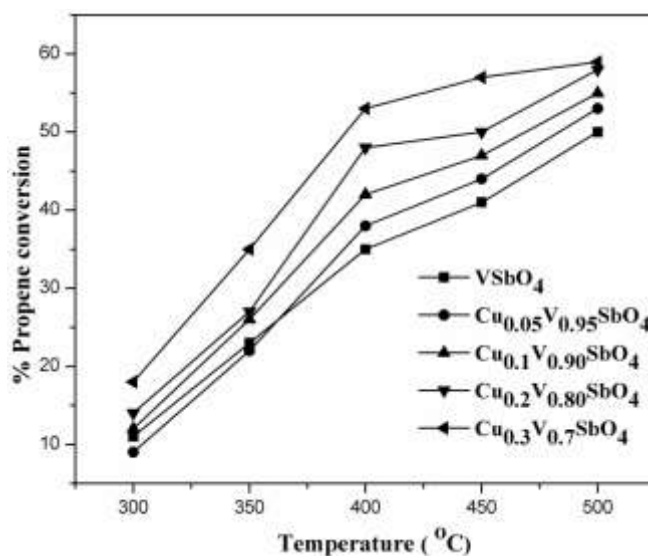


Fig. 5.5 Partial oxidation of Propene over $\text{Cu}_x\text{V}_{1-x}\text{SbO}_4$ catalysts.

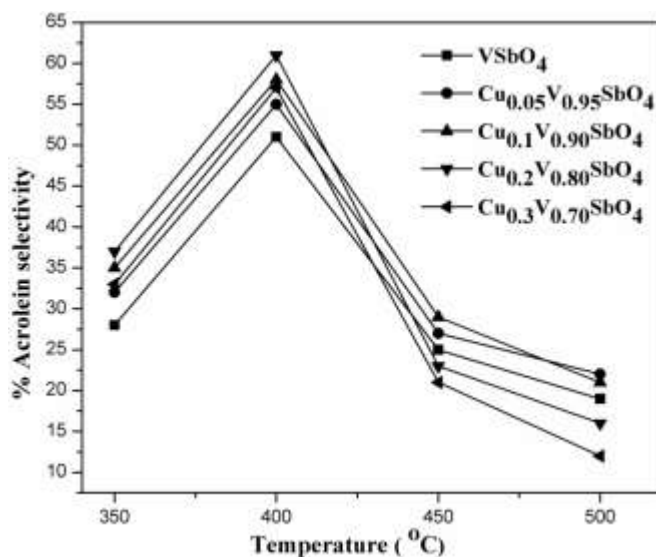


Fig. 5.6 Acrolein selectivity profile of $\text{Cu}_x\text{V}_{1-x}\text{SbO}_4$ catalysts.

Fig. 5.5 shows the conversion of propene over $\text{Cu}_x\text{V}_{1-x}\text{SbO}_4$ catalysts with respect to the rise in temperature. The effective conversion over all the catalysts started from 300 °C.

As observed from the Fig.5.5, the Cu incorporation increased the propene conversion. The conversion has increased continuously with the increase in Cu content. The Cu insertion was expected bring change in the lattice structure and also affect the surface properties of the catalysts. It is proposed that the insertion of aliovalent ions increases the vacancies over the surfaces which are helpful for the adsorption of propene. Propene tends to donate its electron density to the adsorbing sites and hence the positive vacancies formed by the inclusion of aliovalent cations work as favourable sites for the propene adsorption. This can be one of the reasons for the improved conversion of the propene. Along with the adsorption of the propene the efficient transfer of oxygen is also mandatory for the better yield of oxygenates. It is also proposed in the literature that the vacancies present in the bulk are responsible for the randomness in the lattice which is helpful for the oxygen mobility. This mobility allowed the oxide ions from the lattice to diffuse to nearby surface sites for the insertion. In this way, the improved conversion of propene obtained after the Cu insertion can be substantiated.

The selectivity of catalysts towards acrolein is displayed in the Fig.5.6. The highest selectivity was obtained at 400 °C. The product distribution at this temperature is tabulated in the Table.

Table 5.4. Product distribution over pristine VSbO₄ and Cu_xV_{1-x}SbO₄ catalysts.

Catalyst	Temperature (°C)	Propylene Conversion (%)	Selectivity (%)		
			Acrolein	Acetaldehyde	Carbon oxides
VSbO ₄	400	35	51	24	25
Cu _{0.05} V _{0.95} SbO ₄	400	38	55	20	25
Cu _{0.1} V _{0.9} SbO ₄	400	42	58	19	23
Cu _{0.2} V _{0.8} SbO ₄	400	48	61	11	28
Cu _{0.3} V _{0.7} SbO ₄	400	53	57	8	35

All the catalysts showed comparable activity towards the acrolein. Among all the catalysts, the catalysts with the composition $\text{Cu}_{0.2}\text{V}_{0.8}\text{SbO}_4$ showed the highest selectivity of 61 % with the conversion of 48 %. The production of a minor product like acetaldehyde was also seen in the substantial amount which decreased linearly with the increase in the Cu content. The formation of the completely oxidized products like CO and CO_2 also increased with the increase in the Cu content. It can be said that at the lower Cu content acetaldehyde could be formed from the oxidative cleavage of the acrolein or as a semi-cracked product from the propene. As the formation of acetaldehyde decreased with the increase in Cu content, the formation of CO_x increased which indicates that the increased Cu site on the surface favours the further oxidation of acetaldehyde or the acrolein molecules into completely oxidized products. From the above observation, it can be concluded that the Cu inclusion in the VSbO_4 catalysts can affect the catalysis in two different ways. In the first case, as discussed already pertaining to the conversion; the Cu can form the vacancies over the surface and in the bulk affecting the adsorption of propene and the oxygen mobility of the catalyst respectively. In the second case, the increased Cu content can also affect the surface sites as Cu in 2+ oxidation state is known to favour the completely oxidized products. Therefore, it can be said that the catalysts that balance both the above-said effects of the Cu incorporation tend to perform well on both the fronts of conversion and selectivity. Among this Cu inserted VSbO_4 system, the catalysts with composition $\text{Cu}_{0.2}\text{V}_{0.8}\text{SbO}_4$ can, therefore, be said to have the balance favourable factors discussed for the propene conversion and selectivity towards the acrolein.

5.2.4 Cu-K-V-Sb-O catalysts

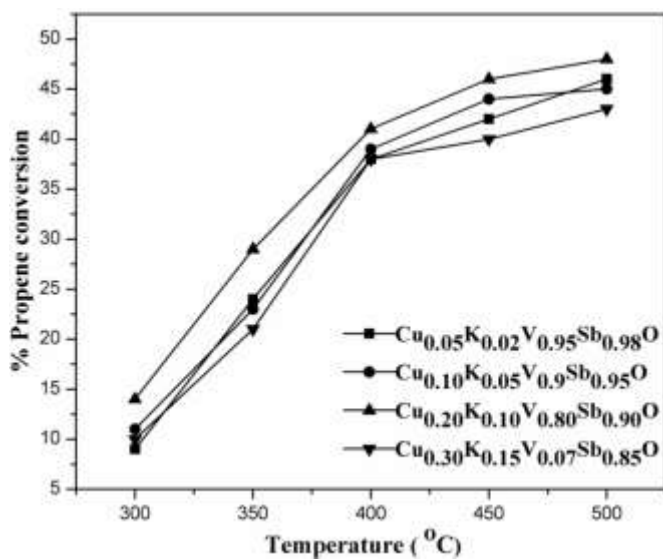


Fig. 5.7 Partial oxidation of Propene over Cu-K-V-Sb-O catalysts

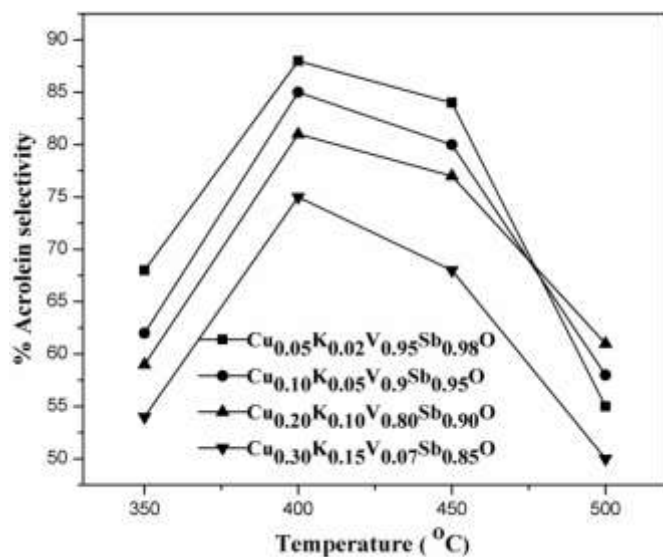


Fig. 5.8 Acrolein selectivity profile of Cu-K-V-Sb-O catalysts.

Fig. 5.7 displays the conversion of propene over Cu-K-V-Sb-O catalysts with respect to temperature. The reasonable conversion over the catalysts started from 300 °C. The catalysts prepared in this series were derivatives of the Cu inserted VSbO₄ catalysts discussed in section 5.4. Along with the Cu insertion, a redox-inactive metal ion in the form of Potassium was incorporated in the composite system. As deduced from the XRD studies already, these catalysts were not monophasic in nature but were

the mixture of different constituent phases in the composite mixture. The Potassium ion was incorporated to study its effect on the conversion and selectivity. This effect was expected on the basis of the concept called as the site isolation approach used in the literature. As discussed in relation to the $\text{Cu}_x\text{V}_{1-x}\text{SbO}_4$ system, the increase in the Cu content diminished the activity and selectivity to an extent after the optimum concentration. As observed from the Fig.5.7, it can be noticed that the conversion of propene increased with the increase in the temperature. The conversion observed in this series was slightly on the lower side than observed in previously discussed $\text{Cu}_x\text{V}_{1-x}\text{SbO}_4$ series. The increase in the conversion at a higher temperature and higher Cu content can be explained on the effects of Cu insertion already discussed in section 5.4. The important observation that can be made in relation to the present catalyst system is regarding the selectivity of the catalysts towards the propene. The selectivity profiles and the product distribution at the highest conversion temperature are presented in the Fig.5.8 and Table 5.5 respectively.

Table 5.5. Product distribution over pristine VSbO_4 and $\text{Cu}_x\text{V}_{1-x}\text{SbO}_4$ catalysts.

Catalyst	Temperature (°C)	Propene Conversion (%)	Selectivity (%)		
			Acrolein	Acetaldehyde	Carbon oxides
$\text{Cu}_{0.05}\text{K}_{0.02}\text{V}_{0.95}\text{Sb}_{0.98}\text{O}$	400	38	88	5	7
$\text{Cu}_{0.1}\text{K}_{0.05}\text{V}_{0.90}\text{Sb}_{0.95}\text{O}$	400	39	85	7	8
$\text{Cu}_{0.2}\text{K}_{0.10}\text{V}_{0.80}\text{Sb}_{0.90}\text{O}$	400	41	81	10	9
$\text{Cu}_{0.3}\text{K}_{0.15}\text{V}_{0.70}\text{Sb}_{0.85}\text{O}$	400	38	75	14	11

The selectivity over all these catalysts at 400 °C was found to be above 70 %. The increase in the selectivity towards the acrolein could be associated with the inclusion of K^+ in the catalyst system. Potassium ion being a bigger ion was not expected to enter in the crystal lattice of major phase VSbO_4 . Therefore, it is highly like

that the K^+ ions are scattered over the catalyst surface in the form of K_2O that can be speculated to cover the surface of the catalyst. The Cu species which favours the formation of the completely oxidized species may have got buried beneath this K_2O phase. The selectivity towards the catalysts was relatively sustained at 450 °C but subsequently fell drastically to around 50% at 500 °C. This fall in the selectivity could be due to the increased flux of oxygen on the surface and the catalysts brought about by the increased mobility due to the thermal agitations in the crystal lattice. The one thing is clear from the above discussion that the incorporation of K ions has improved the selectivity by diluting the redox sites over the catalysts. It can also be said that the presence of K_2O also might facilitate the desorption of oxygenated products thus preventing them from getting oxidized further into completely oxidized products.

5.2.5 $\text{Bi}_2\text{Mo}_{1-x}\text{W}_x\text{O}_6$ catalysts

As discussed already during the literature review, the Bi_2MoO_6 and its other two phases namely $\text{Bi}_2\text{Mo}_3\text{O}_{12}$ and $\text{Bi}_2\text{Mo}_2\text{O}_9$ have been investigated profoundly in the reports. In this present study, W was substituted in place of Mo in Bi_2MoO_6 to investigate the catalytic activity of the resultant compositions. W substitution was expected to cause a structural change in the basic structure of the Bi_2MoO_6 and in turn affect the resultant catalytic activity for the partial oxidation of propene. The conversion of propene over as prepared and acid enriched catalysts is presented in Fig. 5.9 and Fig. 5.10 respectively.

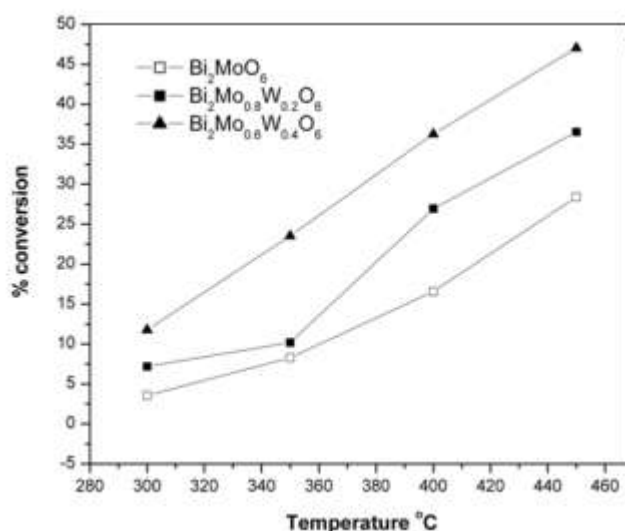


Fig. 5.9 Partial oxidation of Propene over as prepared $\text{Bi}_2\text{Mo}_{1-x}\text{W}_x\text{O}_6$ system

Propylene conversion and product distribution over the as-prepared catalysts are summarized in Table 5.6. In case of all the catalysts, the conversion increased with the increase in temperature. Significant propylene conversion was observed at temperatures higher than 300 °C over all the catalysts. Bi_2MoO_6 based catalysts are known to provide oxygen from the lattice for oxidation and at the same time harness oxygen from the feed gas to get re-oxidized. The rate of this cycle is faster at higher temperatures and therefore, the higher yield of oxygenated products at higher temperatures.

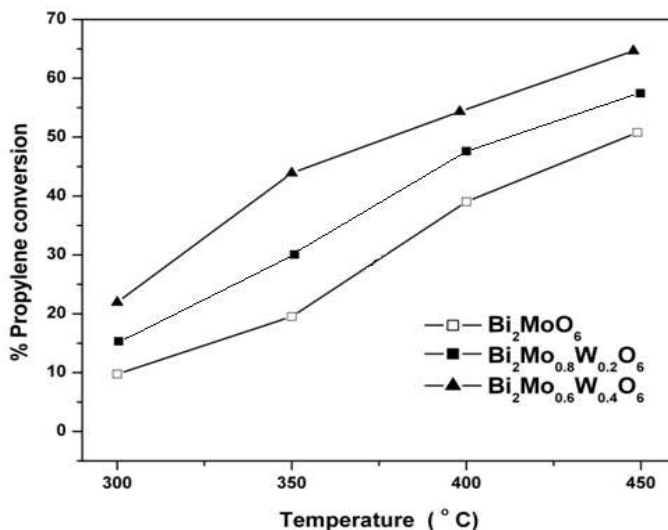


Fig 5.10. Partial oxidation of Propene over acid enriched $\text{Bi}_2\text{Mo}_{1-x}\text{W}_x\text{O}_6$ system

Table 5.6 Product distribution over pristine and W doped Bi_2MoO_6

Catalyst	Temperature (°C)	Propylene Conversion (%)	Selectivity (%)		
			Acrolein	Acetaldehyde	Carbon oxides
Bi_2MoO_6	400	15.0	98.0	1.0	1.0
	450	28.0	95.0	2.0	3.0
$\text{Bi}_2\text{Mo}_{0.8}\text{Mo}_{0.2}\text{O}_6$	400	25.5	94.0	2.0	4.0
	450	37.5	92.0	3.0	5.0
$\text{Bi}_2\text{Mo}_{0.6}\text{W}_{0.4}\text{O}_6$	400	36.3	96.0	0.0	4.0
	450	47.2	94.0	1.0	5.0

W inserted catalysts were found to give better conversion than pristine Bi_2MoO_6 . Among the prepared catalysts, $\text{Bi}_2\text{Mo}_{0.6}\text{W}_{0.4}\text{O}_6$ showed highest propylene conversion. The mobility of oxygen atoms on the catalytic surface should be greater in number for better catalytic partial oxidation. When slightly bigger W ion replaces Mo from Bi_2MoO_6 it is expected to increase the cell volume. The increase in the cell volume, in turn, has led to the weakening of Mo-O bond. This has helped for the easy removal of oxygen from the catalyst surface to form the partially oxygenated species like acrolein. Also in the XPS studies already discussed in the section, the broadened O 1s spectra have indicated the presence of mobile oxygen in the crystal lattice.

As observed from the Fig 5.10, all the acid enriched compounds gave higher propylene conversion than as prepared compounds. Product distribution over acid enriched compounds did not differ significantly from the as-prepared compounds. The trend observed among the three catalysts for the propylene catalytic conversion was same as that for as prepared compounds. Maximum propylene conversion of 65% was observed in the case of acid enriched $\text{Bi}_2\text{Mo}_{0.6}\text{W}_{0.4}\text{O}_6$. The higher conversion, therefore, points at the increased adsorption of propylene on the acid enriched surface. As the propylene oxidation starts above 300 °C mark it is essential to have a good number of adsorptive sites of sufficient strength on the catalyst surface for the better conversion. In these regards, the increased amount of mild and strong acidic sites on acid enriched catalysts have played a major role in the increased adsorption of propylene leading to an improved conversion which is aptly supported by NH_3 TPD studies presented in the Fig. 5.11.

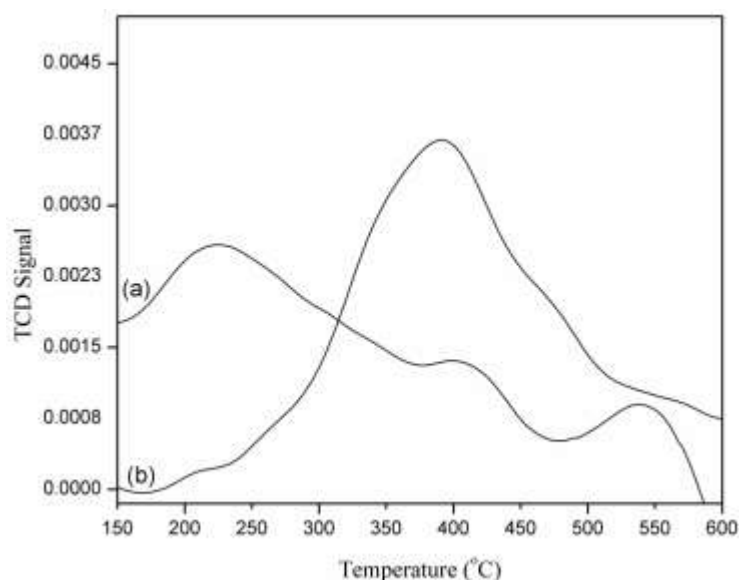


Fig. 5.11 NH_3 TPD studies on $\text{Bi}_2\text{Mo}_{0.6}\text{W}_{0.4}\text{O}_6$ (a) as prepared (b) acid enriched.

As prepared catalysts showed three distinct peaks, i) Up to 300 °C ii) Between 350-475 °C and iii) Beyond 475 °C suggesting there are three types of major acidic sites which can be classified as weak, mild and strong. The first peak showed higher

intensity than the rest of the peaks observed at higher temperatures suggesting a higher number of weak acid sites. In case of the acid enriched catalysts, a steadfast distinction among the acidic sites was not observed, a very small hump in the weak acid region was observed followed by a broad and a relatively intense desorption of NH_3 covering the temperature range from 250 °C to 500 °C signifying a considerable decrease in the weak acidic sites and an increase in the mild and strong acidic sites. This observation proves that the acid enrichment has altered the surface acidic character of the catalysts.

It must be also noted that the strong acidic sites can cause a prolonged stay of the oxygenated compounds on the surface leading to further oxidation to Carbon oxides resulting in the fall of selectivity towards the desired product i.e. Acrolein. In the present case, the selectivity was not altered due to the increased surface acidity which proves that the surface acid enrichment has only increased the adsorptive sites on the surface without having any adverse effect on the selective oxidation.

5.2.6 $\text{M}_3\text{V}_2\text{O}_8$ (M = Ca, Sr and Ba) catalysts

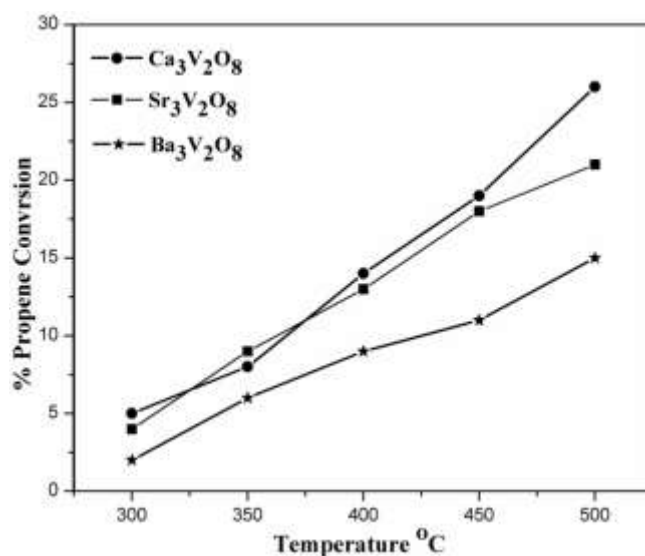


Fig. 5.12 Partial oxidation of propene over $\text{Me}_3\text{V}_2\text{O}_8$ catalysts.

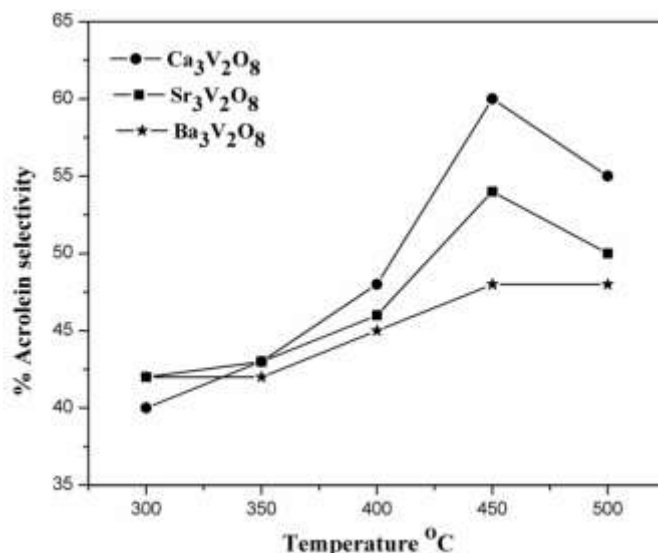


Fig. 5.13 Acrolein selectivity profile of $Me_3V_2O_8$ catalysts.

Fig. 5.12 presents the extent of conversion of propene to the oxygenated compounds over alkaline earth metal vanadates. The onset of the propene conversion was from 300 °C. The conversion of propene increased with the increase in the temperature, The propene conversions over $Ca_3V_2O_8$ and $Sr_3V_2O_8$ were almost identical up to 450 °C, after which the activity showed by the $Ca_3V_2O_8$ showed an increase whereas the $Sr_3V_2O_8$ maintained its regular trajectory. $Ba_3V_2O_8$ showed considerably lower conversion, the maximum conversion shown by these catalysts was as high as 15 %.

The Fig. 5.13 displays the acrolein selectivity profile of the catalysts. Initially, up to 450 °C, the selectivity towards acrolein increased with the increase in temperature after which it dropped and the lowest was observed at 500 °C. The product distributions for all the three catalysts at 450 °C and 500 °C are presented in Table 5.7. Maximum selectivity of 60% for the acrolein was shown by $Ca_3V_2O_8$ also $Sr_3V_2O_8$ was not far behind which had a selectivity of 54 % for the acrolein at 450 °C. In case of all the catalysts, the maximum selectivity was observed at 450 °C and was only maintained by

Ba₃V₂O₈ at 500 °C. Along with the acrolein, acetaldehyde also was found to be a major product accounting for almost 40 % of share in the overall yield.

Table 5.7. Product distribution M₃V₂O₈ catalysts (M = Ca, Sr and Ba)

Catalyst	Temperature (°C)	Propylene Conversion (%)	Selectivity (%)		
			Acrolein	Acetaldehyde	Carbon oxides
Ca ₃ V ₂ O ₈	450	19	60	25	15
	500	26	55	38	7
Sr ₃ V ₂ O ₈	450	18	54	35	11
	500	21	50	38	12
Ba ₃ V ₂ O ₈	450	11	48	31	21
	500	15	48	45	7

At higher temperatures, the selectivity towards the completely oxidized product usually increase but as can be observed from the product distribution table the selectivity towards the carbon oxides in case of Ca₃V₂O₈ ad Ba₃V₂O₈ decreased slightly at 500 °C whereas in case of Sr₃V₂O₈ it almost remained unchanged. This suggests that somehow the catalysts favour acetaldehyde formation over the carbon oxide formation.

The lower activity observed in the alkaline earth metal vanadates can be attributed towards the lack of a redox couple other than the V⁺⁵. The V⁺⁵ usually can be considered as an adsorptive site for propene. The lack of the redox activity and thus the oxygen mobility thereof seems to be the main reason behind the low conversions observed in this case. It can be also observed from the table that the selectivity towards the acetaldehyde and carbon dioxide did not increase to a great extent at higher temperatures. This indicates that they are not the products of the acrolein decomposition but are more likely to be formed from the separate reaction pathways not involving acrolein as the intermediate. The lower formation of CO₂ at 500 °C than the

acetaldehyde also indicates the same fact. These observations suggest that the lack of redox couple in the alkaline earth metal vanadates has caused the lack of oxygen participation from the lattice. And thus the lower activities are observed.

6. SUMMARY AND CONCLUSIONS

This chapter will present a rapid glance over the work and the important findings reported in this thesis. The major conclusions derived from the investigations are stated concisely.

6.1 Summary

The thesis basically deals with the preparation of some selected metal oxides and their systematic characterization. The metal oxide systems were envisioned and selected based on their applicability to the fields under consideration, namely heterogeneous catalysis, and study of luminescence properties. In case of heterogeneous catalysis, partial oxidation of propene to acrolein was studied, whereas the luminescence studies dealt with the study of optical properties of the R.E doped $\text{Ca}_3\text{V}_2\text{O}_8$ host. The utility of the prepared metal oxides towards the above applications was studied considering structure-property relations. An effort was made to put the findings in a proper scientific perspective. A chapter wise overview of the content compiled in the thesis is presented in the following paragraphs.

Chapter 1 provided a brief introduction and scope of the research work carried out in the thesis. A comment was made on the general trends observed in the fields of material preparation, catalysis, and luminescence. The role of heterogeneous catalysis in the industrial sector and the applicability of efficient phosphors in today's light sources were discussed. The main outcomes of the work were highlighted and the overall organization of the thesis was presented in this chapter.

Chapter 2 presented a review of the extensive literature published on the topics of partial oxidation of propene and luminescence studies. In relation to the partial oxidation of propene, an attempt was made to trace all the reported catalytic systems.

Efforts were made to understand the active centres and synergy effects in these catalytic systems. Similarly, with regards to the luminescence studies, a survey of substitution of R.E ions in the $\text{Ca}_3\text{V}_2\text{O}_8$ host lattice along with the different doping schemes employed was done. The above compilation gave fair ideas regarding the behaviour and utilization of $\text{Ca}_3\text{V}_2\text{O}_8$ as a promising host material for the R.E ions.

Chapter 3 dealt with the experimental aspects of the work reported in the thesis. Preparative procedures of the materials were reported in detail. The underlying principles of the instrumental techniques used for the characterization along with their working were discussed. Brief procedures for the handling of the simple instruments and the specifications of all the instruments were presented. The schematics of the catalytic set up was explained and the essential terms of partial oxidation such as conversion and selectivity were defined.

Chapter 4 revealed the systematic account of the characterization of the prepared materials using different analytical and spectroscopic techniques. The thermal behaviour of the metal oxide precursors and the thermal stabilities of ensuing oxides were elucidated using TG/DTA analysis. The metal oxide systems prepared were analyzed for their phase formation and elemental purity using the techniques such as XRD, IR, Raman and XPS spectroscopy. Luminescence spectra of all the prepared phosphors were presented and explained in this chapter.

Chapter 5 featured basic characterizations of the catalysts such as the surface area measurements. A complete account of the catalytic activity measurements over the prepared catalyst systems was presented in here. Taking into consideration the structural characterization of the materials, the elucidations of the catalytic activity measurements were made relating the structure and catalytic behaviour.

6.2 Conclusions

From the literature review, it can be concluded that the catalytic systems for the partial oxidation of propene are mostly the acidic oxides with variable oxidation states. Apart from the Bi-Mo based oxides, other systems such as antimonates and vanadates have also been ventured but they could not reach the performance levels of molybdates. Bi-Mo oxides are found to be a base composition for all the commercial catalysts. Throughout the literature, it is agreed that the partial oxidation of propene takes place with the following steps.

- i) Adsorption of propene on a Lewis acidic site.
- ii) Abstraction of hydrogen by an adjacent site to form an allyl radical.
- iii) Allyl radical is inserted with oxygen to form acrolein

Depending upon how catalysts can affect the above steps determine its performance. For example, too much of acidity on the catalyst can lead to significant decrease in the selectivity, similarly, lack of sufficient oxygen mobility leads to the decrease in the yield of oxygenated products. Only the catalyst with optimum attributes needed for the partial oxidation can give better conversion and selectivity.

Regarding the luminescence studies, it was noticed in the literature that the alkaline earth vanadates are tested extensively as host materials for the search of white LEDs. The thermal stability, transparency and lower cost of preparation have added to their candidacy as the host materials. Different activator R.E ions with their characteristic colour rendering properties are substituted in these alkaline earth vanadates so as to get the finely tuned colour emissions. It is also learned from the literature that each R.E ions have their own critical dopant concentration at which they

yield intense luminosity. The doping combinations, doping schemes, and dopant concentrations are the important factors that affect the luminescence.

In the present work, preparative techniques such as co-precipitation and sol-gel have been successfully employed. Different complexing acids such as Citric acid, Malic acid, EDTA and Tartaric acid are used for the sol-gel preparations. Co-precipitation technique is only used for the preparation of $\text{Bi}_2\text{Mo}_3\text{O}_{12}$ compounds. Thermal analysis done on TG/DTA analyzer for all the metal oxide precursors supplied the important information regarding the decomposition patterns of the carbonaceous precursors. The final calcination or sintering temperatures were fixed by following the TG curve. All the metal oxides systems prepared were found to be stable thermally.

All the metal oxide systems were monophasic as deduced from the XRD studies. The diffraction files matched well with the respective standard JPDS cards. The IR studies revealed the complete absence of the organic impurities in the metal oxide systems. The characteristics peaks relating to the vanadate and molybdate moieties were seen in their respective regions. Raman spectra were especially useful in case of the $\text{Ca}_3\text{V}_2\text{O}_8$ phosphors in confirming the phase purity and also supplying the important information regarding the crystallinity and local structures as they play an important role in the luminescence.

Propene partial oxidation carried out on the catalytic systems gave valuable insights about their performance and mechanistic pathways. In the case of $\text{Cu}/\text{Bi}_2\text{Mo}_3\text{O}_{12}$ catalysts, it is found that the 2% Cu loadings on $\text{Bi}_2\text{Mo}_3\text{O}_{12}$ increases the conversion and selectivity whereas the subsequent higher loadings of Cu is found to be detrimental to the propene selectivity majorly due to the non-selective nature of Cu^{2+} species present on the surface. The decline in the propene conversion is attributed to the

masking of highly active Mo^{6+} sites by increased Cu loadings. The drop in the selectivity was due to the non selective nature of Cu^{2+} towards partially oxidised products like acrolein.

Cu inserted $\text{Bi}_4\text{V}_2\text{O}_{11}$ system showed the fairly good conversion of propene. The conversion of propene has increased with the Cu content but the same trend is not followed by the selectivity as the Cu content has brought down the selectivity. The vacancies created by the Cu doping are thought to be the helping factor in the propene conversion. XRD studies suggest the stabilization of γ phase of $\text{Bi}_4\text{V}_2\text{O}_{11}$ by the substitution of Cu. This tetragonal phase has very high ionic conductivity. The randomness created by the Cu doping and the stabilization of highly conducting phase are thought to be the main factors responsible for the higher production of completely oxidized products at higher temperatures.

Cu doped VSbO_4 system has shown the similar results. The conversion of propene increased with the increase in the Cu content. Selectivity towards propene increased up to an optimum temperature from where it decreased. This decline is substantiated by the increased amount of vacancies created by the aliovalent doping of Cu in the VSbO_4 crystal lattice. The Cu-V-Sb-K-O composite catalysts showed better selectivity towards acrolein. The increase in selectivity seems to be due to the isolation and masking of Cu sites on the surface by the K containing phases like K_2O . This K_2O phase is also proposed to initiate the easy desorption of oxygenated products from the surface preventing the further oxidation of oxygenated products thus retaining the selectivity towards acrolein.

W inserted Bi_2MoO_6 showed better conversion than the pristine Bi_2MoO_6 . The increase in the cell volume due to W doping has caused the easy removal of oxygen

ions from the lattice resulting in the better conversion. The acid enriched catalysts have shown the better conversion than as prepared catalysts due to the increased adsorptive sites on the surface of the catalyst. The increased acidic sites have not caused any detrimental effects on acrolein selectivity.

Alkaline earth metal vanadates did not show a great deal of propene conversion which can be assigned to the lack of separate redox centre apart from V^{5+} in the system, which is very much essential for the oxygen insertion and for Mars van Krevlen mechanism to occur.

R.E-doped $Ca_3V_2O_8$ phosphors were successfully prepared by a Malic acid assisted sol-gel process. This process offers a softer route to these compounds taking into the consideration the extensive use of solid state approach found in the literature. The sol-gel process offers homogeneity and has reduced the sintering time.

The band gap values obtained are in the range of 3.5-3.6 eV, thus confirming the semiconductor nature of the phosphors. In all the four series, band gap values decreased to a small extent upon the doping of RE ions. This could be due to the impurity energy levels formed just above the valence band or below the conduction band.

Tb singly doped series and Na-Tb co-doped samples showed the characteristic green emissions. The optimum concentration of Tb in singly doped phosphors is found to be at $Tb = 0.08$ whereas the optimum concentration for Na-Tb co-doped samples is located at $Tb = 0.12$. The singly doped series could not sustain the luminescence intensity after the optimum concentration, but co-doped series showed luminescence even after the optimum concentration. The vacancy concentration, homo ion interactions, local disorder are thought to be the main reason behind the decreased intensity of green emission in the Tb singly doped compounds. On the other hand, due

to the vacancy compensation in co-doped samples, the above said factors are minimized resulting in the sustained luminescence intensity. The shift in the excitation wavelength from singly doped compounds to the co-doped compounds hinted the change in the sensitization mechanism.

In Ce-Tb co-doped $\text{Ca}_3\text{V}_2\text{O}_8$ samples, the characteristic green emissions of Tb are observed. The role of Ce^{3+} as a sensitizer ion is proved as the Ce emissions have decreased in the Ce-Tb co-doped samples. The energy is transferred from Ce^{3+} to Tb^{3+} , as a result of which the Ce^{3+} emissions are quenched.

In Eu-Tb co-doped samples, the Tb^{3+} ions could not be excited at the excitation wavelength applicable to the Eu^{3+} suggesting a lack of energy transfer from Eu to Tb. But it is also learned from the spectral studies that the excitation wavelength corresponding to the Tb could initiate the Eu emissions suggesting an energy transfer from the Tb to Eu. Therefore, a simultaneous emission of Eu and Tb are found to be possible. This enables the phosphors to emit the green and red emissions simultaneously.

REFERENCES

1. R.A. Sheldon, *Green Chem.* 9 (2007) 1273.
2. P.T. Anastas, L.B. Bartlett, M.M. Kirchhoff, T.C. Williamson, *Catal. Today.* 55 (2000) 11.
3. F. Cavani, J.H. Teles, *ChemSusChem* 2 (2009) 508.
4. G. Martino, in 12th International Congress on Catalysis (Studies in Surface Science and Catalysis Series, Elsevier: Amsterdam, Vol. 130 (2000) p 83.
5. R. K. Grasselli, *Handbook in Catalysis*, WileyVCH: New York. Vol. V (1997) pp 2302.
6. J. H. Lunsford, *Catal. Rev.* 12 (1975) 13.
7. B. K. Hodnett, *Heterogeneous Catalytic Oxidation*, Wiley-VCH, Weinheim. (2000)
8. R. K. Grasselli, *Catal. Today* 49 (1999) 141.
9. R. K. Grasselli, *Top. Catal.* 21 (2002) 79.
10. B. Grzybowska-Swierkosz, *Top. Catal.* 21 (2002) 35.
11. N.Song, C. Rhodes, J. K. Bartley, S. H. Taylor, D. Chadwick, G. J.Hutchings, *J. Catal.* 236 (2005) 282.
12. S. Pudar, J. Oxgaard, W. A. Goddard III, *J. Phys. Chem. C.* 114 (2010) 15678.
13. D. M. Perez Ferrandez, M. H. J. M. de Croon, J. C. Schouten, T. Alexander Nijhuis, *Ind. End. Chem. Res.* 52 (2013) 10126.
14. R.L. Webster, D. J. Evans, P. M. Rawson, B. S. Mitrevski, P. J. Marriott, *Energy Fuels.* 27 (2013) 889.
15. Halcon, US patent 117 (1984)146
16. D. Bhattacharya, S.K. Bey, M.S. Rao, *Appl. Catal. A.* 87 (1992) 29
17. I.M. Dahl, K. Grande, K.J. Jens, E. Rytter, A. Slagtern, *Appl. Catal.* 77 (1991) 163.
18. R. Grabowski, *Catal. Rev. Sci. Eng.* 48 (2006) 199.

19. F. Cavani, N. Ballarini, A. Cericola, *Catal. Today*. 127 (2007) 113.
20. J.-P. Lange, *CATTECH*. 5 (2001) 82.
21. E. A. Mamedov, V. Cortes-Corberan, *Appl. Catal. A*. 127 (1995) 1.
22. J.L. Callahan, R.K. Grasselli, E.C. Milberger, H.A. Strecker, *Ind. Eng. Chem. Prod. Res. Dev.* 9 (1970) 134.
23. F. Veatch, J.L. Callahan, J.D. Idol, E.C. Milberger, *Chem. Eng. Progr.* 56 (1960) 65.
24. W.K. Lewis, E.R. Gilliland, W.A. Reed. *Ind. Eng. Chem.* 41 (1949) 1227.
25. F. Zaera. *J. Phys. Chem. B* 106 (2002) 4043.
26. C.R. Jung, A. Kundu, S.W. Nam, H-I Lee, *Appl. Catal. B*. 84 (2008) 435.
27. F. Romero-Sarria, A. Penkova, L.M. Martinez, M.A. Centeno, K. Hadjiivanov, J.A. Odriozola, *Appl. Catal. B*. 84 (2008) 119.
28. A. Bielanski, J. Haber, *Oxygen in Catalysis*, Third Ed., New York (1991) pp.159
29. S. Saha, S. Das, U.K. Ghorai, N. Mazumder, B.K. Gupta, K. K. Chattopadhyay, *Dalton Trans.* 42 (2013) 12965.
30. F. Du, R. Zhu, Y. Huang, Y. Tao and H. Jin Seo, *Dalton Trans.* 40 (2011) 11433.
31. J. Choi, T.K. Tseng, M. Davidson, P. H. Holloway, *J. Mater. Chem.* 21 (2011) 3113.
32. W.N. Wang, F. Iskandar, K. Okuyama, Y. Shinomiya, *Adv. Mater.* 20 (2008) 3422.
33. J.E. Huheey, E.A. Keiter, R.L. Keiter, O.K. Medhi, *Inorganic Chemistry-Principles of Structure and Reactivity*, Pearson Education Inc, 4th Edition (1993).
34. C. Feldmann, T. Jüstel, C. Ronda, P. Schmidt, *Adv. Funct. Mater.* 13 (2003) 511.
35. H.A. Hoppe, *Angew. Chem., Int. Ed.* 48 (2009) 3572.
36. L. Li, Y. Su, G. Li, *J. Mater. Chem.* 20 (2010) 459.
37. Y. Liu, D. Tu, H. Zhu, R. Li, W. Luo, X. Chen, *Adv. Mater.* 22 (2010) 3266.

38. S. Wang, R. Deng, H. Guo, S. Song, F. Cao, X. Li, S. Su, H. Zhang, Dalton Trans. 39 (2010) 9153.
39. Y. Fang, Y. Xiong, Y. Zhou, J. Chen, K. Song, Y. Fang, X. Zhen, Solid. State . Sci. 11 (2009) 1131.
40. L. H. Brixner, J. Solid State Chem. 1 (1970) 185.
41. P.P. Mokoena, M. Gohain, B.C.B. Bezuidenhoudt, H.C. Swart, O.M. Ntwaeaborwa, J. Lumin. 155 (2014) 288.
42. M.M. Bettahar, G. Costentin, L. Savary, J.C. Lavalley, Appl. Catal. A: Gen. 145 (1996) 1.
43. A. Takahashi, N. Hamakawa, I. Nakamura, T. Fujitani, Appl. Catal. A: Gen. 294 (2005) 34.
44. G. Wegener, M. Brandt, L. Duda, J. Hofmann, B. Kleszczewski, D. Koch, R.-J. Kumpf, H. Orzesek, H -G. Pirkl, C. Six, C. Steinlein, M. Weisbeck, Appl. Catal. A. 221 (2001) 303.
45. Internet Source, <https://en.wikipedia.org/wiki/Acrolein>
46. 'Acrolein derivatives- Kirk Othmer encyclopaedia of chemical technology', 4th ed, Vol. 1 (1997) pp 232.
47. S. Uchiyama, Y. Inaba, N. Kunugita, J. Chromaography. 1217 (2010) 4383.
48. Z. Feng, W. Hu, Y. Hu, M.S. Tang, Proc. Natl. Acad. Sci. U.S.A. 103 (2006) 15404
49. G.W. Hearne, E. Cerrito, M.L. Adams, (1948) US 2451485 19481019
50. G. W Hearne, M. L. Adams (1949) US 2486842 19491101
51. N.I. Popova, E.E. Vermel, Doklady Akademii Nauk SSSR 124 (1959) 842.
52. C.R. Adams, T.J. Jennings, J. Catal. 3 (1964) 549
53. K.H. Shultz, D.F. Cox, J. Catal. 143 (1993) 464.
54. H.S. Choi, J. T. Lin, R. L. Kuczkowski, J. Catal. 99 (1986) 72.

55. A.A. Davydov, V G. Mikhal'Chenko, V. D. Sokolovskii, G. K. Boreskov, J. Catal. 55 (1978) 299.
56. B.J. Wood, H. Wise, R.S. Yolles, J. Catal. 15 (1969) 355
57. C.A. Woodcock (1949) Patent No.655, 210, 2
58. L. Holbrook, H. Wise, J. Catal. 20 (1971) 367
59. T. Inui, T. Ueda, M. Suehiro, J. Catal. 65 (1980) 166
60. B. Ya, I. Gorokhovatskii, I. Vovyanko, M. Ya. Rubanik, Kinet. Katal; 7 (1966) 76.
61. H. Tuysuz, J. J. Galilea, Catal. Lett; 131 (2009) 49.
62. J. B. Reitz, E. I. Solomon, J. Am. Chem. Soc; 120 (1998) 11467.
63. V. G. Mikha'Chenko, V. D. Solokovskii, G. K. Boreskov, Kinet. Katal. 14 (1973) 698.
64. V. G. Mikha'Chenko, V. D. Solokovskii, A. A. Fillipova, A. A. Davydov, Kinet. Katal; 14 (1973) 1253.
65. J. R. Labastida-Bardales, R. R. Hudgins, P. L. Silveston, The Canadian Journal of Chemical Engineering. 67 (1989) 418.
66. J. Haber, J. Stoch, T. Wiltowski, 'Surface Transformations of Copper Molybdate Catalysts', New Horizons in Catalysis, part B, T. Seiyama, K. Tanabe, eds. (1980) pp. 1402.
67. J. Haber, Izvestiya Khimiya. XIII (1980) 65.
68. J-S Yu, L. Kevan, J. Phys. Chem. 95 (1991) 6648.
69. J-S Yu, L. Kevan, The Journal of Physical Chemistry. 95 (1991) 3262.
70. C-H Liu, N-C Lai, J-F Lee, C-S Chen, C-M Yang, J. Catal. 316 (2014) 231
- 70^a. D. Duzenli, D. O. Atmaca, M.G. Gezer, I. Onal, Appl. Surf. Sci. 355 (2015) 660.
71. F. Veatch, J. L. Callahan, E. C. Milberger, R. M. Foreman, Proc. 2nd catalysis conference; (1960) Paris.

72. R. K. Grasselli, J. D. Burrington, *Advances in Catalysis*, Academic Press New York. Vol. 30 (1981) pp.133.
73. J. L. Callahan, R. K. Grasselli, *J. Am. Inst. Chem. Eng.* 9 (1963) 755.
74. G. W. Keulks, *J. Catal.* 19 (1970) 232.
75. G. W. Keulks, L. D. Krenzke, 6th Intl. Congress on Catalysis, London; (1976) pp. 806.
76. P. A. Batist, B. C. Lippens, G. C. A. Schuit, *J. Catal.* 5 (1966) 55.
77. K. German, B. Grzybowska, J. Haber, *Br. Acad. Pol. Sci. Chim.* 11 (1973) 319.
78. I. K. Kolchin, E. L. Gla'perin, S. S. Bobkov, L. YA. Mrgolis, *Kinet. Catal.* 6 (1965) 794.
79. D. Carson, G. Coudurier, M. Forissier, J. C. Vedrine, A. Laarif, F. Theobald, *J. Chem. Soc. Faraday Trans. I* 79 (1983) 1921.
80. Z. Bing, S. Pei, S. Shishan, G. Xiexan, *J. Chem. Soc. Faraday. Trans.* 86 (1990) 3145.
81. J. R. Monnier, G. W. Keulks, *Preprints Am. Chem. Soc. Div. Petr. Chem.* 24 (1979) 19.
82. J. D. Burrington, R. K. Grasselli, *J. Catal.* 59 (1979) 79.
83. L. D. Krenzke, G. W. Keulks, *J. Catal.* 64 (1980) 295.
84. B. R. Sant, S. B. Rao, J. R. Rao, R. S. Thakur, K. M. Parida. *J. Sci. Ind. Res.* 43 (1984) 542.
85. G. I. Aleshina, C. Joshi, D. V. Tarasova, G. N. Kustova, T.A. Nikoro, *React. Kinet. Catal. Lett.* 26 (1984) 203.
86. W.J.M. van Well, M. T. Le, N. C. Schiodt, S. Hoste, P. Stoltze, *J. Mol. Cat. A: Chemical.* 256 (2006) 1
87. P.A. Batist, *J. Chem. Technol. Biotechnol.* 29 (1979) 451

88. P. A. Batist, J.F.H. Bouwens, G.C.A. Schuit, *J. Catal.* 25 (1972) 1.
89. D.A.G. van Oeffelen, J.H.C. van hoof, G.C.A. Schuit, *J. Catal.* 95 (1985) 84.
90. I. Matsuura, R. Schut, K. Hirakawa, *J. Catal.* 63 (1980) 152.
91. P. M. Burban, G.C.A Schuit, T.A. Koch, K.B. Bischoff, *J. Catal.* 126 (1990) 326.
92. M.T. Le, W.J.M. Van well, P. Stoltze, I.V. Driessche, S. Hoste, *Appl. Catal. A: Gen.* 282 (2005) 189.
93. D. Carson, M. Forissier, J.D. Vadrine, *J. Chem. Soc; Faraday Trans. 1* 80 (1984) 1017.
94. A.P.V Soares, L.D. Dimitrov, M.C.-R.A de Oliveira, L. Hilaire, M.F. Portela, R.K. Grasselli, *Appl. Catal. A: Gen.* 253 (2003) 191.
95. M.T. Le, J. Van Craenenbroeck, I. Driessche, S. Hoste, *Appl. Catal. A: General*, 249 (2003) 355.
96. J.D. Burrington, C.T. Kartisek, R.K. Grasselli, *J. Catal.* 87 (1984) 363.
97. J.D. Burrington, C.T. Kartisek, R.K. Grasselli, *J. Catal.* 81 (1983) 489.
98. L. T. We, B. Delmon, *Appl. Catal. A.* 81 (1992) 141.
99. O. Legendre, Ph. Jaeger, J.P. Brunelle, *Stud. Surf. Sci. Catal.* 72 (1992) 387.
100. Y. Moro-Oka, D.H. He, W. Ueda, *Stud. Surf. Sci. Catal.* 67 (1991) 57.
101. J.M.M. Millet, H. Ponceblanc, G. Codurier, J.M. Hermann, J.C. Vadrine, *J. Catal.* 142 (1993) 381.
102. H. Ponceblanc, J.M.M. Millet, G. Codurier, J.M. Hermann, J.C. Vadrine, *J. Catal.* 143 (1993) 373.
103. E.V. Hoefs, J.R. Monnier, G.W. Keulks, *J. Catal.* 57 (1979) 331.
104. L.D. Krenzke, G.W. Keulks, *J. Catal.* 61 (1980) 316.
105. Y. Moro-oka, W. Ueda, S. Tanaka, T. Ikawa, *Proc. 7th Int. Congr. Catalysis*, Tokyo, 1980, Vol. 191, p. 1086.

106. W. Ueda, Y. Moro-oka, T. Ikawa, *J. Catal.* 70 (1981) 409.
107. Japan Patent, 48- 1645U (1973)
108. US Patent, 3, 825, 600 (1974)
109. Y. Moro-oka, W. Ueda, *Adv. Catal.* 40 (1994) 233.
110. O. Ovsitser, Y. Uchida, G. Mestl, G. Weinberg, A. Blume, J. Jager, M. Dieterle, H. Hibst, R. Schlogl, *J. Mol. Catal. A.* 185 (2002) 291.
111. B.Y. Jo, E.J. Kim, S.H. Moon, *Appl. Catal. A: Gen.* 358 (2009)180.
112. R.P. Rastogi, A.K. Singh, C.S. Shukla, *J. Solid State Chem.* 42 (1982) 136.
113. B. Zhou, P. Sun, S. Sheng, X. Guo, *J. Chem. Soc. Faraday Trans.* 86 (1990) 3145.
114. L.D. Krenzke, G.W. Keulks, *J. Catal.*64 (1980) 295.
115. G.W. Keulks, J.L. Hall, C. Daniel, K. Suzuki, *J. Catal.* 34 (1974) 79.
116. M.D. Wildberger, J.D. Grunwaldt, M. Maciujewski, T. Mallat, A. Baiker, *Appl. Catal. A* 175 (1998) 11.
117. M. Kakihana, *J. Sol-Gel Sci. Technol.* 6 (1996) 7.
118. E. Godard, E.M. Gaineaux, P. Ruix, B. Delmon, *Catal. Today* 61 (2000) 279.
119. J.A. Schwartz, C. Contescu, A. Contescu, *Chem. Rev.* 95 (1995) 477.
120. M.T. Le, W.J.M. Van Well, I. Van Driessche, S. Hoste, *Appl. Cat. A.* 267 (2005) 227.
121. Y. Moro-Oka, W. Ueda, *Adv. Catal.* 40 (1994) 233.
122. T. Ono, N. Ogata, R.L. Kuczkowski, *J. Catal.* 175 (1998) 185.
123. R. Rangel, P. Bartolo-Perez, E. Martinez, X.A. Trejo-Cruz, G. Diaz, D.H. Galvan, *Cat. Sci. and Tech.* 2 (2012) 847.
124. K. Schuh, W. Kleist, M. Høj, V. Trouillet, A. D. Jensen, J.-D. Grunwaldt, *Chem. Commun.* 50 (2014) 15404

125. K. Schuh, W. Kleist, M. Høj, V. Trouillet, P. Beato, A.D. Jensen, J-D. Grunwaldt, *Catalysts*. 5 (2015) 1554.
126. L. Wang, B. Peng, L. Peng, X. Guo, Z. Xie, W. Ding, *SCIENTIFIC REPORTS*. 3 (2013) 2881.
127. A. F. van den Elzen, G. D. Rieck, *Acta. Cryst. B29* (1973) 2433.
128. F. Theobald, A. Laarif, A.W.Hewat, *Mater. Res. Bull.* 20 (1985) 653.
129. A.F. van den Elzen, G.D. Rieck, *Acta. Cryst. B29* (1973) 2436.
130. R.G. Teller, J.F. Brazdil, R.K. Grasselli, *Acta. Cryst. C40* (1984) 2001.
131. A. Bielanski, J. Haber, *Oxygen in Catalysis*, Marcel Dekker Inc. Newyork (2009)
132. D.B. Dadyburjor, E. Ruckenstein, *J. Catal.* 63 (1990) 383.
133. F.J. Berry, *J. Catal*, 58 (1979)61.
134. J.L. Portefaix, P. Bussiere, M. Forissier, F. Figueras, J.M. Friedt, J.P. Sanchez, F. Theobalt, *J. Chem. Soc. Faraday Trans. 1* (1980) 652.
135. F.J. Berry, *Adv.Catal.* 30 (1981) 97.
136. M. Crozat, J.E. Germain, *Bull. Soc. Chim. Fr.* (1975) 1125.
137. J.C. Volta, B. Benaichouba, I. Mutin, J.C. Vedrine, *Appl. Catal.* 8 (1983) 215.
138. Y. Boudeville, F. Figueras, M. Forissier, J.L. Portefaix, J.C. Vedrine, *J. Catal.* 58 (1979) 52.
139. V. Fattore, Z.A. Fuhrman, G. Manara, B. Notari, *J. Catal.* 37 (1975) 215.
140. G.W. Godin, C.C. Mae Cain, E.A. Porter, in J.W. Hightower (Editor), *Proc. 4th Int. Congr. Catalysis, Moscow, 1968, Vol.1, Elsevier, (1969) pp. 347.*
141. D.L. Trimm, D.D. Gabay, *Trans. Faraday Soc.* 67 (1971) 2782.
142. L.D. Krenzke, *The Kinetics and Mechanism of Propylene oxidation over Bismuth Molybdate*, The University of Wisconsin. (1977).
143. B.J. Evans, *J. Catal.* 41 (1976) 271.

144. R.K. Graselli, D.D. Suresh, *J. Catal* 25 (1972) 273.
145. P. Hayden, G.R. Higgins, Selective oxidation of Hydrocarbons over mixed metal oxide catalysts in C. Kemball (ed.), *Catalysis*, Vol.1 (1976), The chemical society London, pp, 169.
146. I. Matsuura, *J. Catal.* 35 (1974) 452.
147. M. Imachi, R.L. Kuczkowski, J.T. Groves, N.W. Cant, *J.Catal.* 82 (1983) 355.
148. S. Duan, M, Kahn, S. Senkan, *Combinatorial Chemistry & High Throughput Screening* 10 (2007) 111.
149. J. Xie, Q. Zhang, K.T. Chuang, *Appl.Cat A: Gen.* 220 (2001) 215.
150. N. Dimitratos, C.D. Pina, E. Faletta, C.L. Bianchi, V.D. Santo, M. Rossi, *Cat.Tod.* 122 (2007) 307.
151. Y. He, Y. Wu, X. Yi, W. Weng, H. Wan, *React.Kinet.Mech.Cat.* 99 (2010)149.
152. Y.Q. Zhang, Y. Xuan, S.S. Qian, X.L. Li, Y.Q. Jia, *J.Mat.Chem.* 34 (1999) 4475.
153. F. Abrahams, F. Krok, *Solid State Ion.* 157 (2003) 139.
154. A.V. Firsov, A.A. Bush, A.E. Mirkin, Y.N. Venetsev, *Kristallografiya* 30 (1985) 932.
155. G.N. Subbanna, L. Ganapathi, *Bull. Mater. Sci.* 9 (1987) 29.
156. M. Huve, R.N. Vannier, G. Nowogrocki, G. Mairesse, G. Van Tendeloo, *J. Mater. Chem.* 6 (1996) 1339.
157. G. Mairesse, P. Roussel, R.N. Vannier, M. Anne, C. Pirovano, G. Nowogrocki, *Solid State Sci.* 5 (2003)
158. O. Joubert, A. Jouanneaux, M. Ganne, *Mater. Res. Bull.* 29 (1994) 175.
159. G. Mairesse, P. Roussel, R.N. Vannier, M. Anne, C. Pirovano, G. Nowogrocki, *Solid State Sci.* 5 (2003) 861.
160. S.K. Ramasesha, A.K. Singh, K.B.R. Varma, *Mater. Chem. Phys.* 48 (1997) 136.

161. N. Syam Prasad, K.B.R. Varma, *J. Mater. Chem.* 11 (2001) 1912.
162. M. Joseph, H.Y. Lee, H. Tabata, T. Kawai, *J. Appl. Phys.* 88 (2000) 1193.
163. F. Abraham, J.C. Boivin, G. Mairesse, G. Nowogrocki, *Solid State Ion.* 28 (1987) 529.
164. R. Kant, K. Singh, O.P. Pandey, *Ionics.* 15 (2009) 567.
165. A.J. Jacobson, *Chem. Mater.* 22 (2010) 660.
166. F. Abraham, J.C. Boivin, G. Mairesse, G. Nowogrocki, *Solid State Ion.* 40-41(1990) 934.
167. G. Kaur, O.P. Pandey, K. Singh, *Phys. Status Solidi A*, 209 (2012) 1231.
168. W. Yao, J. Ye, *J. Phys. Chem. B* 110 (2006) 11185.
169. V. Thakral, S. Uma, *Mat. Res. Bull.* 45 (2010) 1250.
170. F. Abraham, M. F. Debreuille-Gresse, G. Mairesse, G. Nowogrocki, *Solid State Ion.* 28-30 (1988) 529.
171. N. M. Sammes, G. A. Tompsett, H. Nafe, F. Aldinger, *J. Eur. Ceram. Soc.* 19, 1801 (1999)
172. C. Piravano, M.C. Steil, E. Capoen, G. Nowogrocki, R.N. Vannier, *Solid State Ion.* 176 (2005) 2079.
173. F. Abrahams, F. Krok, M. Malys, W. Wrobel, *Solid State Ion.* 176 (2005) 2053.
174. J. Yan, M. Greenblatt, *Solid State Ionics* 81 (1995) 225.
175. F. Krok, I. Abrahams, W. Wrobel, S.C.M. Chan, M. Malys, W. Bogusz, J.R. Dygas, *Solid State Ionics* 154–155 (2002) 511.
176. G. Pasciak, J. Chmielowiec, P. Bujlo, *Mater. Sci. Poland* 23 (1) (2005) 209.
177. E. Pernot, M. Anne, M. Bacmann, P. Strobel, J. Fouletier, R.N. Vannier, G. Mairesse, F. Abraham, G. Nowogrocki, *Solid State Ionics* 70–71 (1994) 259.
178. P.J. Gellings, H.J.M. Bouwmeester, *Catal. Today* 58 (2000) 1.

179. P.J. Gellings, H.J.M. Bouwmeester, eds. *The CRC Handbook of Solid State Electrochemistry* (CRC Press, Boca Raton, 1997).
180. J.W. Pell, K.M. Delak, H.C. zur Loye, *Chem. Mater* 10 (1998) 1764.
181. A. Cherrak, R. Hubaut, Y. Barbaux and G Mairesse, *Catal. Lett.* 15 (1992) 377.
182. A. Chetouani, B. Taouk, E. Bordes-Richard, E. Abi-Aad and A. Aboukai's, *Appl. Catal. A : General* 252 (2003) 269
183. A. Chetouani, B. Taouk and E. Bordes-Richard, *Catal. Today*. 91–92C (2004) 75.
184. R. Kaur, S. Thakur, K. Singh, *Physica B*. 440 (2014) 78.
185. S. Beg, Niyazi A.S. Al-Areqi, Sadaf Haneef *Solid State Ionics* 179 (2008) 2260.
186. W. Xie, W. Hu, L. Zou, D. Bao, *Ceram. Int.* 41 (2015) S265
187. J.W. Pell, J.Y. Ying, H-C zur Loye, *Materials Letters* 25 (1995) 157.
188. L. W. Vernon, W. Milligan, *Tex. J. Sei.* 3 (1951) 82.
189. R. S. Roth, J. L. Waring, *Am. Mineral.* 48 (1963) 1348.
190. H. Schuer, W. Klemm, *Z. Anorg. Mg. Chem.* 395 (1973) 287.
191. T. Birchall, A.E.Sleight, *Inorg. Chem.* 15 (1976) 868.
192. S. Hansen, K. Stahl, R. Nilsson, A.J. Andersson, *Solid State Chem.* 102 (1993) 340.
193. M.O. Guerrero-Perez, J. Janas, T. Machej, A. Haber, A. Lewandowska, J. García-Fierro, M.A. Banares, *Appl. Catal. B: Environ.* 71 (2007) 85.
194. B. Kim, D. Park, I. Kim, H. Woo, *Catal. Today*. 87 (2003) 11.
195. K. Li, K. Wu, *Ind. Eng.Chem. Res.* 40 (2001) 1052.
196. H. Zhang, J. Zhang, K. Sun, Z. Feng, P. Ying, C. Li, *Catal. Lett.* 106 (2006) 89.
197. A. Guttman, R.K. Grasselli, J.F. Brazdil, *US Pat.* 4, 746, 641, 4,788, 317, 1988.
198. M.O. Guerrero-Pérez, J.L.G Fierro, M.A. Banares, *Top. Catal.* 41 (2006) 43.
199. S. Hamid, G. Centi, P. Pal, E. Derouane, *Top. Catal.* 15 (2001) 161.

200. R.K. Grasselli, J.D. Burrington, D.J. Buttrey, P. De Santo, C.G. Langmuir, *Top. Catal.* 23 (2003) 5.
201. G. Centi, P. Mazzoli, S. Perathoner, *Appl. Catal. A* 165 (1997) 273.
202. M.O. Guerrero-Pérez, J.L.G. Fierro, M.A. Bañares, *Catal. Today*. 118 (2006) 366.
203. R.G. Teller, M.R. Antonio, J.F. Brazdil, R.K. Grasselli, *J. Solid State Chem.* 67 (1986) 249.
204. Y. Haraguchi, T. Wada, Y. Ominami, N. Matsudaira, H. Ariga, S. Takakusagi, K. Asakura, *Kiyotaka Hyomen Kagaku* 33 (2012) 426.
205. Y. Ohminami, S. Suzuki, N. Matsudaira, T. Nomura, W.J. Chun, K. Ijima, M. Nakamura, K. Mukasa, N. Koichi, M. Nagase, K. Asakura, *Bulletin of the Chemical Society of Japan*. 78 (2005) 435.
206. T. Shishido, T. Konishi, I. Matsuura, Y. Wang, K. Takaki, K. Takehira, *Catal. Today*. 71 (2001) 77.
207. H. Roussel, B. Mehlomakulu, F. Belhadj, E. van Steen, J.M.M. Millet, *J. Catal.* 205 (2002) 97.
208. G. Centi, P. Mazzoli, *Catal. Today*. 28 (1996) 351.
209. S. Larrondo, B. Irigoyen, G. Baronetti, N. Amadeo, *Appl. Catal. A: Gen.* 250 (2003) 279.
210. E. Mamedov, *Appl. Catal. A: Gen.* 474 (2014) 34.
211. S. Thangaraj, B. Arumugam Chandra, V. Sivan, *J. Nanosci. Nanotechnol.* 15 (2015) 5760.
212. L. Xiang and Q. Long, *Rev. Nanosci. Nanotechnol.* 3 (2014) 161.
213. X. Min, M.H. Fang, Z.H. Huang, Y.G. Liu, C. Tang, X.W. Wu, *Mater. Lett.* 125 (2014) 140.

214. C. C. Lin, Z. R. Xiao, G. Y. Guo, T. S. Chan, R. S. Liu, *J. Am. Chem. Soc.* 132 (2010) 3020.
215. E.F. Schubert, J.K. Kim, *Science*. 308 (2005) 1274.
216. Z.Y. Zhang, J.G. Wang, Y.L. Yin, J.J. Zhou, S.P. Zhou, Y.X. Pan, *Opt. Mater.* 35 (2013) 1273.
217. S.J. Nakamura, M. Senoh, T. Mukai, *Appl. Phys. Lett.* 62 (1993) 2390.
218. A. A. Fotiev, B. V. Shul'gin, A. S. Moskvina, F. F. Gavrilov, *Vanadievye Kristallofosfory (Crystalline Vanadium Phosphors) Nauka, Moscow, Vol. 3 (1976) pp. 206.*
219. T. Nakajima, M. Isobe, T. Tsuchiya, and Y. Ueda, *Nat. Mater.* 7, 735 (2008)
220. A. Grzechnik, P.F. McMillan, *Solid State Commun.*102 (1997) 569.
221. A. Grzechnik, P.F. McMillan, *J. Solid State Chem.* 132 (1997) 156.
222. B. Buijsse, J. Schmidt, I.Y. Chan, D. J. Singel,1995 *Phys. Rev.*B51 62,15
223. L.D. Merkle, A. Pinto, H. Verdun, B. McIntosh, *Appl.Phys. Lett.* 61 (1992) 2386.
224. P. Ghosh, J. Oliva, E.D.L. Rosa, K.K. Haldar, D. Solis, A. Patra, *J. Phys. Chem. C.* 112 (2008) 9650.
225. L.H. Brixner, P.A. Flournoy, *J. Electrochem. Soc.* 112(3) (1965) 303.
226. X.C. Zhou, L.P. Zhong, Q.P. Liu, R.Y. Kuang, H.M. Chen, *Inorg. Mater.* 45 (2009) 1295.
227. R. Kasuya, T. Isobe, K.H. Katano *J. Phys. Chem. B* 109, 22126
228. X. Mi, H. Shi, Z. Wang, L. Xie, H. Zhou, J. Su, J. Lin 2016 *J. Mater. Sci.* 51 (2016) 3545
229. C.H. Lu, R. Jagannathan, *Appl. Phys. Lett.* 80 (2002) 3608.
230. H. Ning, H. Yan, M.J. Reece, *Ferroelectrics.* 487 (2015) 94
231. R. Gopal, C. Calvo, *Z. Kristallogr.* 137 (1973) 67

232. A.M. Glass, S.C. Abrahams, A.A. Ballmann, G. Laiacono, *Ferroelectrics*. 17 (1978) 579.
233. A. Grzechnik, *Solid State Sci.* 4 (2002) 523.
234. G. Tammann, *Z. Anorg. U. Allgem. Chem.* 149 (1925) 68.
235. C-Z. Li, W-H. Yang, Y-C. Chang, *Ferroelectrics*. 142 (1993) 131.
236. X. Mi, H. Shi, Z. Wang, L. Xie, H. Zhou, J. Su, J. Lin, *J. Mater. Sci.* 51 (2016) 3545.
237. H-Y. Lin, Y-C. Fang, X-R. Huang, S-Y. Chu. *J. Am. Ceram. Soc.* 93 1 (2010) 138.
238. H-Y. Lin, S-Y. Chu, *J. Am. Ceram. Soc.* 95 11 (2012) 3538.
239. X. Zhou, X. Wang, R. Kuang, J. Guo, H. Chen , *Inorganic Materials*. 46 11 (2010) 1244.
240. L.H.C. Andrade , D. Reyes Ardila , J.P. Andreetta , M. Siu Li, *Optical Materials*. 22 (2003) 369
241. J. Huang, Q. Li, D. Chen, *Materials Science and Engineering B*. 172 (2010) 108.
242. H. Zhang, M. Lu, Z. Xiu, S. Wang, G. Zhou, Y. Zhou, S. Wang, Z. Qiu, A. Zhang, *Mater. Res. Bull.* 42 (2007) 1145.
243. H-Y. Lin, W-F. Chang, S-Y. Chu, *J. Lumin.* 133 (2013) 194.
244. K. Qiu, J. Li, J. Li, X. Lu, Y. Gong, J. Li, *J. Mater. Sci.* 45 (2010) 5456.
245. B. Yan, X.Q. Su, *J. Alloys Compd.* 431 (2007) 342
246. B. Yan, X.Q. Su, *Optical Mater.* 29 (2007) 1866.
247. J.H. Wu, B. Yan, *J. Alloys Compd.* 455 (2008) 485.
248. A.R. Forbes, C.D. McMillen, H.G. Giesber, J.W. Kolis, *J. Crystal Growth*. 310 (2008) 4472

249. H.P. Zhang, M.K. Lu, Z.S. Yang, Z.L. Xiu, G.J. Zhou, S.F. Wang, Y.Y. Zhou, S.M. Wang, *J. Alloys Compd.* 426 (2006) 384.
250. K. Riwozki, M. Haase, *J. Phys. Chem. B* 102 (1998) 10129
251. G. Blasse, *Prog. Solid State Chem.* 18 (1988) 79.
252. J. Sut, L. Bora, A. Pandey, *International Journal of Innovative Research and Development*, 1 (2012) 181.
253. A. Martí'nez-de la Cruz, S. O. Alfaro, *Solid State Sci.* 11 (2009) 829.
254. M. Alga, A. Ammar, R. Essalim, B. Tanouti, F. Mauvy, R. Decourt, *Solid State Sci.* 7 (2005) 1173.
255. A.K. Bhattacharya, K.K. Mallick, *Solid State Comm.* 91 (1994) 357
256. A. Ghule, S-H Tzing, J-Y Chang, K. Ghule, H. Chang, Y. C. Ling, *Eur. J. Inorg. Chem.* (2004) 1753.
257. S.R.G. Carrazán, C. Martin, V. Rives, R. Vidal, *Spectrochimica Acta Part A.* 52 (1996) 1107.
258. .P. Tolstoy, E.V. Tolstobrov, *Solid State Ionics.* 151 (2002) 165.
259. K. Nakamoto, *Infrared and Raman Spectra of Inorganic and Coordination Compounds*, John Wiley & Sons, New York (1997).
260. R. Kaur, S. Thakur, K. Singh, *Physica B.* 440 (2014) 78.
261. P. Parhi, V. Manivannan, S. Kohli, P. McCurdy, *Bull. Mater. Sci.* 31 (2008) 885.
262. A. Grzechnik, *Chem. Mater.* 10 (1998) 1034.
263. S.A. Kovyazina, L.A. Perelyaeva, O.N. Leonidova, I.A. Leonidov, A.L. Ivanowskii, *Crytallography Rep.* 49 (2004) 211.
264. K. Qiu, J. Li, J. Li, X. Lu, Y. Gong, J. Li, *J. Mater. Sci.* 45 (2010) 5456.
265. M.R. Dolgos, A.M. Paraskos, M.W. Stoltzfus, S. C. Yarnell, P. M. Woodward, *J. Solid State Chem.* 182 (2009) 1964.

266. T. Wang, Y. Hu, L. Chen, X. Wang, G. Ju, *Appl. Phys.A* . 120 (2015) 301.
267. J. Huang, Q. Li, D. Chen, *Mater. Sci. Eng. B*. 172 (2010) 108.
268. R.M. Jafer, E. Coetsee, A. Yousif, O.M. Ntwaeborwa, H.C. Swart, *Appl. Surf. Sci.* 332 (2015) 198.
269. V.J. Babu, R.S.R. Bhavatharini, S. Ramakrishna, *RSC Advances*. 4 (2014) 29957.
270. A. Chaudhari, T. Ghoshal, M. T. Shaw, J. O'Connell, R. A. Kelly, C. Glynn, C O'Dwyer, J.D. Holmes, M. A. Morris, *Adv. Mater. Interfaces*. 3 (2016) 1500596.
271. M. Zhou, L. Cai, M. Bajdich, M. Garcia-Melchor, H. Li, J. He, J. Wilcox, W. Wu, A. Vojvodic, X. Zheng, *ACS Catal.* 5 (2015) 4485.
272. S.S. Parab, A.V. Salker, *Buletin of Chemical Reaction Engineering and Catalysis*. 12 (2017) 197.
273. Y. Y. Luo, L. Q. Zhu, Y. X. Zhang, S. S. Pan, S. C. Xu, M. Liu, G. H. Li, *J. Appl. Phys.* 113 (2013) 183520.
274. Y. Zhang, J. Tian, K. Jiang, J. Huang, H. Wang, Y. Song, *RSC. Adv.* 7 (2017) 41540.
275. H.Van Doveren, J.A.T Verhoeven, *J. Electron Spectrosc. Relat. Phenom*, 21 (1980) 265.
276. J.G. Choi, M.K. Ryu, C.H. Cho, D.H. Cho, N.E. Sung, J.P Kim, M.S. Jang, *Ferroelectrics*. 332 (2006) 29.
277. Z. Li, Q. Zhu, S. Huang, S. Jiang, S. Lu, W. Chen, G.S. Zakharova, *RSC Adv.* 4 (2014) 46624.
278. H-M Yang, J-X Shi, H-B Liang, M-L Gong, *Mater. Res. Bull.* 41 (2006) 867.
279. S.S. Parab, A.V. Salker, *Mater. Res. Express*. 5 (2018) 0163302.

APPENDIX

PUBLICATIONS

1. **Shambhu S. Parab**, S.J. Naik, A.V. Salker

‘Partial oxidation of propene over as prepared and acid enriched $\text{Bi}_2\text{Mo}_{1-x}\text{W}_x\text{O}_6$ system’

Bulletin of Chemical Reaction Engineering and Catalysis, 12 (2017) 197-205.

2. **Shambhu S. Parab** and A.V. Salker

‘Structural and optical properties of Tb and Na–Tb co-doped $\text{Ca}_3\text{V}_2\text{O}_8$ phosphors prepared by sol–gel process’

Materials Research Express, 5 (2018) 016302.

3. **Shambhu S. Parab** and A.V. Salker

‘Propene partial oxidation over $\text{V}_{1-x}\text{Cu}_x\text{SbO}_4$ and Cu-K-V-Sb-O systems’

Communicated (2018)

4. **Shambhu S. Parab** and A.V. Salker

‘Preparation, characterization and luminescence studies of Eu-Tb co-doped $\text{Ca}_3\text{V}_2\text{O}_8$ phosphors.

Communicated (2018)

PAPERS PRESENTED AT SEMINARS/WORKSHOP

1. Shambhu S. Parab and A.V. Salker “Partial oxidation of propene over Cu/Bi₂Mo₃O₁₂ catalysts” at Catsymp 21, 11-13 February 2013 held at IICT Hyderabad.

Awarded ‘Hindustan Platinum award for Best Poster’

2. Shambhu S. Parab and A.V. Salker “Preparation, characterization and catalytic studies over selected alkaline earth vanadates” at Royal Society of Chemistry (UK) West India Chapter Symposium. 13th November 2016, held at BITS Pilani, Goa Campus.